A-priori tabulation of sub model coefficients for efficient numerical combustion system design

A thesis for the attainment of an

Engineering Doctorate

University of Brighton

2019

By

Daniel M. Nsikane

Abstract

The wide range of operating conditions and the multiscale nature of the physical processes makes numerical replication of in-cylinder fuel injection, mixing and combustion events a difficult task. In commercial engine development, these difficulties are compounded with limited computational resources and the requirement for fast development cycles. Combined, they are the main reason that for commercial purposes, simplified computational models with user-defined modelling coefficients are preferred over physically accurate methods without tuning dependency. Producing reliable in-cylinder simulations for quick turnaround engine development is a challenging task for modern CFD tools, mostly because of the tuning effort required for the sub-grid scale (SGS). Common practice is to prepare simulations for a baseline key point, tune the simulation to match available experimental data, and then use the tuned setup to predict other operating conditions or even engine configurations. The underlying assumption made when employing this approach is that all used sub models and their respective modelling coefficients are physically accurate and can therefore be representative for changing boundary conditions. This is however rarely the case.

This thesis covers four objectives. First, a combination of industry standard and relatively simple simulation sub models is selected, and their limits identified. Secondly, it challenges the common practice of matching a baseline experiment and swinging the boundary conditions with a fixed simulation setup. Next, a novel modelling coefficient table is developed that can match a wide range of idealised experiments from the Engine Combustion Network. Finally, the performance of simulations, whose settings are based solely on the novel modelling coefficient table, are tested selected on experimental data from two small-bore LDD DI Diesel engines at two load conditions.

The approach in this thesis shows that it has the potential to remove the necessity of lengthy and tedious tuning iterations by standardising and accelerating the simulation preparation. The modelling coefficient table is derived using a combination of Design-of-Experiment and stochastic process modelling. This statistical approach applied to a large range of operating conditions and a variety of computational models visualises the physical multivariable interactions between modelling coefficients and governing boundary conditions and lays the groundwork for novel auto-tuned and predictive in-cylinder simulations.

Table of contents

Declaration

I declare that the research contained in this thesis, unless otherwise formally indicated within the text, is the original work of the author. The thesis has not been previously submitted to this or any other university for a degree and does not incorporate any material already submitted for a degree.

Signed: Dated:

List of figures

List of tables

List of acronyms

Abbreviation	Definition
ASOI	After Start of Injection
BMEP	Break Mean Effective Pressure
CFD	Computational Fluid Dynamics
CMC	Conditional Moment Closure
CMT	Universitario De Motores Térmicos
CV	Constant Volume
DDM	Discrete droplet method
DNS	Direct Numerical Simulation
DoE	Design-of-Experiment
ECN	Engine Combustion Network
EGR	Exhaust Gas Recirculation
EVO	Exhaust Valve Opening
FIE	Fuel Injection Equipment
GDI	Gasoline Direct Injection
ID	Ignition delay
IMEPg	Indicated Mean Effective Pressure
IVC	Intake Valve Closure
IFPEN	Institut Français du Pétrole Energies Nouvelles
KH	Kelvin-Helmholtz
KP	Key point
LDD DI	Light Duty Diesel Direct injected
LES	Large Eddy Simulation
LoL	Lift-off-Length
LPT	Lagrangian Particle Tracking
NVH	Noise-Vibration-Harshness
PDF	Probability Distribution Function
PRF	Primary Reference Fuel
RANS	Reynolds-Averaged Navier-Stokes
RoHR	Rate of Heat Release
RoI	Rate of injection
RT	Rayleigh-Taylor
RTZF	Ricardo Two-Zone Flamelet model
SGS	Sub-grid scale
SMD	Sauter Mean Diameter
SNL	Sandia National Laboratories
SoC	Start of combustion
SoCF	Start of Cool Flames
SoI	Start of injection
SPM	Stochastic Process Model
SSI	Second Stage Ignition
TCI	Turbulence Chemistry Interactions
TPDF	Transport Probability Distribution Function

Nomenclature

Symbol	Definition
k	Turbulent kinetic energy
ε	Dissipation rate
U_i	Velocity component
x_i	Location component
μ_t	Turbulent viscosity
G	Generation rate of turb. energy
σ_k	Standard k-ε modelling coefficients
σ_ϵ	
C_1, C_2, C_3	
m_d	Droplet mass
V	Droplet velocity
C_d	Drag coefficient
A_f	Projected area
A_{drag}	Drag scaling coefficient
ρ_g	Gas density
Re_d	Droplet Reynolds number
r	Parent droplet radius
r_c	Child droplet radius
Λ_{KH}	Maximum wave growth rate
Ω_{KH}	Grow rate wavelength
τ_{KH}	Characteristic break-up time
Λ_{RT}	Corresponding wavelength
K_{RT}	Wave number
Ω_{RT}	Frequency of the fastest growing wave
τ_{RT}	Characteristic break-up time
D_d	Stable droplet diameter
B_1	KH-RT Spray model coefficients
B_0	
C_{RT}	
C_3	
L_b	Levich break-up length
A_{bu}	Levich model coefficients
B_{bu}	
D_n	Nozzle diameter
ρ_l	Liquid density
Sc_t	Turbulent Schmidt number
K	Eddy diffusivity
ω_{mix}	Turbulent mixing rate
Y_i^{seg}	Mixture fraction in the segregated zone
Y_{ig}	Mixture fraction in ignition zone
C_{mix}	Mixing coefficient
P_{ig}	Probability of reactant auto-ignition
i_{ig}	Ignition delay time
c_{ig}	Auto-ignition coefficient
A	Empirical ignition delay coefficients
n	
T_a	Activation temperature
ω_{ig}	Reaction rate
T_f	Flame temperature
B	Empirical pre exponential coefficient
τ_c	Chemical reaction rate
$\tilde{C}$	Combustion progress variable
Y_x	Mass fractions (A=Air, F=Fuel, B=Burnt, R=Residual)
ω_f	Turb. controlled reaction rate
r_{vol}	Ratio of unburned fully mixed reactants to total cell volume
τ_t	Turbulent mixing time scale
S_t	Turbulent flame speed
S_l	Laminar flame speed
l_c	Characteristic length scale
A_0	Burn velocity multiplier
ρ_u	Unburnt-zone density
α_{turb}	Turb. flame speed multiplier
q	Empirical coefficient
S_l^0	Laminar flame speed at reference conditions
α	Original Metghalchi and Keck model coefficients
β	
$\dot{q}^n$	Total heat release
q_{cell}^n	Heat release in every cell
q_{io}^n	Heat release to/from boundaries
q_{spray}^n	Heat contribution from spray
$h_{\dots}^n$	Formation enthalpies

Acknowledgements

I would like to express my sincere gratitude to Mr. Kenan Mustafa and Dr Konstantina Vogiatzaki for their exceptional motivational and technical support throughout my research project. Their advice and mentoring on topics within and beyond the EngD was immensely valuable and will guide me through my entire private and professional life.

Next, I would like to thank Prof Dr Robert Morgan, Prof Dr Morgan Heikal, Andy Ward and Nick Winder for always offering advice, insightful comments and encouragement, but also for asking the hard questions to keep the project progress and content on track.

I also would like to express much appreciation to Prof Dr David Mason who, besides helpful advice on research topics, equipped me with a financial buffer by offering various staff positions throughout the last four years.

I thank all my colleagues at Ricardo Ltd, fellow students and researchers from the Advanced Engineering Centre at the University of Brighton for creating such a fun and productive working environment and for helping when questions arose. I also thank all the administrative staff at the school office and doctoral collage for being there to answer any queries.

Lastly, I would like to thank my family, my partner and my close friends for their support and encouragement throughout my EngD.

1 Introduction

1.1 Motivation

In recent years, the development of Internal Combustion Engines (ICE's) has become increasingly reliant on virtual engineering tools. The need to comply with tightening emission regulations and shortening development cycles are putting pressure on engine manufacturers, raising the importance of early stage numerical simulations for in-cylinder processes. The process of Diesel fuel direct injection into a combustion chamber is typically simulated with one or multidimensional Computational Fluid Dynamics (CFD) tools. It is a challenging and computationally demanding task to simulate the full combusting spray process, in particular for realistic conditions of injection pressures reaching beyond 250MPa.

Computational methods that calculate processes like turbulent motion and combustion to a physically accurate level are rarely usable in industry. With current numerical capabilities, an "all scale analysis" using Direct Numerical Simulation (DNS) is impossible due to the multi-scale, multi-phase nature of liquid-gas interactions and the complexity of finite-rate evaporation, mixing and multi-step reactions. For many interest groups quick-turnaround simulations of global parameters like pressure rise and the associated heat release characteristic and, to a smaller extent, spray characteristic for piston bowl design are of paramount importance. Capturing characteristic trends of changing operating points potentially allows faster engine mapping. For this, engineers may want to run dozens of simulations at varying key points and hardware configurations. A single, full-scale simulation of a combusting spray with a DNS approach can take up to weeks on a supercomputer. For this reason, modelling approaches that simplify parts of the mathematical/physical background (such as the ones used within Reynolds-Averaged Navier-Stokes (RANS) context and to some extent Large Eddy Simulations (LES) for turbulent motion and tabulated or reduced chemical kinetic models for combustion) are used to reduce computational runtimes. The simplifications of these models are the source of the major tuning dependency.

1.2 The problem

A typical approach to simulating engine performance parameters with CFD is shown in Figure 1. First, a key point with known characteristics is simulated. To match the comparison metrics like cylinder pressure, heat release or emission data, the simulation setup is adjusted iteratively. Once the simulations match the experiments, the same simulation setup is used for a range of key points of interest.

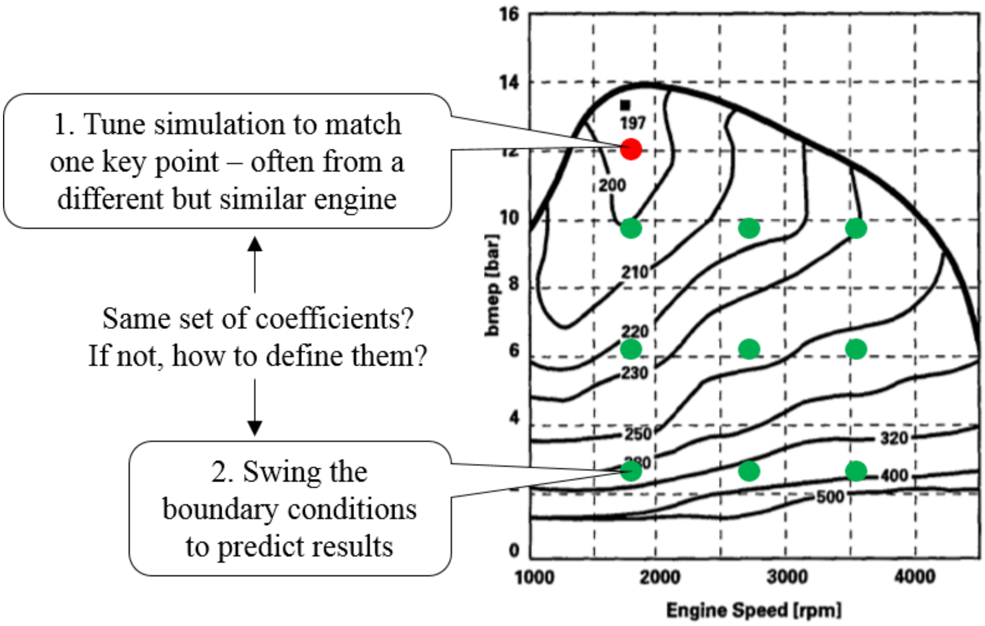

Figure **1**: *The dilemma engineers face when selecting the coefficients to simulate a range of operating points. Image of typical engine map reproduced from Georgi* et al *in [1]*

Two problems arise immediately with this approach:

1. In early engine development, experimental data are not available and are therefore taken from similar operating conditions and hardware configurations of previous engines.
2. There is no standard or consensus on which sub models should be used and how their modelling coefficients should be set.

When the sub models' settings in low-resolution simulation approaches like RANS and LES are left unchanged throughout swinging operating conditions, an assumption is made that the models' mathematical fundamentals are sophisticated enough to replicate the physical changes in the environment. This is not always the case because the empirical sub models are often derived from observations under operating conditions that may not represent real engine conditions. Accepting the limitations of simplified sub models and improving modelling coefficient selection capabilities, can greatly improve simulation accuracy without negatively affecting runtimes. Even more advantageous would be if it were possible to define the value of key modelling coefficients prior to any simulation.

1.3 The goal

The focus of this thesis is to propose a generalised modelling coefficient table for inert and reactive spray conditions. This table will be used for a priori definition of modelling coefficients for a range of boundary conditions in a physically consistent manner. The importance of the thesis is that from a research point of view, this is the first study that attempts to provide a link between modelling coefficients and the underlying physical processes and from practical point of view, it suggests a method capable of accelerating simulations without compromising the physical representation of the processes.

The successful delivery of this goal has a strong potential to improve the virtual engineering process of light duty diesel (LDD) engine developers. In the end, a modelling coefficient definition process based on tabulation paves the way of use of automation or machine learning techniques that are currently of interest within virtual design product manufacturing.

The project structure is shown in Figure 2. The steps indicated by white squares are the intermediate objectives that are necessary to achieve the above stated goal (marked as green endpoint). To progress from one objective to another stand research questions (orange blocks) that must be answered with definitive conclusions to justify the next step or conclude that the stated goals are not achievable in this format (red terminator blocks). Also shown are some iteration loops (beige blocks) which are crucial to the quality but do not immediately threaten the overall feasibility of the project. In the following two sections, the objectives and research questions are discussed in more detail.

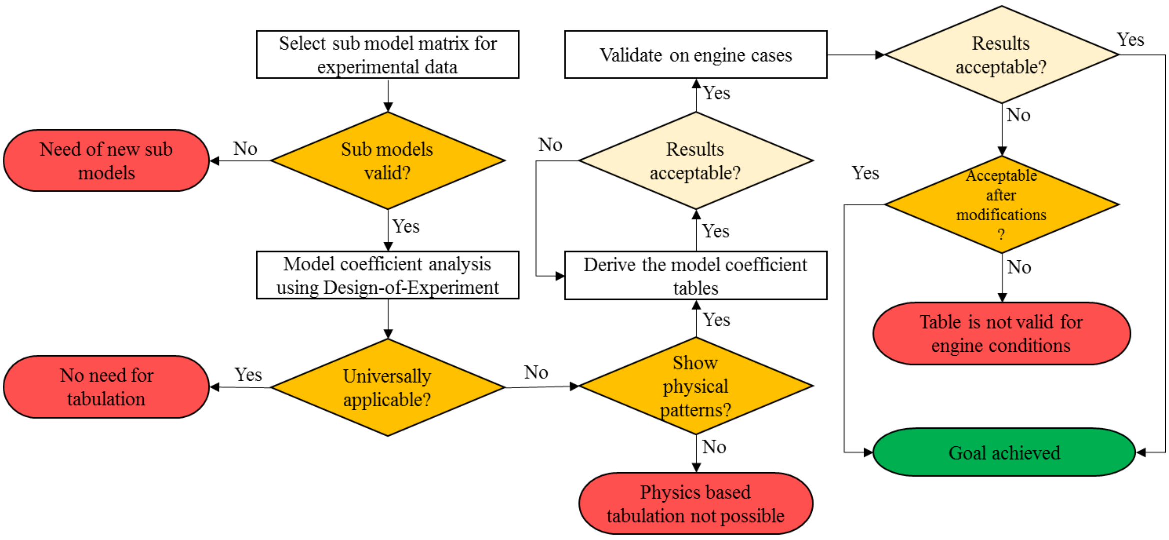

Figure 2: Project decision-making flowchart. White blocks: intermediate objectives; Orange blocks: research questions; Red blocks: terminate research project; Green block: endpoint of research

1.3.1 The objective

To reach the stated goal of producing a modelling coefficient table with respect to governing boundary conditions, the four following objectives must be completed.

1. Select a sub model matrix that is to a large extent industry standard
2. Conduct an extensive investigation into the performance of the modelling coefficients under different operating conditions using a Design-of-Experiment (DoE) approach.
3. Derive a boundary condition dependent modelling coefficient table based on a limited number of operating points that can be used to define the simulation setup of other operating points.
4. The modelling coefficient table that is derived under quiescent conditions must be validated for real engine cases that are within and beyond the range of confidence.

The first objective relates to the practical nature of this project. The simulation setup used here is intended to be applicable for interest groups who typically use standard commercially available simulation tools. Therefore, the selection of the software and the applied sub models will have to fulfil this criterion. The next objective is to perform an in-depth study into the physical-mathematical background of the modelling coefficients to identify any potential links between coefficient sensitivities and changing boundary conditions in a constant volume combustion chamber. This is done by producing Stochastic Process Models (SPMs) using a DoE approach to visualise the sensitivity of simulated metrics to modelling coefficients. This will include hundreds of simulations and various studies into the behaviour of the modelling coefficients. The third objective addresses how these links can be used to predefine the simulation setup for a range of operating conditions. For the modelling coefficient table to be used in a commercial engine development environment it must be valid for real engine conditions. This is the mission of the fourth objective. These objectives contain research questions that will be introduced in the following section

1.3.2 The research questions

The following research questions must be answered to justify the continuation of the project in the form outlined in Figure 2. All four research questions if answered with “no” are set to terminate this path of research.

1.3.2.1 Validity of classical numerical spray models for modern LDD engine conditions

In this thesis, one important aspect is the validity of classical numerical spray models in constant volume combustion chamber experiments that are designed to resemble LDD engine conditions. In recent years, a discussion in the scientific community has emerged as to whether the thermodynamic conditions in a specific set of experiments, which will be introduced in detail, are in the trans-critical or even supercritical mixing regime of the fuel. The thermodynamic conditions of the chamber gas prior to combustion are beyond the critical point of the fuel (chamber gas condition: ~1200 K, ~22,8 kg/m³ and ~8 bar, critical fuel conditions: n-dodecane, Tc=658.3K, Pc=18.2 bar). The first question is whether the continuous injection of cool spray leads to a local cooling of the gas phase around the liquid droplets and subsequent reduction of both local ambient temperature and pressure. The next question is whether this cooling effect is potent enough that only the initial droplets would fall into the super/trans critical regime while the following droplets would be trans/sub critical.

Question 1

Are the most commonly used sub models, which were derived for classical droplet evaporation and break-up processes, valid for simulating the conditions related to real Diesel injection (sometimes approaching trans-critical conditions)?

1.3.2.2 Performance of a single set simulation setup for a range of operating conditions

In the introduction, it is asserted that a single simulation setup with constant modelling coefficients is unable to produce good results for swinging boundary conditions. An important research question is therefore whether this argument is valid. An analysis into whether sub models and their modelling coefficients are sophisticated enough to account for physical changes in the injection process is necessary. This is formulated as:

Question 2

Is there a single coefficient matrix for the various sub-models used in spray injection (namely turbulence, atomisation, evaporation, mixing and combustion) that can provide good match with experimental data at different operating conditions?

1.3.2.3 Identify the link between the spray physics and modelling coefficients

If Question 2 is negated, the next step is to focus on the concept of intelligent coefficient selection strategies of physically reasonable modelling coefficients to trigger similar trends between simulations and experiments if the sub models cannot adequately replicate the real process. Question 3 seeks to identify pre-defined values of key modelling coefficients depending on the boundary conditions and some “key benchmark points”.

Question 3

If a coefficient matrix to match multiple operating points does not exist, are there any trends in the change of the coefficient values linked to physical processes and boundary conditions that can guide the a priori selection of the coefficient values?

If such a pre-definition of modelling coefficients is derivable, then lengthy tuning iterations will no longer be necessary. This opens the possibility of intelligent or even automated tuning.

1.3.2.4 Transferability of modelling coefficient table to real engine conditions

The modelling coefficient table is derived from set of experiments conducted under simplified conditions to focus the study on the spray dynamics. To achieve the fourth objective of this thesis, the question of validity of the modelling coefficient table for real engine conditions must be addressed.

Question 4

Are the model coefficient settings derived from the injection into quiescent conditions representative for real engine conditions?

Conducting experiments on quiescent combustion rigs is significantly easier and cheaper. Should it be possible to calibrate and tabulate the modelling coefficients to these conditions, then there would be merit for an extensive experimental parametric exploration study that can feed back into the development of the tabulation for a larger range of conditions.

1.4 The contribution

Two different contributions are set to come out of this work. One is the scientific contribution, which discusses the mathematical expression of the modelling coefficients in relation to changing operating points. The second is a practical tool to automate the simulation preparation, post processing and result visualisation. The scientific contribution will be at the core of this work while the technical contribution in form of scripts, tools and methods will largely remain confidential for commercial use.

The scientific contribution is that for the first time it is shown that a tabulated form of modelling coefficients of relatively simple sub models can be used to match multiple important comparison metrics without tuning iterations. The most important factor when deriving the table is that the values in the coefficient table, whether they remain constant or change, behave in way that is represented in their mathematical expression. That such a link exists or that simulations can be prepared in such a way has not been shown before. Another important contribution is the applied methodology to arrive at the model coefficient table. This work is conducted with a range of specific tools with in-built sub models. The methodology, however, can be transferred to other simulation software (like Converge, Star CD or OpenFOAM), other simulation approaches (like LES) or, with some creativity, even to other phenomenological areas outside in-cylinder simulations (like friction models, battery models etc.).

1.4.1 The potential application

The achievement of the stated goal could lead to a significant acceleration of virtual engine mapping. The boundary conditions at SoI can be approximated using 0D or 1D modelling approaches. With these calculated boundary conditions, the associated tabulated modelling coefficients can be fed straight into the CFD setup. The result is the simulation of the spray and jet penetration lengths (relatively straightforward), flame lift-off lengths, cylinder pressure and heat release curves (manageable), and finally, emission characteristics (challenging) without tuning iterations. These parameters are important for the following reasons:

1. With knowledge of spray and jet penetrations and spatial flame lift-off, geometrical specifications for the piston bowl can be designed to avoid undesirable wall impingement.
2. Cylinder pressure and heat release characteristics are important markers for combustion performance and NVH (Noise-Vibration-Harshness) characteristics.

3. The prediction of emission production under a range of operating points to estimate legislative conformance.

Current simulation methods cannot yet replace test bed validations but having approximated the above combustion characteristics certainly narrows the scope of necessary testing. This can be by excluding potential geometries or by identifying desirable operating conditions and can, with increasing reliability through method development, deliver measures to improve the product in the digital development phase. These measures open new avenues for reduction of cost reduction and acceleration of the development phase.

In future, instead of spending time to iteratively set up one key point, the table can be used to set up a whole range of conditions spanning the engine speed/load map in one go. Automated modelling coefficient selection coupled with automated simulation setup scripts (as developed for this work) can produce dozens of setups within seconds. Automated execution and post processing scripts further accelerate the simulation process and visualisation of the results while eliminating human error.

A more distant vision of this approach would be the implementation of automated modelling coefficient adjustment. This work will highlight boundary condition sensitive modelling coefficients. In real engines, where the thermodynamic conditions vary strongly throughout a single injection phase, the coefficients between the start and end of injection should theoretically be adapted. This was not within the scope of this thesis, however, shows an exciting potential of a further development of the methodology proposed here.

1.4.2 The scope and limitations

1.4.2.1 The trade-off between speed and accuracy

The approach is to be used for fast simulation results at multiple operating conditions. The selection of the sub models is biased towards speed over mathematical/physical sophistication. Part of the physical accuracy is recoverable with smart modelling coefficient selection. The limitation here is that the overall simplicity of the selected sub models may not always offer a clear physical justification.

1.4.2.2 In-scope combusting spray characteristics

A consequence of using a combination of simplified and statistical models is the reduced detail of the ambient air motion and the spray, evaporation and combustion characteristics. This means that microscopic information of the spatial and temporal mixture, combustion and emission production may not be accurate. For metrics like the spray and jet penetration, heat release and chamber pressure, this limitation is manageable. While the intermediate break-up and evaporation process may not be replicated down the scale of individual droplets or spatial equivalence ratio, the overall penetration lengths can be simulated within the stated experimental uncertainty, which is sufficient for the purpose of this work. The same applies for the heat release and chamber pressure, where it is not the main concern where exactly the combustion occurs and propagates, if the rate of heat release, and hence the cylinder pressure profile, is approximated. The aspired accuracy of the simulations is the replication of the cylinder pressure trace within the experimental uncertainty of the transducer ($\pm 1\%$). Such a clear error band is difficult to define for the heat release rate, as the definitions between the simulation and the experiments differ. Hence, a qualitative comparison between the characteristics of the curves is more appropriate.

1.4.2.3 Out-of-scope combusting spray characteristics

The chemical mechanism used in the combustion model is suspected to pose strong limitations to the prosperity of simulating emission characteristics. The simplicity of the auto-ignition and combustion model by no means can accurately predict processes in which chemical mechanisms are more important than mixing dynamics. Hence, at low temperatures strong tuning is required to keep the simulation results on track. Models that are more elaborate are available, but it is also part of this work to test the limits of these simple models.

Additionally, the cascading inaccuracies of air motion and spray break-up and evaporation models lead to a difficulty in simulating emission results even in conventional load conditions. Out of all emissions, NOx and soot values are currently the most pressing. While global NOx emission simulations, with its limited reliance on the quality of local temperature and species concentrations, are a solvable problem, soot formation and oxidation, with its complex mechanisms and strong reliance on local conditions, remains an onerous task. In the final validation of this work, preliminary simulation results for NOx emissions using a default NOx model were achieved but not added to this thesis as the analysis was still in its infancy. A continuation of this analysis in future work is recommended as it is certain to open numerous new questions and may even inspire a separate doctoral thesis.

1.5 The structure

The thesis is structured as follows: The methodology used to achieve the objectives of the thesis is shown in chapter 2. It details the steps taken to achieve the objectives laid out in the introduction. It also describes the DoE methodology, tabulation and validation.

In chapter 3, the physical processes based on relevant literature that govern the high-pressure fuel injection are thoroughly discussed. The focus hereby lies on publications discussing the influence of thermodynamic boundary conditions and injection parameters on macroscopic spray (liquid) and jet (vapour) characteristics and turbulent combustion. The trends described here are of fundamental importance for analysing the parameter changes that should produce the same trends in the simulations. This chapter also discusses a range of numerical methods that researchers working in the field of combusting fuel spray use. Further, the answer to the first research question, which is based on available literature, is presented in section 3.1.1.3.

A thorough discussion of the used experimental data is offered in chapter 4. This includes sections on the configurations, the operating conditions and the measurement approaches. The chapter is concluded with a critical analysis of the potential deficiencies of the used data.

Chapter 5 first presents the mathematical fundamentals of the CFD tool in which this project is conducted. Then it shows the details of the geometry and meshing strategy that is used for the different engine configurations. The chapter is closed with a section outlining the computational and experimental definitions used to compare the data.

The results and discussions are split into four chapters. Chapter 6 starts by presenting the results for the necessary independence studies of mesh, time-step and parcel introduction rate. The modelling coefficient analysis that discusses the second and third research questions are split in two parts – sections 7.1 and 7.2. The tabulation following that analysis is described in chapter 7.3. In chapter 8.4, the coefficient table is validated against real engine hardware at two load conditions. A preliminary analysis of the droplet-mixing regime relevant to the validity of classical sub models is offered as a supplementary chapter in the appendix.

The summary and conclusions in chapter 10 tie all these topics together and briefly reiterates the objectives of the thesis and critically discusses whether they were met. The thesis is then completed with a summary of avenues of further research as well as the potential outlook of the application of the conclusions.

2 Methodology

This thesis builds upon developing simulation capabilities by introducing complexity gradually. This is done by initially selecting a configuration at simplified conditions that offer a large range of experimental data. The findings in that study are then implemented in an environment, where geometry and engine operation are more representative, but still offers good breadth of experimental data to compare to. Finally, the findings are combined and validated on a real engine condition under the assumption that the previous learnings have led to the physical processes being accounted for accurately. A schematic of the implementation of the experimental data sets is shown in Figure 3.

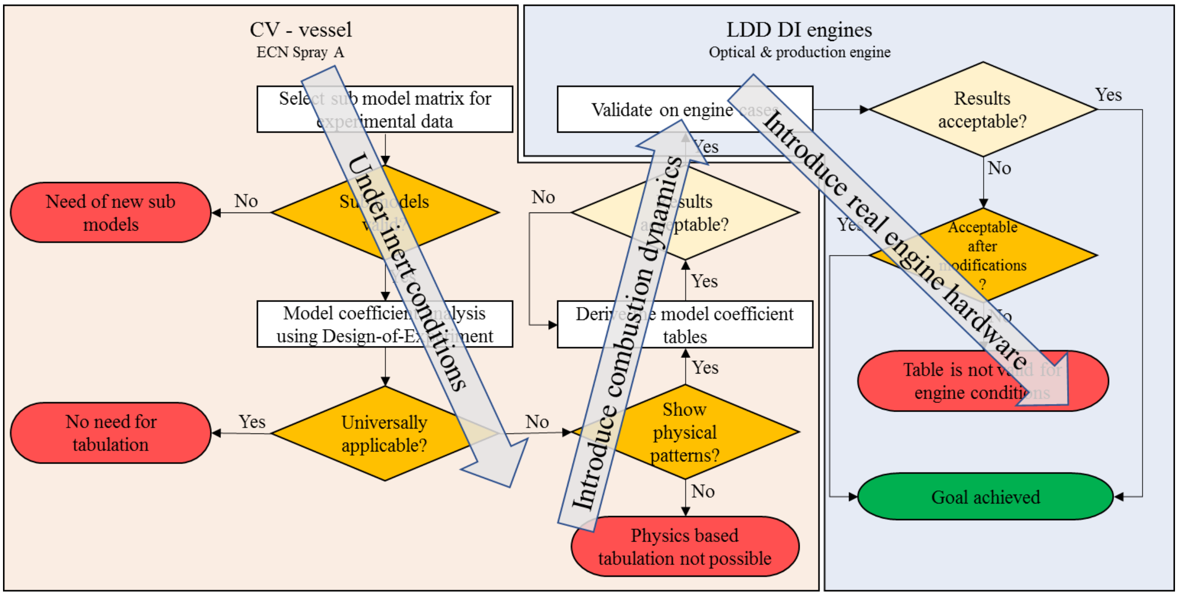

Figure 3: Schematic of the use of the different experimental data sets and gradually introduced complexity superimposed on the decision-making flow chart from (Figure 2)

The choice for the first configuration is the data originating from the ECN quiescent CV chamber. It is widely considered to be robust, well documented, validated and conducted under conditions relevant for part-load Diesel operation. The second data set is from the small-bore optical engine that was used by Sandia National Laboratories (SNL) for research purposes for more than a decade and has recently been included into the ECN's portfolio. While the documentation and experimental control are less elaborate, the engine operating conditions are like those of the CV – chamber. This allows for a transfer of knowledge without major leaps of uncertainties over the effects of boundary conditions because changes can be attributed relatively confidently to a change in engine hardware and operation. For the final validation, a subset of experimental data from a multi-cylinder production engine is used. Ricardo Ltd collected the data as part of ongoing projects, which also means some confidentiality constraints exist. In this full-load case, the engine hardware is very similar to that of the optical engine. Therefore, the adaptations of the simulations can be linked predominantly to the change of boundary conditions. This closes the loop and lays out the scope of this thesis. The experimental datasets will be introduced in detail in chapter 4.

2.1 Selection of sub model matrix

The selection of the used sub models is based on the requirement to run combusting in-cylinder CFD with the lowest possible runtimes without compromising the quality of simulated metrics of interest for engine development. In this work, due to the practical nature of this project, the trade-off is biased toward reducing runtime and recovering lost physical accuracy with smart modelling coefficient strategies. This is reflected in the selection of the sub models. Simple sub models are favoured over correlations that are more complex. Another important criterion is the use of common modelling approaches to allow a high degree of transferability of this work to other simulation frameworks. A detailed literature review in chapter 3 will justify the choice of software and combination of sub models.

2.1.1 Validity of classical sub models

Advances in engine technology over the last three decades have led to a steep rise in thermodynamic gas conditions into which the fuel spray is injected. The ambient temperature and pressure of the gas are typically beyond the critical point of the liquid fuel. The question that arises, is whether the fuel, which all the way up the nozzle is subcritical, will undergo supercritical break-up once injected or will remain subcritical due to aerodynamic and heat transfer processes breaking up the droplet before it becomes supercritical. This is an ongoing topic of research in the scientific community and this thesis will give an overview of the status in the literature review and perform a comparable microscopic analysis of the gas and liquid phase of a selected spray injection condition.

These questions will addressed based on the most recent experimental findings published in literature discussed in section 3.1.1.3. A numerical analysis to investigate these results was also attempted as part of this thesis. Practical limitations to the simulation tool, however, prevented achieving results that were robust enough for the main text. Curious readers can find this analysis in the appendix.

2.2 Analysis of the sub model’s modelling coefficients

The second objective of this work is to analyse the settings of the modelling coefficients in the sub models regarding the governing boundary conditions. A DoE approach with subsequent stochastic process modelling is applied to highlight the responses of changing modelling coefficients on the simulated result.

The Spray A dataset includes a range of parametric variations, which are shown qualitatively in Figure 4. Eight Spray A key points are selected for this objective. These include a discrete injection pressure sweep (KPs 1-3), a simultaneous swing in ambient density and temperature (KPs 1, 4 & 5) and an ambient temperature swing (KPs 7, 9 & 18). The blue key points refer to inert and the red to reactive conditions. The half-blue and red key point stands at the centre of all parametric swings and will be referred to as “the inert or reactive Spray A baseline”. In the next section, the DoE approach is introduced followed by the individual tasks carried out with the different swings is discussed in the next two sections.

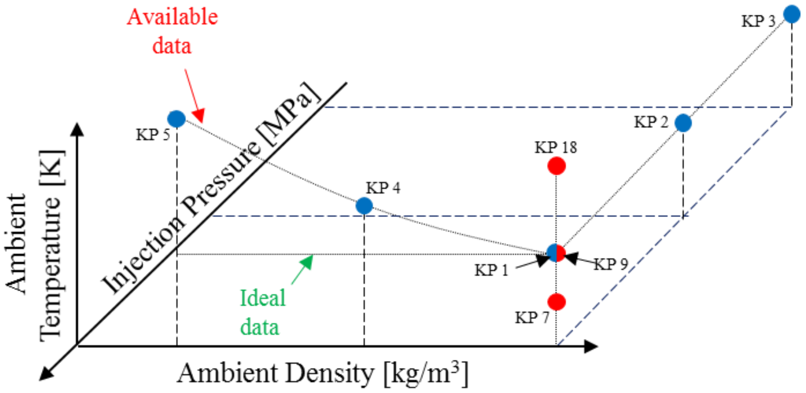

Figure 4: DoE key points for the analysis of modelling coefficients. Blue dots represent inert, red reactive cases

2.2.1 *Design-of-Experiment and stochastic process modelling*

When a system has too many influential and intertwined modelling coefficients to be unpicked in discrete investigations, a statistical approach to analyse the data can significantly reduce the burden. DoE is such an approach. In engine R&D and beyond, DoE is a common tool to visualise complex interactions and sensitivities in the system [2]. Its tasks can be summarised as a tool for:

- Identifying the influence of modelling coefficients on output parameters within a system
- Highlighting the sensitivity of the system towards changing conditions
- Finding a combination of modelling coefficients which produce a desired output

It is important to note that DoE only highlights connections between independent (input) and dependent (response) variables but cannot explain the fundamental processes. For a reliable connection between cause and effect to be made, a statistically relevant number of experiments must be conducted. The mathematical fundamentals of the simulation’s sub model in section 5.1 show that the response of the CFD simulation relies on several user defined modelling coefficients. The DoE software used for this study is a tool called ηCal. The mathematical background of the ηCal tool is given in [3]. It should be underlined that part of the novelty of this work is that the effort is not only limited to identifying links between independent (input) and dependent (response) variables as traditional DoE’s do but also to unveil a physical explanation of these trends.

Few examples of a DoE or other similar response surface modelling in connection with numerical models were found in literature. Work done by Pei *et al* in [4, 5] partially inspired the methodology followed in this thesis. There, they ran dozens of simulations with a range of (1) modelling coefficients [5] and (2) boundary conditions [4] to visualise the most sensitive experimental and numerical modelling coefficients when simulating any direct fuel injection. Pandal *et al* in [6] used a response surface model coupled with an optimiser to find the best modelling coefficient for the simulation to match Sauter Mean Diameter (SMD) measurements. Work done by Brulatout *et al* in [7] uses a DoE approach to reverse-engineer ideal modelling coefficients for two injection pressure conditions.

All four studies are very valuable in highlighting the issue of the two-way sensitivity of modelling coefficients and boundary conditions. However, they stop short of investigating how the values and sensitivities of modelling coefficients change between boundary conditions and whether the change is explainable with the presence of changing physics, a knowledge gap that will be addressed in this work. The publication by Brulatout *et al* in [7] is most closely related to the approach taken in this thesis, however, it stops short of assessing the entire simulation landscape (turbulence, combustion etc.) by focussing on the spray models.

The flow chart in Figure 5 shows the tasks carried out under the ECN Spray A configuration. If the reader is not familiar with the ECN Spray A configuration, it is recommended to skip ahead to section 4.1 where the configurations is thoroughly explained. The inert Spray A was used until step 5. Limited experimental data points prohibited the extraction of any meaningful tabulation but allowed a thorough investigation into the mixing process of the spray and jet. To confirm the findings from the inert conditions and to investigate the transition from inert to reactive, all steps were repeated with an expanded DoE modelling coefficient matrix. The plethora of available boundary conditions here facilitated a detailed physical analysis leading up to the derivation of the tabulation.

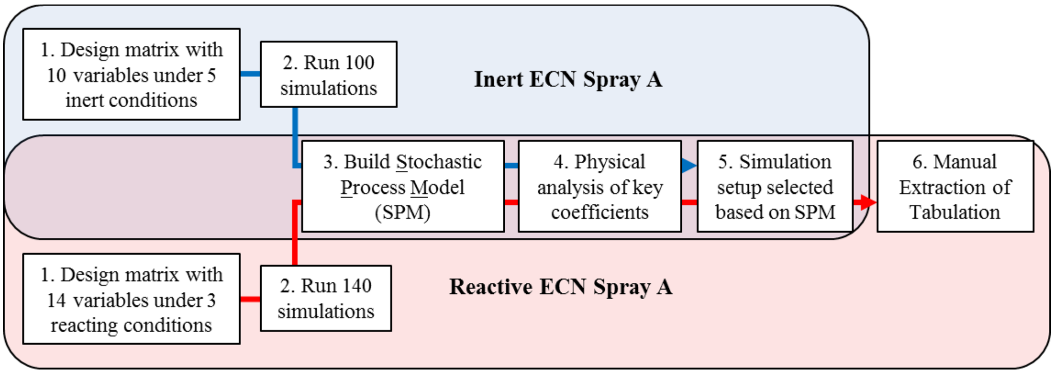

Figure 5: Flow chart of the DoE methodology to derive the tabulated modelling coefficients

Each step will be explained in more detail in the following sub-sections. First, a design matrix for some ECN Spray A conditions with a selected number of DoE coefficients is produced. Every simulation setup in the design matrix has a unique combination of the employed coefficients. Each simulation is then post processed to extract specific response parameters, which can then be used to build the SPMs.

2.2.1.1 *Selection of DoE key points*

The eight DoE key points shown in Table 1 are a subset of the complete list of ECN Spray A key points (to be introduced later in Table 5) that exhibit parametric swings that are of interest for this thesis. The parametric variations include a swing in injection pressure and a simultaneous swing of ambient temperature and density under inert conditions. The reacting conditions are represented with a discrete ambient temperature swing at constant injection pressures. To allow some parametric variations to be “predicted”, no further DoE campaigns for reactive conditions were planned.

Table 1: Selected DoE key points and their parametric variations

Key point	Ambient temperature (K)	Ambient density (kg/m^3)	Chamber pressure (bar)	Injection pressure (MPa)	Injector (#)	Gas composition at SoI (%)
1/2/3	900	22.8	6.05	150/100/50	210677 (SNL)	$O_2 = 0$ $N_2 = 89.71$ $CO_2 = 6.52$ $H_2O = 3.77$
4	1100	15.2	4.96	150		
5	1400	7.6	3.19			
7	800	22.8	5.3			$O_2 = 15$ $N_2 = 75.15$ $CO_2 = 6.22$ $H_2O = 3.62$
9	900		5.9			
18	1200		7.9			

2.2.1.2 *Selection of DoE variables*

For each DoE key point from Table 1, a certain number of variables are selected. For the study of the inert Spray A conditions, 10 variables, and for the reactive Spray A, 14 variables were selected. The DoE variables, their range and phenomenological significance are collected in Table 2. The modelling coefficients that are not included for the inert investigation are marked with a “*”. The importance of the C_1 – coefficient was only discovered after that part of the work had already been concluded and the combustion coefficients play no role under inert conditions. The initial droplet diameter and the half cone angle are not part of any model, are however typically unknown and treated as modelling coefficients. Although the coefficients are grouped, it is important to realise that they are intertwined i.e. an initial condition like the droplet size will influence the mixing and combustion. The selection of these coefficients was based on either literature indicating uncertainty or simulation trials showing strong influence.

Table 2: Selected modelling coefficients and their physical implication

Parameter	**Range**	**Default**	**Phenomenon**
Turbulence Coefficients			
Schmidt Number Sc_t	0.6 – 1	0.6	Species Diffusivity
Coefficient of Dissipation C_1 (-) *	1.35 – 1.55	1.44	Production of Turbulence
Coefficient of Dissipation C_2 (-)	1.65 – 1.92	1.92	Destruction of Turbulence
Combustion Coefficients			
Burning Velocity Coefficient A_0 (-) *	0.3 – 1.5	1	Combustion
Auto-Ignition Coefficient c_{ig} (-) *	0.3 – 1.2	1	Ignition
Turbulent Flame Speed Multiplier α_{turb} (-) *	0.1 – 3	3	Turbulent Combustion
Droplet Break-up Coefficients			
Drag Scaling Coefficient A_{drag} (-)	0.2 – 1.5	1	Liquid/Gas Momentum Transfer
KH B_1 – Coefficient (-)	1 – 40	13	Primary Atomisation
KH B_0 – Coefficient (-)	0.3 – 0.8	0.5	Primary Atomisation
RT C_{RT} – Coefficient (-)	0.3 – 2	1	Secondary Atomisation
RT – C_3 – Coefficient (-)	0.3 – 5.3	5.3	Secondary Atomisation
Levich A_{bu} – Coefficient (-)	5 – 12	11	Primary/Secondary Atomisation
Initial conditions			
Initial Droplet Diameter D_0 (μm)	60 – 90	-	Droplet Introduction
Initial Half Cone Angle α_{cone} (deg)	2.5 – 7.5	-	Initial Dispersion

*Only included for the DoE constant matrix under reacting conditions

The turbulence coefficients and droplet drag factor

Like the spray break-up model, the turbulence coefficients are often altered, but rarely discussed in literature. Some of these are highly influential for the simulation results [8, 9]. In the case of the coefficient values of the turbulence and the droplet drag model, simulation trials uncovered significant sensitivity of the results. Potential reference values from literature were not identified; hence, sensitivity studies were conducted to outline the ranges in preparation of the DoE. The investigation of the turbulent Schmidt number Sc_t and its range were suggested by Ricardo Software because of its less understood effect on the combustion event in the software tool.

Initial trials testing the range on the Spray A conditions first supported the selected range. Only during the validation of the simulations on the engine cases was it revealed that the range was chosen too narrow.

The combustion coefficients

Trial studies focussing on a variety of RTZF combustion model coefficients narrowed down the number of interesting parameters to the listed four. The tested default ranges from the software handbook proved not to be large enough to capture much of the potential variation in heat release and chamber pressure. After further consultation with Ricardo Software to ensure mathematical justification, the ranges were significantly widened to the presented values.

The droplet break-up coefficients

The droplet break-up coefficients (excluding drag scaling factor) from the KH-RT model are the prime examples of coefficients that researchers rely on to adjust their simulations to experiments [10, 11] or leave at default and tune other models [8, 9]. The ranges for the five coefficients are based on a combination of the suggested ranges by the original authors in Beale *et al* [12] and the VECTIS user manual.

The initial conditions

The listed initial conditions were also included after they showed influence on the simulation. The upper limit of the droplet sizes is given under the assumption that the introduced droplets cannot be larger than the nozzle size. The lower limit is not as clear-cut. The final value of 60µm was identified as a result a failed DoE with a range between 75-90 µm suggested the ideal value to be at the lower end of that range. In a future repetition of similar approach, it is recommended to increase this range further, as the validation simulations on the engines showed a stronger sensitivity, perhaps due to the significantly different injector design. The half cone angle was included into the DoE as a result of literature, like Siebers in [13], indicating strong sensitivity to thermodynamic boundary conditions. The ranges were selected based on the measured values of between 5.5° and 7° at conditions closely resembling the ones from this work.

2.2.1.3 *Simulation design matrix*

The DoE software distributes the value of these modelling coefficients randomly across all simulations. A schematic representation of this is provided in Figure 6. Every blue dot represents the value of a test point of the design.

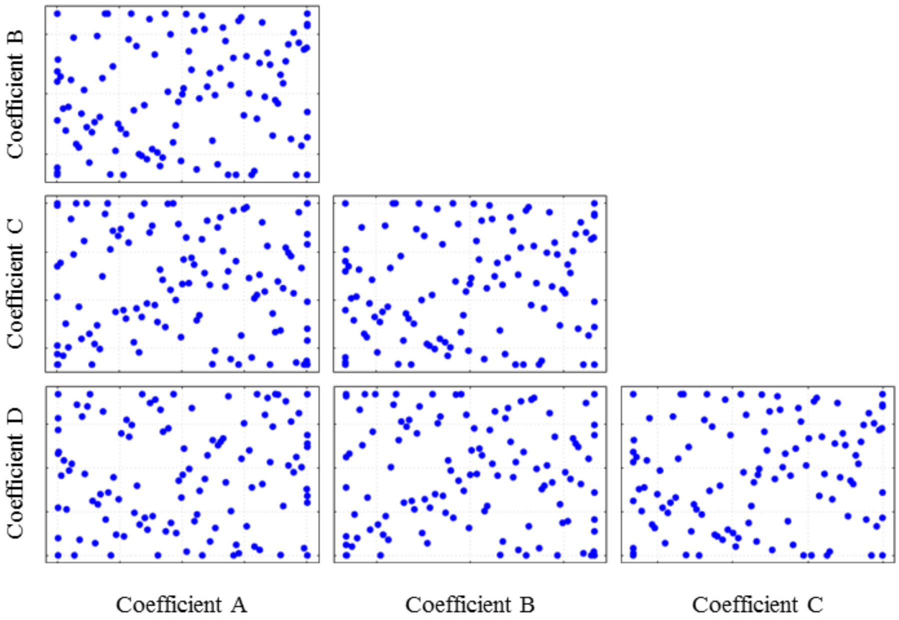

Figure 6: Graphical representation of the design space. Each dot represents the value of a constant in a single DoE simulation. The full picture includes up to 14 modelling coefficients

2.2.1.4 *Stochastic process modelling*

For each DoE key point from Figure 4, 10 simulations per DoE variable are run to ensure statistical relevance. To compare the results between numerical and experimental data, the root-mean-square-error (RMSE) was calculated. This allows a quantification of the similarity between the experimental and calculated curve progressions. To avoid skewed results, extreme transients in the curves are avoided (i.e. Rate of Injection (RoI) ramp up/down).

The mathematical background is described in Table 3. Additionally, a schematic showing an example of the approach applied to the RMSE of spray penetration is shown in Figure 7. This comparison metric is analogously applied to the jet penetration, flame lift-off-length and total heat release. To build the SPM, the matrix of DoE variables together with the responses of the simulations, the RMSEs, are imported into the DoE tool and modelled using a fitting transformation.

Table 3: Mathematical background for RMSE approach

Case	Time-step	Metric Value	No. of time-steps
Experiment	t	$x_{1,t}$	n_t
Simulation		$x_{2,t}$	

$$RMSE = \sqrt{\frac{\sum_{t=1}^{n_t}\left(x_{1,t} - x_{2,t}\right)^2}{n_t}} \qquad \text{Eq 1}$$

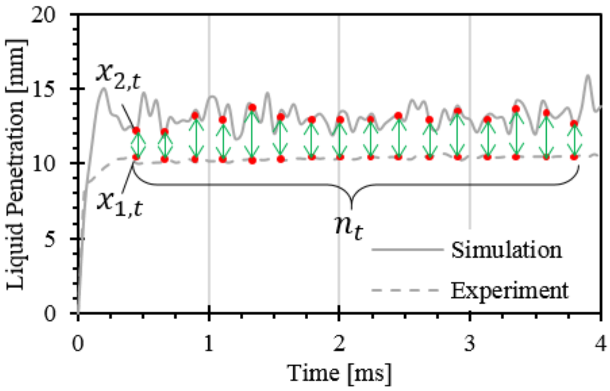

Figure 7: Schematic of data points used to calculate the RMSE shown in an example for spray penetration

2.2.1.5 Quality assessment of the SPM

To assess the quality of the SPM, the DoE tool has a “model quality viewer”, which aids the detection of outliers and evaluation of the model quality with a graphical user interface. The individual criteria will be described first, followed by an explanation of how they are quantified to output a single model quality report.

Outlier detection

To check for outliers, the normal probability plot of the standardised residuals (see Figure 8) is used. This graph is used to verify the assumption of a statistical error having a normal distribution. Single data points that deviate from the reference line, which represents a normal distribution of the residuals, show outlier data points that can be excluded from the model. Should a collection of points deviate from the reference line and exhibit a non-linear pattern, then a transformation of the result should be considered to improve the analysis. Two quality criteria are assessed:

1. The spread of the data points from the centre point
2. The upper absolute value of the standardised residual

Based on these two criteria, the tool recommends which data points should to be excluded to improve the model quality, which in the example shown in Figure 8 would be points 80 and 98.

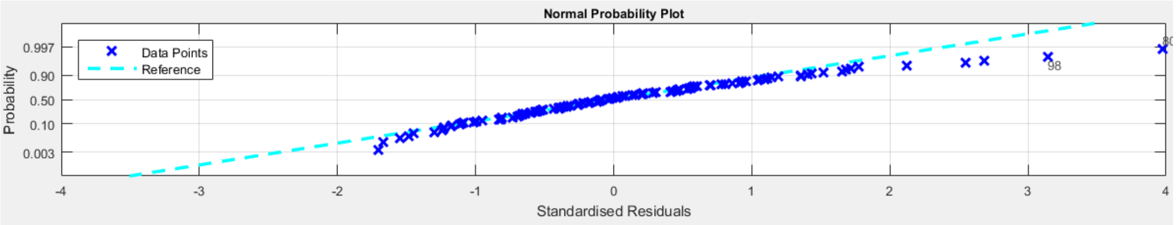

Figure 8: Probability of data points against their reference over the standardised residuals

Prediction residuals and cross-validation

In Figure 9, the residuals are shown in two ways. Both plots show the prediction residuals in magenta and the cross-validation in cyan. The prediction residuals are the difference between the data point and the model prediction. If the residual is positive, the measurement i.e. the RMSE is higher compared to the model prediction and vice-versa.

The cyan circles represent the cross-validation residuals. They show the difference between the raw data point and the prediction from the model if that point were to be excluded from the analysis, which makes them a measure of the predictive quality of the model. In the top graph, the values for cross-validation and prediction are shown over the run number, and below as a function of the RMSE. As a quality criterion, the coefficient of regression R^2 for each model is displayed. The so-called “CV-R^2’- coefficient is based on the cross-validation residual.

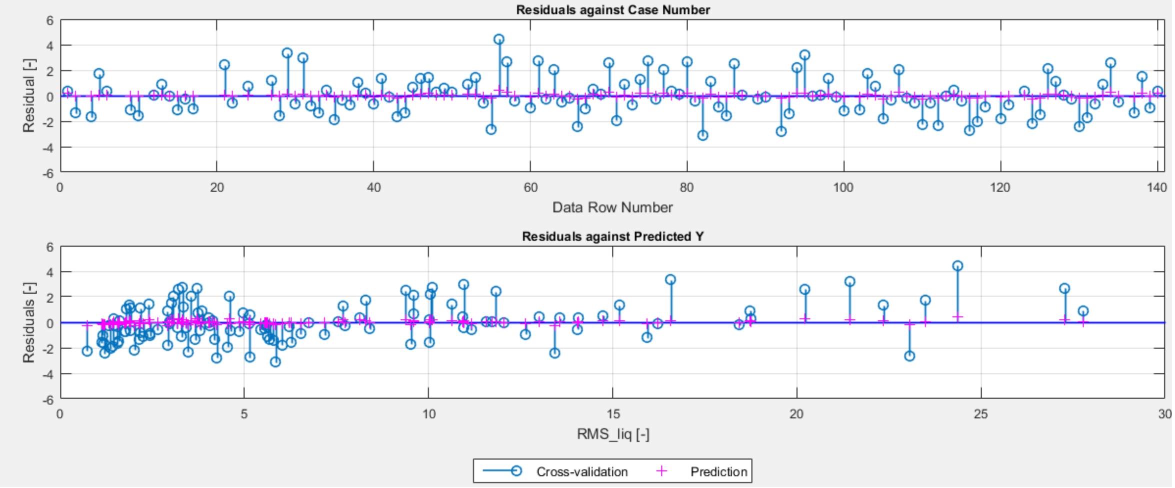

Figure 9: Example of residuals of the prediction and cross validation of each run (top) and for the RMSE (bottom)

Quantitative quality determination

The model is then assigned quality points based on multiple criteria that are summed up into a score as shown in Figure 10. It then receives a rating based on its score (Table 4). For the model meeting the centre point spread and absolute maximum value of the standardised residuals, one point for each criterion is added to its score. Should despite the standardised residuals meeting both quality criteria the CV-R^2 value be between 0.6 and 0.7, the score will be reset to 1 and therefore the model rated as “poor”. On the contrary, should the model fail both quality criteria for the standardised residuals, but have a CV-R^2 value beyond 0.9, the score is set to one. A CV-R^2 value below 0.6 immediately resets the score to 0 (Do Not Use (DNU)), regardless of any other criteria. A good model, which has a score of three, is characterised as meeting both criteria for standardised residuals and having a CV-R^2 value beyond 0.95. A model with the score of two usually meets the standardised residual criteria but has a CV-R^2 value between 0.7 and 0.95. This model is usable, but some caution must be applied.

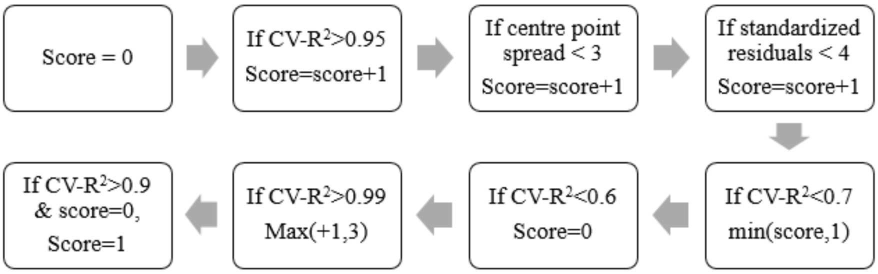

Figure 10: Process to define quality score of model response [14]

Table 4: Model quality rating based on score [14]

Score	Rating	Description
0	DNU	Do not use
1	Poor	Fails most criteria but reflects general response trend
2	OK	Does not meet all criteria but is generally sound
3	Good	Meets all criteria for this response

The majority of SPM’s used in this work have a score of three, which means they meet all the criteria for a good response model. In some cases, where the CV-R^2 value could not be lifted beyond 0.95 without discarding too many key points but remained in the upper end of the range between 0.7 and 0.95, a score of two was accepted.

2.2.1.6 Local optimisation

The DoE software provides an inbuilt optimiser that uses the SPM to achieve a defined target – in this case the reduction of the RMSE to a minimum. The optimiser can handle up to a maximum of three simultaneous targets. When one target is set, the optimiser will find a single best setting. When two or three target conditions are set, it will produce a Pareto curve or surface respectively. Hence, depending on the number of selected targets, the result of the optimisation is a map of multiple solutions.

2.2.1.7 Weaknesses of the DoE approach

In short, the DoE approach is only as good as its inputs. This means that while the statistical modelling and quality control within the model setup are sound and well validated, setting the right boundary conditions is more difficult. The DoE model relies on the following aspects:

- The selection and range of the modelling coefficients
- The selection and quality of the response metrics
- The availability of experimental data at representative conditions

Regarding the first point, throughout this study modelling coefficients were added, removed, and their ranges adapted. Although the selection of modelling coefficients in Table 2 was continuously improved, after every DoE run some indications remained that some ranges should have been larger or more modelling coefficients included. There are two limitations to both points. Regarding the former, ever expanding the investigated range of a constant also increases the risk of including non-physically plausible results that still produce good results for plain numerical reasons. An example of this is that in some cases the DoE found a drag coefficient value of $A_{drag}>1$ to be favourable. In our definition of A_{drag}, this would mean increasing the drag coefficient of the droplet to that beyond a sphere, which is physically unreasonable. The second point, adding more modelling coefficients, has a practical runtime limit. Each coefficient increases the number of simulations by 10, which for the reactive cases means around an extra 70hrs of simulations. Since this work was done in a commercial environment, there was always a strong incentive to hold runtime and cluster occupation to a reasonable level.

The selection of the response metrics, which will be extensively discussed in chapter 5, plays a big role for the quality of the model design. Since the experiments were not conducted in-house, no information beyond the literature are known. Then there is the selection of the sections of the data that are used for the calculation of the RMSE. Deriving the RMSE based on metrics that are highly transient can lead to high errors. To avoid this, either highly transient regions are clipped resulting in some events becoming less well represented or a smoother derivative of the metric is used. An example of the former is the RoI ramp up effect on spray penetration. The simulations often show a spike of liquid length before stabilising at a steady state. It is not entirely clear, if these simulated spikes are a numerical effect or if they are physical, but not captured well by experiments. An example of the use of a smoothed derivative is the capturing of the auto-ignition event. The clearest evidence of auto-ignition can be found in the RoHR curves. The problem with these curves is that they show extreme gradients and are filtered as derivative of the pressure curve. Calculating the RMSE based on this metric could lead to high total errors although the curve characteristics are otherwise nearly identical. For this reason, the smoother total heat release is selected. However, when using this metric, the exact timing of auto-ignition is partially supressed.

The final problem arises with the selection of the comparison metrics. While most aspects of the macroscopic spray, jet and combustion characteristics are well resolved with the current selection of metrics, there is a gap in the availability of representative near nozzle droplet statistics. The current selection of comparison metrics struggle to resolve the microscopic processes of the droplet injection and break-up process. This means that coefficients like for the break-up coefficients and initial droplet sizes are not well understood because they predominantly affect the microscopic droplet evolution. Hence, an attempt at characterising these coefficients is based on their macroscopic effect. For the initial droplet sizes, some measurements at somewhat relevant conditions are available so a tabulation could be based on literature rather than the produced SPM’s. Once technological advancements make the measurement of this metric possible, this approach could be expanded to include microscopic data to fine-tune the droplet break-up and evaporation.

2.2.2 Universal validity of coefficients

Following the flow chart from Figure 2, the second research question to answer is whether there exists a selection of modelling coefficients within a set combination of sub models that can produce acceptable simulation results as defined in section 1.4.2 for multiple metrics at various boundary conditions. A local optimiser (see section 2.2.1.6) uses the SPM of the inert Spray A baseline (KP 1) to find the best simulation setup. This setup is then used for the other four inert key points (KPs 2-5).

2.2.3 Physical-mathematical analysis of modelling coefficients

Should a single simulation setting not be universally applicable, a study into the physical and mathematical background of the modelling coefficients is to be carried out to identify potential links between the boundary conditions and the coefficient values (third research question). This is done by running all DoE's and using the SPMs to find the individual combination of modelling coefficients for each condition that produce a good match between simulations and experiments. The next step is to highlight the sensitive and insensitive modelling coefficient by comparing their values between the different key points (shown as schematic in Figure 11). If the modelling coefficients are insensitive to the changing boundary condition, then it can be assumed that the sub model they are embedded into considers the physical process sufficiently well. If the contrary applies, and the optimum coefficient value changes with boundary condition, the sub model is not sophisticated enough to account for the changing physical process.

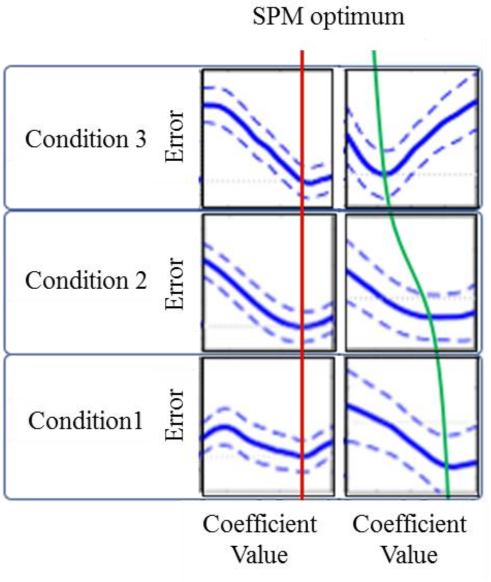

Figure 11: Schematic of sensitive (green) and insensitive (red) modelling coefficients against changing boundary conditions

This investigation is done for all DoE key points but with differing focus depending on the whether the condition is inert or not. The experimental data for the inert condition offers more details for the spray evolution like spray and jet penetration, radial and axial mass fraction and gas temperature distributions. If all these characteristics are matched well, it allows for a high degree of confidence in the simulation setup's capability to deal with the spray break-up and mixing process – the key ingredients for the combustion process. The use of the reactive cases is twofold. Firstly, since they are performed chronologically after the inert conditions, they serve as a first validation of the simulation coefficients found to work for inert conditions. Secondly, additional modelling coefficients, which are influential for combustion, are introduced.

2.3 Coefficient tabulation

The next step is to derive the tabulation of the modelling coefficients for more parametric variations than shown in Figure 4. A qualitative schematic of the distribution of all Spray A key points is given in Figure 12.

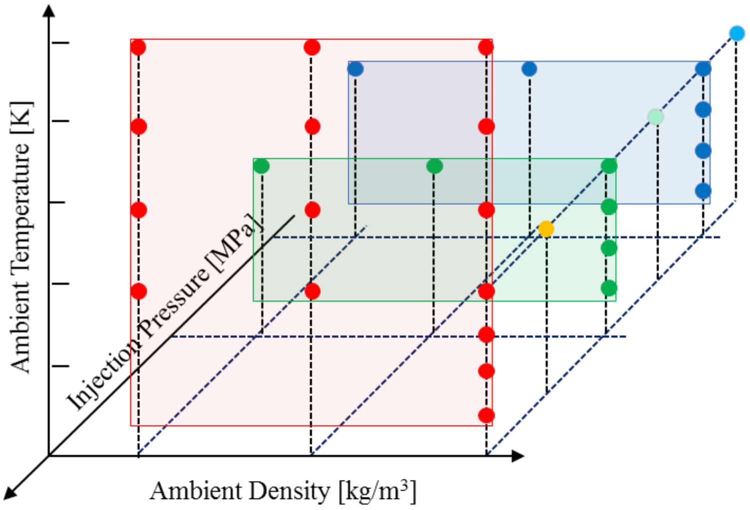

Figure 12: Schematic of the final grid of the extent of the tabulated setup

Using the found connections between the physical and numerical changes derived from the SPMs of the DoE key points, a range of parametric Spray A variations are simulated. The coefficient values that were used for a successful match were recorded in a tabular format. Of highest priority here is that the change in coefficient is physically plausible and not arbitrary. Fulfilling this criterion is the most challenging of this thesis, but also what lends it its innovative nature. To the best of my knowledge, neither the tabulation of modelling coefficients nor an extensive attempt to connect modelling coefficients to physical processes has been attempted. The initial results for this work are published in Nsikane *et al* [15]. The detailed analysis, i.e. the continuation of Nsikane *et al* [16], are at the point of writing under review.

2.4 Tabulation validation

To test the performance of the modelling coefficients derived from the table on realistic engine conditions, two light-duty engines were selected. One is an optical engine that is operated at part-load and the other is a production engine operated at full-load. The optical engine is selected due to an extensive dataset and a solid publication history as well as comparable geometric specifications with the production engine and boundary conditions at SoI that could be considered well within the area of confidence of the coefficient tables. This means that to derive the coefficients, simple interpolation between surrounding key points Figure 12 was possible.

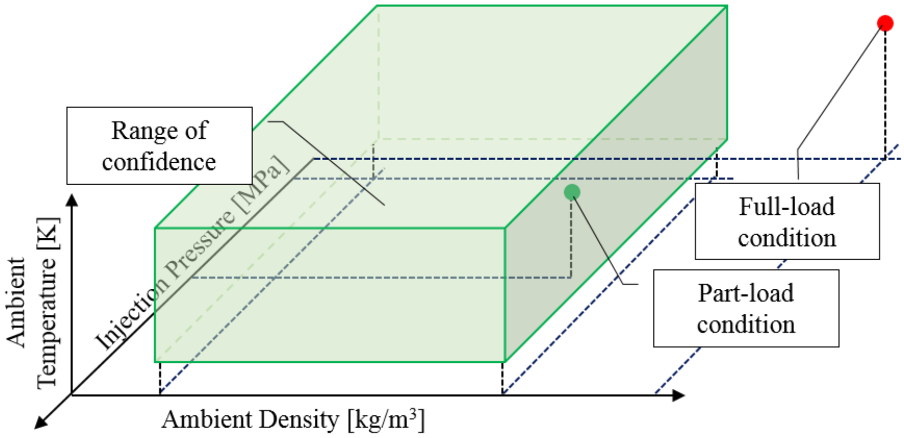

Figure 13: Range of confidence of the tabulation (green box) and the relative location of the boundary conditions of the two selected engine conditions to validate the coefficient table.

The operating point of the production engine is selected as it represents classic full-load operation. The derivation of the modelling coefficients for this case requires multidimensional extrapolation from the range of confidence (see Figure 13). The results of this study are published in Nsikane *et al* [17].

2.4.1 Identification of necessary adaptations

The transition from the CV – chamber to real engine conditions is not expected to work without necessary changes. The fundamentally different operation of engines includes moving parts, steep thermodynamic gradients and increased turbulence levels. An analysis into the effect of these differences will guide the targeted modifications of selected modelling coefficients to match these conditions.

3 Relevant literature

3.1 Physical processes governing the injection process

In direct injection combustion systems such as in modern Diesel engines, cold liquid fuel is injected at high velocities into a hot and pressurised environment with a given gas mixture. This configuration means that steep temperature, pressure, density and velocity gradients exert physical forces upon the liquid fuel at nozzle exit breaking up and vaporising the liquid core over time. As the fuel/air mixture further propagates in time and space, temperature dependant chemical processes trigger a combustion event with subsequent emission formation.

In most experiments discussed in the literature, the spray break-up and combustion processes are typically measured with macroscopic metrics. These are the spray & jet penetration, Ignition Delay (ID), flame Lift-off-Length (LoL), chamber pressure rise, heat release and emission mass fractions. What is of interest for this thesis is how these measures depend on outside boundary conditions. This section contains a review of older and current research on how thermodynamic conditions like ambient density, temperature and pressure and injection parameters like injection pressure and orifice diameter affect the above-mentioned spray metrics. Since one of the main goals of this work is to derive a simulation approach that is as physically accurate as possible, the simulation results will frequently refer to the trends found in this section.

The section will start with a description of the sensitivity of droplet sizes. Although not a main metric due to ambiguous experimental data, they are an important aspect of multiphase flow simulations in this area. In recent years, improving experimental data has begun to allow some conclusion to be derived. After an analysis of the microscopic spray follows a discussion of the sensitivity of the macroscopic spray & jet penetration and lift of length.

The following sub sections will always be headed with an introductory explanation of the importance of the metric followed by a short summary of the key findings. This is followed by the detailed discussion within the sub section itself. A dataset called ‘Spray A’ will be mentioned regularly throughout the review. ‘Spray A’ is a dataset collected by the Engine Combustion Network (ECN) and was extensively used in this thesis. Much of the detailed analysis of spray characteristics were performed on this dataset. A comprehensive summary of Spray A will follow in section 4.1.

3.1.1 Microscopic spray characteristics

For liquid fuel injected combustion systems, the structure of the liquid flow field is fundamental for the air-fuel mixing and combustion process as well as emission formation. Information about the flow field is crucial for physical representation of the liquid phase evolution in numerical approaches. The problem is that acquiring experimental data to characterise the liquid during the high-speed injection process is very challenging. An extensive review of the challenges and capabilities of developing optical imaging techniques is given by Linne in [18]. Since the writing of that review, technological advancements have improved the optical imaging capabilities, but there remain some stubborn difficulties. The key problems remain to-date that the optically dense region of the spray prohibits light to pass through the spray hindering optical measurements in this region. This is the reason that the data is typically either available from the less dense outer region of the spray or measured during phases of the injection where measurements are easier like RoI ramps. However, the dense region of the spray is where most of the liquid mass is and is therefore of greater importance. Some measurement techniques like USAXS [19, 20] and ballistic imaging [21, 22] are to an extent capable of resolving the dense region of the spray. The results from these have been valuable in improving understanding of the physical implications of changing operating conditions relevant for this thesis.

The second discussion in this section is on the validity of classical spray models for the spray (and similar) configuration. A shift of a liquid droplet from classical atomisation and vaporisation (subcritical) into the supercritical regime is characterised by the reduction of liquid droplet surface tension. This phenomenon occurs at a combination of high temperature and high pressures above the critical point of the fluid. In common Diesel injection conditions, the liquid fuel all the way through the injector is subcritical. However, the ambient gas the liquid is injected into is typically in the supercritical regime of the fuel. As the fuel exits the nozzle, heat transfer processes will elevate the temperature of the fuel while simultaneously reducing the local temperature and pressure of the surrounding gas. There is still ambiguity among the scientific community as to whether a cool spray injected into a supercritical environment ultimately represents a supercritical spray or not.

The most relevant findings, which will all be discussed in-depth in the sub-sections, are the following:

- Increasing ambient density reduces droplet Sauter Mean Diameter (SMD) [19]

- Rising chamber temperatures prevent droplet coalescence that occurs at increasing chamber densities and thus reduces probability of large droplets forming [23-25].
- Increasing injection pressures decrease droplet SMD [19, 20, 24, 26, 27].
- The baseline Spray A is in the subcritical mixing regime, while parametric variations with temperatures beyond 1100K enter the trans-critical regime [21, 22, 28].
- Even when the liquid enters the trans or supercritical regime, there is still a finite transition time where the droplets show clear signs of surface tension [28].

3.1.1.1 Effect of ambient density and temperature on droplet size distributions

Shear or deceleration of the liquid are considered the main contributors to droplet break-up. Both aspects are increased when ambient densities are raised. Figure 14 from Kastengren *et al* shows the droplet SMD of a non-evaporating variation of the Spray A baseline along the centreline (optically dense region) of the spray at two different ambient pressures using a USAX imaging technique. The SMD represents the diameter of a sphere whose volume is equal to the summed volumes of the sample. From the figure it becomes clear that higher ambient pressures, and by extension ambient densities if the temperature is held constant like here, promote smaller near nozzle droplet sizes.

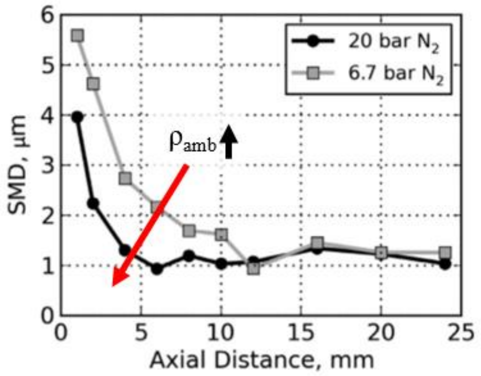

Figure 14: Effect of ambient pressure (and by extension, density) on the SMD along the spray axis of the non-evaporating Spray A condition [19]

Experimental findings from Nawi *et al* [23] shown in Figure 15, show the effect of a discrete increase of ambient density on the Probability Distribution Function (PDF) of droplet diameters at 0.6ms after Start of Injection (ASOI) in the vicinity of the nozzle outlet (optically thin region) for two temperature conditions. At ambient temperature T_i=500K, the droplet PDF shows higher probability of larger droplets for the higher density condition. In contrast to the authors, who argue that the reason for higher probability of large droplets its due to droplet evaporation of small droplets, stands research by Chi *et al* in [24] who highlight the tendency of droplets to coalesce under high pressure if the temperatures are too low to evaporate the initially smaller droplets. While this publication is potentially out of date, recent research by Jeon and Moon on fuel injection with a Gasoline Direct Injection (GDI) hollow cone injector in [25] strongly suggests increasing droplet coalescence under increasing ambient densities and non-evaporating conditions (see Figure 16). The logic laid out in Chin *et al* in [24] and Jeon and Moon in [25] then allows the conclusion that when the ambient temperature is increased to T_i=700K, evaporation is enhanced and coalescence supressed. In contrast, the explanation by Nawi, that smaller droplets would evaporate only leaving large droplets behind to be measured, should mean that the probability of large droplets should still prevail because small droplets have already evaporated. Hence, the inclination of this thesis is to follow the argumentation by Chin *et al* in [24] and Jeon and Moon in [25].

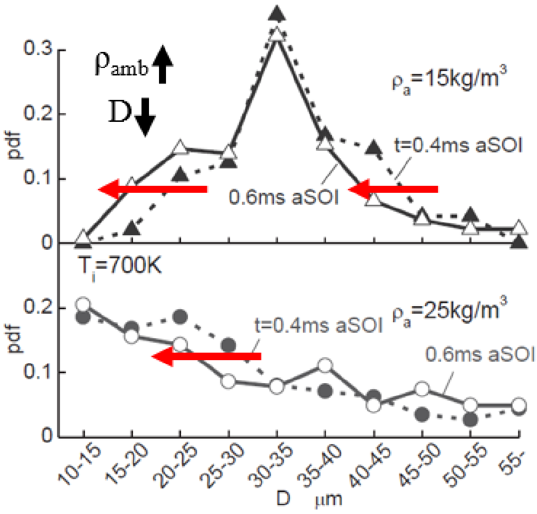

Figure 15: Effect of ambient density on droplet size distribution near the nozzle at 0.6ms ASOI [23]

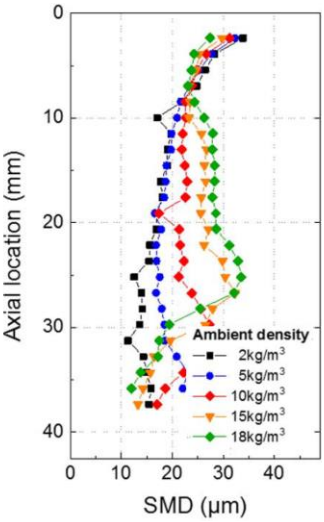

Figure 16: Effect of ambient density on local SMD distribution for hollow cone GDI injector [25]

All three publications agree increasing densities lead to decreased near nozzle droplet sizes. Chin *et al* in [24] explains this based on the effect of the Weber number being proportionally higher with increasing density. This leads to increased droplet instability and enhances break-up.

3.1.1.2 Effect of injection pressure on droplet sizes

There is a consensus among researchers (for example [19, 20, 24, 26, 27]) that with increasing injection pressures, the droplet SMD reduces. This trend can be clearly seen in Figure 17 from Kastengren *et al* [19]. Higher injection pressures, which are synonymous to higher droplet velocities, means that shear between liquid and gas is increased due to increased relative velocities. Increased shear results in accelerated break-up.

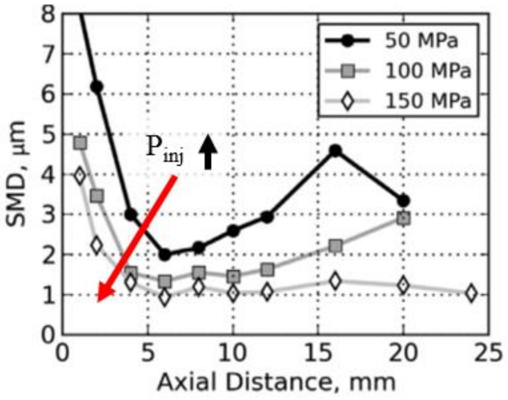

Figure 17: Effect of injection pressure on the SMD along the spray axis for the ECN 210675 injector under non-evaporating conditions [19]

3.1.1.3 Droplet mixing regime of ECN Spray A

It is generally very difficult to observe the highly dynamic diffusive mixing (supercritical evaporation) process of droplets experimentally primarily due to technical limitation of the equipment [29-31]. The absence of conclusive results has led to researchers trying to identify supercritical characteristics of flows based on secondary evidence like macroscopic changes in the physical appearance of the plume [21, 22, 32]. Work done by Falgout *et al* in [21, 22] used the ballistic imaging technique at the periphery of the optically dense region of a spray closely resembling Spray A. There they identified an onset of characteristics that place the droplets at the spray periphery near, but not in the trans-critical mixing regime. Crua *et al* in [28] eventually succeeded in capturing the droplet break-up and evaporation process and developed a conceptual model of the droplet mixing regimes shown in Figure 18.

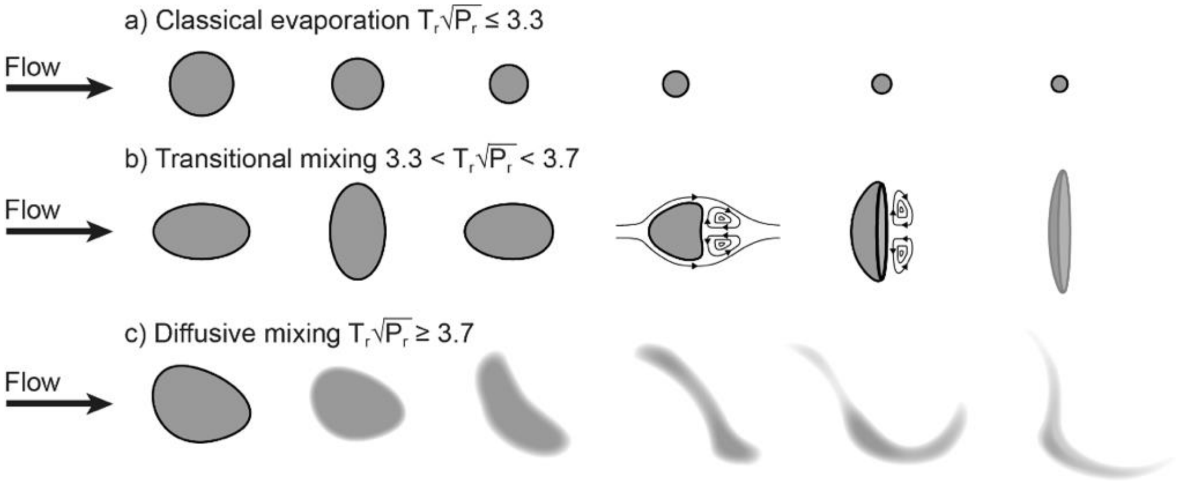

Figure 18: Conceptual model of droplet mixing regimes [28]

Their work was based on a range of single component fuels injected through a single-hole injector into a quiescent vessel at various operating conditions. The authors show clear evidence that despite the ambient conditions being supercritical, surface tension and primary atomisation for n-dodecane can be observed, hence categorising the spray well within the ‘classical evaporation’ regime. They further show that even in cases where ambient conditions are so extreme that the fuel ultimately undergoes diffusive mixing, there is still a finite transition time that depends on local gas temperatures, pressures and on the fuel’s physical properties. This finding is of fundamental importance for this work because it justifies the use of the classical sub models which usually account for surface tension effects and would potentially not be valid for flows entering the “transitional mixing” regime or beyond. Recent attempts of simulations of supercritical flows can be found for example by Chung *et al* in [33].

Despite the results from Crua *et al* in [28], some technical limitations to their approach are important to highlight. A visualisation of the individual droplets was only possible at the end of injection for relatively slow droplets and in an optically thin region of the spray. Physical processes within the core or the optically dense region of the spray remained unresolved. This is where CFD has the potential to offer some insight by assessing the thermodynamic conditions in the optically dense region, so that a categorisation of the droplet mixing regimes can be attempted. The Spray A variations investigated here were also central conditions in the work by Crua *et al* in [28] where they developed a droplet mixing regime classification system (see Figure 19).

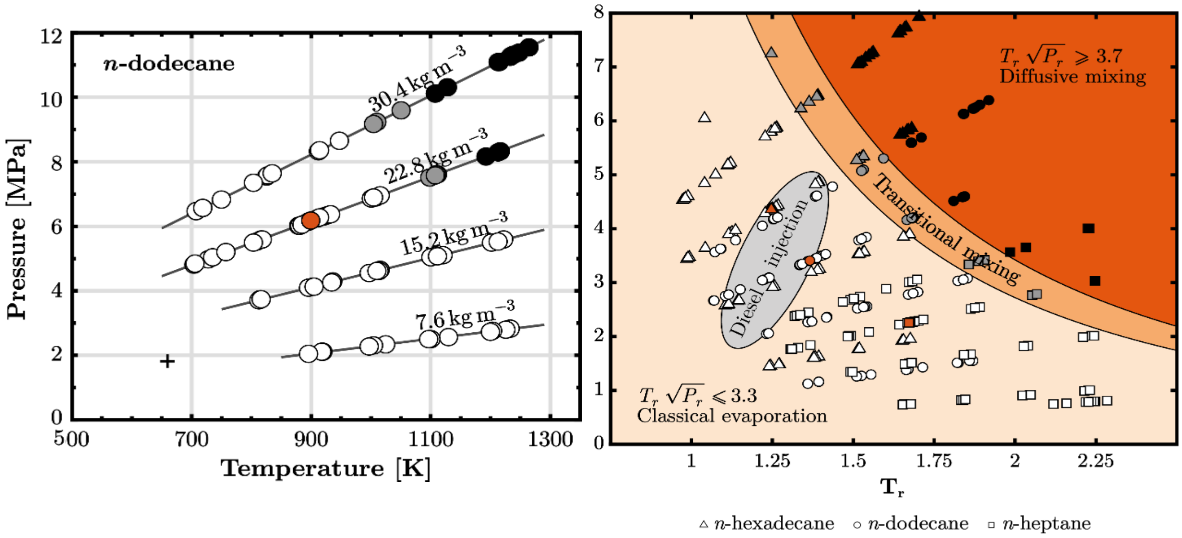

Figure 19: Gas pressure-temperature diagrams for n-dodecane (left). The left diagram is then projected onto a classification of mixing regime diagram on the right. Both Pr and Tr are calculated by dividing the imposed far-field (Pg,Tg) values by the critical values of the fuel (For n-dodecane Pc = 18.2bar, Tc = 658K). (Reproduced from [28], red symbols indicate the operating conditions examined in this thesis.)

The left image shows the nominal chamber pressure over ambient temperature of a range of operating conditions. Following this, the axes were normalised by dividing the far-field values (Tg, Pg) by the fuel specific critical temperature and pressure values Tc and Pc. A regression model with the best fit at $T_r\sqrt{P_r}$ allowed the automated classification seen on the right image.

Summary of mixing regime analysis

The literature discussing the mixing regime of Spray A is still scarce, but overall suggests convincingly that liquid fuel may still qualify as subcritical and therefore be treated with classical evaporation equations even if the ambient gas conditions are nominally in the supercritical regime of the fuel. The reason for this is the thermal inertia and rapid disintegration of droplets that break-up and evaporate the droplets before they reach supercritical conditions. Then there is the hypothesis that a continuous injection of cool spray leads to a local drop in temperature and pressure that may produce a subcritical zone within an otherwise supercritical environment. Based on the evidence in the literature, this thesis sees the first research question answered as follows:

Answer to research question 1

Using a combination of findings from literature and a numerical analysis of the gas phase of the injection duration of the inert Spray A baseline, it is shown that a continuous injection of cool liquid fuel leads to a reduction of the local ambient temperature below the critical point.

Numerically defining the mixing regimen of the droplet in Spray A is difficult because the used simulation package bases its equations in the assumption that the spray is subcritical. Nonetheless, as part of this work, it was attempted, and initial results were promising. However, practical limitations to the simulation tool prevented the analysis from being robust enough to be included in the main body of the thesis. Curious readers can find this analysis in the appendix.

3.1.2 Spray penetration

Injection pressure, injector orifice diameter and ambient conditions play a major role in designing the combustion system. Each of these aspects affect combustion performance in their own distinct way. Their effect on spray penetration must be understood to reduce emissions, avoid piston bowl impingement and set turbocharging conditions.

An elaborate investigation of the parametric dependencies of Diesel fuel spray penetration was conducted by Siebers in [13]. He investigated the effects of the orifice diameter, orifice pressure drop and ambient thermodynamic conditions. This is not an exhaustive list of factors that influence spray penetration but rather highlights the main aspects that will also play a major role in the results of this work. His results can be summarised as follows:

- Liquid length is linearly dependent on orifice diameter regardless of fuel or thermodynamic boundary conditions (see Figure 20).
- Liquid length decreases slightly injection pressure regardless of fuel or thermodynamic boundary conditions (see Figure 21). Similar findings were reported in Yeh *et al* [34], Kanimoto *et al* [35] and Hawi *et al* [36].
- Fuel volatility (i.e.boiling point) is an influential factor for low ambient temperatures. Lower fuel volatility results in longer liquid lengthts. With increasing ambient tempretures this effect diminishes (see Figure 23). These findings are consistent with observations in Browne *et al* in [37].
- Ambient gas densities and/or gas temperatures have a significant effect on liquid length. The sensitivity however reduces at both higher temperatures and densities (see Figures 22 and 23). This has also been observed by Epsey *et al* [38].
- The liquid length decreases linearly with increasing fuel temperature. The inclination is dependant on the thermondynamic boundary conditions and fuel volatility (see Figure 24).

3.1.2.1 Spray penetration dependency on injection pressure and orifice diameter

The fact that liquid length is almost independent of injection pressure but not of orifice diameter (see Figures 20 and 21) suggests that the liquid length is predominantly determined by air entrainment (or turbulent mixing). This is because in turbulent mixing, the local interphase transport rates of mass, momentum and energy (which determine liquid break-up) must be fast relative to turbulent mixing rates. As such, the turbulent mixing defines the rate at which energy is entrained into the spray. Therefore, while a change in orifice size cannot provide the spray with enough fresh gas to be entrained, an increase of fuel mass at constant orifice size can always be matched with enough fresh gas.

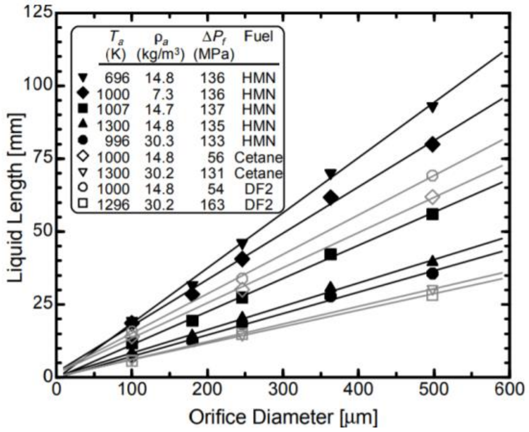

Figure 20: Liquid length versus orifice diameter for a wide range of conditions [34]

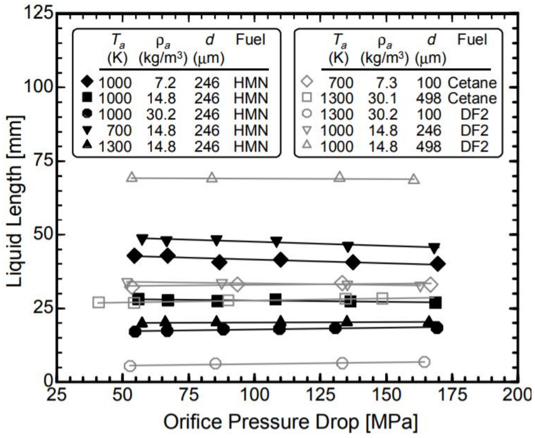

Figure 21: Liquid length versus the pressure drop across the injector orifice [34]

3.1.2.2 Penetration dependency on ambient density and temperature

The effect of gas density on the spray penetration is related to the above-mentioned turbulent mixing. An increase of ambient density comes with an increase of carried energy in the air. The proportion of this is to the square root of the gas, leading to the strong non-linear effect. Additionally, higher gas densities increase the spreading angle of the spray, which in turn entrains more gas. The reason for the decrease in spray penetration at rising ambient temperatures is straightforward. Due to the hotter air, which carries more energy, that is being entrained, less time in required to break-up the droplets (see Figures 22 and 23).

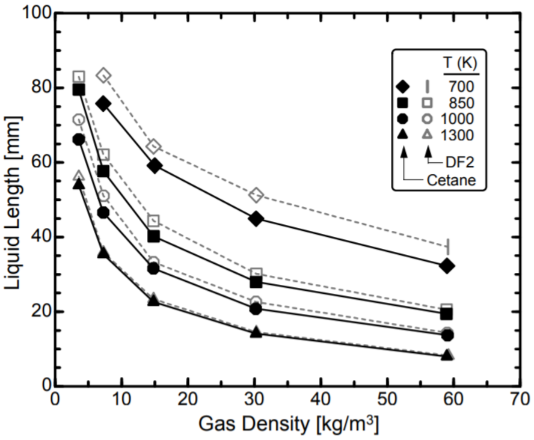

Figure 22: Liquid lengths for the single component fuel cetane with the multicomponent DF2 [13]

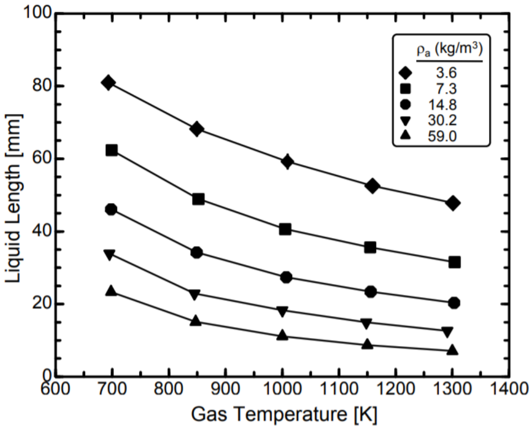

Figure 23: Liquid length as a function of gas temperature for five gas densities [13]

This also plays a role when volatility of the fuel is considered. Fuels with lower volatility have longer liquid lengths. Highly volatile fuels require less exposure to heated air to undergo the break-up process leading to the clear difference between the liquid lengths of different fuels. Other, more complex, factors such as thermodynamic properties of the fuel like temperature dependent vaporisation heat, saturation pressure and temperature and heat capacity also play a role.

3.1.2.3 Spray penetration dependency on fuel temperature

The turbulent mixing process is also the main contributor to the spray penetration dependency on fuel temperature. As Figure 24 shows, hotter fuel requires less energy supply from the entrained gas to be broken up. The result is reduced spray penetration with increasing initial fuel temperatures.

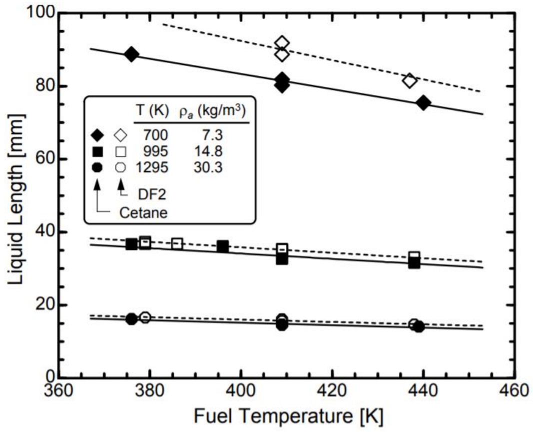

Figure 24: Liquid length versus the injected fuel temperature for three different ambient gas conditions and two different fuels [13]

3.1.3 Jet penetration and mixture fraction

A good understanding of the mixing process between ambient gas and fuel is crucial to predict the temporal and spatial Start of Combustion (SoC) and emission production. Numerical combustion models use the mixture fraction combined with the thermodynamic conditions as triggers to start the combustion event. Further, emission models can only give reasonable results if the spatial mixture fractions are well approximated. The main findings are:

1. Increasing injection pressures increases jet penetration rates (Heikki *et al* [39] and Pickett *et al* [40])
2. A decrease in chamber density increases jet penetration rates (Pickett *et al* [40])
3. The mixing at a given spatial location is independent of injection velocity [40-44]
4. The mixture fraction increases with a decrease in the ambient density at a given axial position. [40-44]
5. A combustion induced local drop in density leads to a brief pause in deceleration of the vapour cloud (Pickett *et al* [45] and Pastor *et al* [46])

3.1.3.1 *Effect of injection pressure on jet characteristics*

This first analysis is focussed on the effect of injection pressure on the vapour phase. Figure 25 shows a time resolved plot of jet penetration at three incrementally increasing injection pressures. At this point, the simulations in solid red will be ignored and only discuss the experimental data. Heikki *et al* stipulates in [39] that the increase in jet penetration rate at higher injection pressures is caused by the higher relative liquid phase velocity which in turn induces higher gas velocities and turbulence levels.

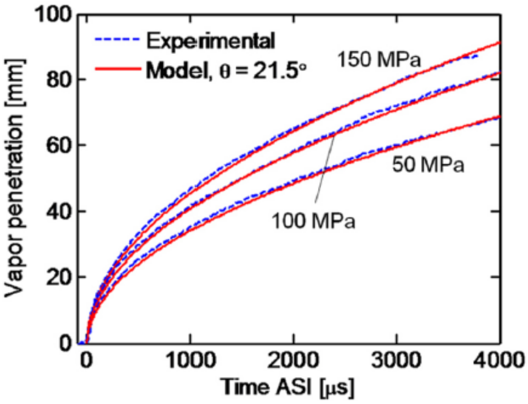

Figure 25: Time-resolved jet penetration at three injection pressure conditions [40]

Figure 26 shows the mass fraction distributions along the plume axis (top row) and across the plume cross section (bottom row) for incrementally increasing injection pressure conditions (columns). The data were collected during the steady state phase of the injection.

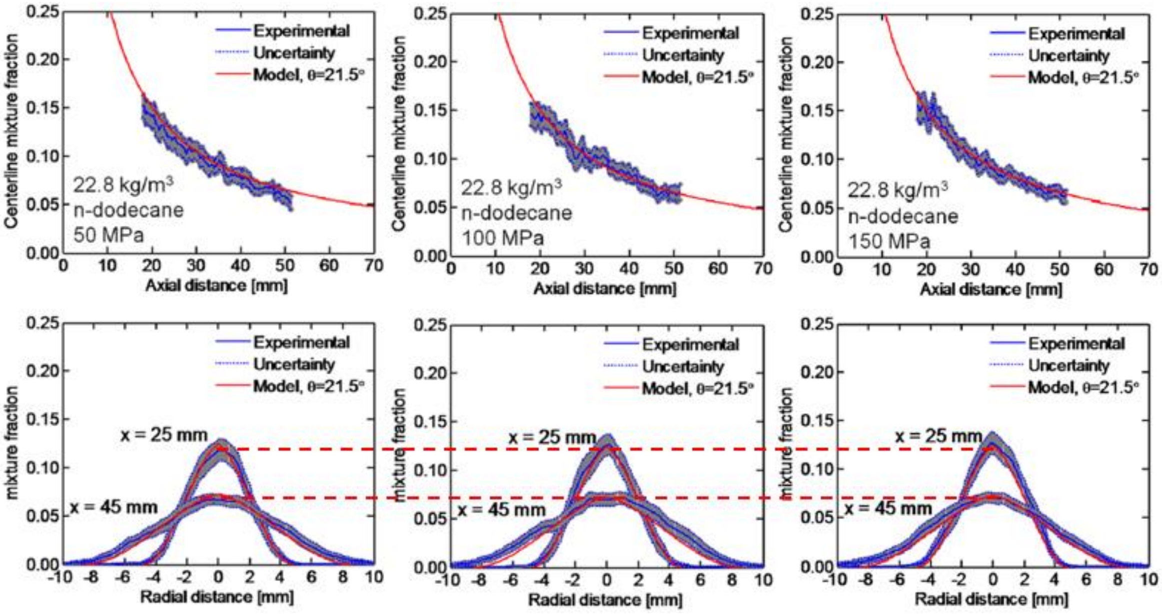

Figure 26: Fuel mass fraction distributions across the plume axis (top) and cross section (bottom) at given axial locations and time for three operating conditions. Injection pressures rise from left to right (reproduced from [40])

The experimental data in Figure 26 show that the mixture fraction distribution is independent of injection pressure. The red dashed line is added to highlight the indifferent peaks of radial mass fraction distributions at both locations under all three conditions. This agrees with a range of findings where it is stated that at steady state, spreading angles are not affected ([41-44]), spray penetration remains roughly unchanged ([13] & discussed in section 3.1.1.3) and flame lift-off is independent ([47-50] & will be discussed in section 3.1.5). All these aspects highlight that air entrainment remains constant at rising injection pressures.

3.1.3.2 Jet tip penetration dependency on ambient density

The dependency of the evolution of jet penetration over time on ambient density of two similar experiments is shown in Figure 27. The left graph from Pickett *et al* in [40] shows the simultaneous density and temperature variation while the right graph from Hawi *et al* in [36] shows a discrete density swing.

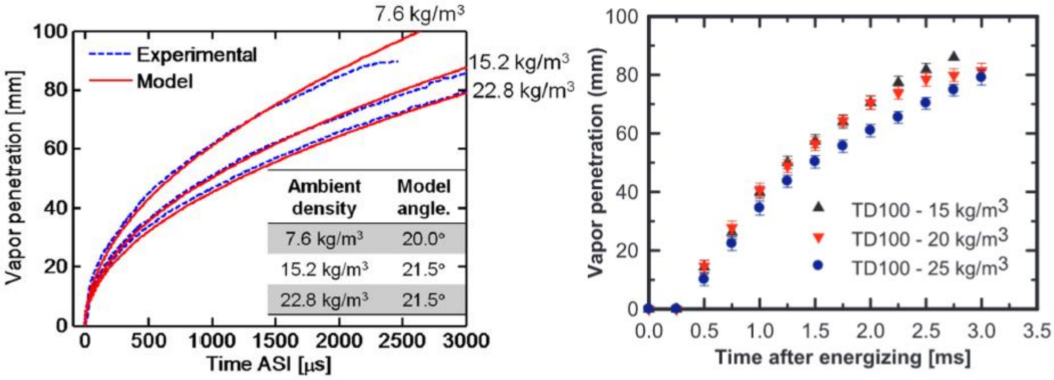

Figure 27: Time-resolved jet penetration at three different ambient temperature and density conditions. Left: (900K & 22.8kg/m^3, 1100K & 15.2kg/m^3, 1400K & 7.6kg/m^3) from Pickett et al *in [40]. Right: ambient temperature is constant at 724K from Hawi* et al *in [36]. Both experiments have the same injection pressure of 150MPa and conducted in a CV – vessel.*

Both sprays are injected with an injection pressure of 150MPa. Hawi *et al* [36] attributes the increase in temporal jet penetration at decreasing ambient densities to a combination of reduction aerodynamic resistance and lengthening spray penetrations. In both cases the increase in density has a non-linear effect at given time, however the in this sense the experimental data appear to contradict each other. This may be a due to differences in the used fuels (left: n-dodecane, right: tetradecane).

The sensitivity of axial and radial mass fraction distributions at given locations and times with changing density and temperature conditions is shown in Figure 28 (from Pickett *et al* [40]). The axial mass fraction distribution is shown as a function of axial distance to the nozzle in the top row. The radial mass fraction distribution, in the bottom row, is plotted as mixture fraction over the plume cross section. The columns each represent an individual condition with the density reducing from left to right column. The greyed area represents the 95% confidence band of the experimental error. The authors highlight that due to fuel decomposition at the highest temperature/lowest density condition, the experimental method struggled to resolve the mass fraction distributions deeming them unreliable for quantitative comparison.

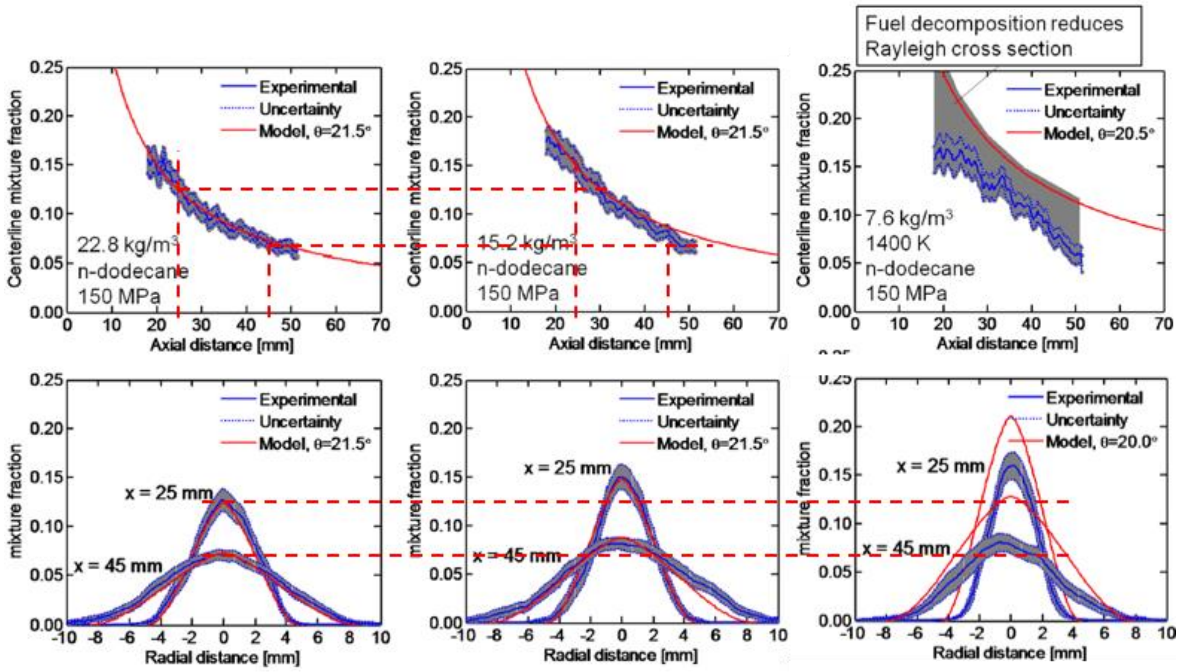

Figure 28: Fuel mass fraction distributions across the plume axis (top) and cross section (bottom) at given axial locations and time for three operating conditions. The left column: 900K & 22.8kg/m^3, the middle column: 1100K & 14.8kg/m^3, the right column: 1400K & 7.6k/m^3 (reproduced from [40])

The data in Figure 28 show that the mixture fraction decreases with increasing ambient density at the investigated locations from Pickett *et al* [40]. This is visualised by the peak of the radial mass fraction distributions of the lower densities exceeding the dashed reference. This means that less of the ambient gas is entrained into the plume leading to a richer spray plume with decreasing densities. The higher mixture fraction is also shown along the plume axis, where the decay curve is shifted to the right and up. The data shown for the 7.6kg/m3 density case can only be considered qualitatively because of experimental difficulties reported in [45].

3.1.3.3 Effect of combustion on jet penetration

The jet penetration is also dependent on whether the mixture will ignite or not. Initial experiments by Picket *et al* in [45] (shown in Figure 29) and later confirmed by Pastor *et al*

[46] show two things. Until ~ 400ms, the spray penetration of the inert and reacting case are almost undistinguishable. The experimental data show a slight dip in jet penetration at this point. The authors attribute this to the darkening environment during the cool flame.

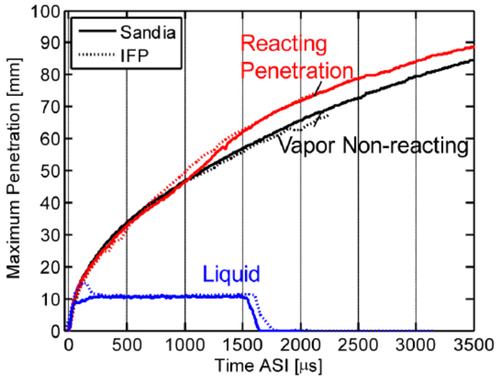

Figure 29: Difference between jet penetration under inert and reacting conditions [45]

The effect on the overall penetration however is negligible. Following ignition, the curve of the reactive case shows a slightly steeper curve albeit being very similar to the inert case. Finally, between ~800ms and ~1500ms, the curves clearly diverge before continuing relatively parallel. The analysis given in Pastor *et al* [46] identifies the drop in local density and increase in spray cone angle as the driving phenomena for briefly accelerating the spray plume.

3.1.4 Ignition delay and heat release

In a typical non-premixed diffusion flame, the ignition of the fuel air mixture occurs in two stages. The time that elapses between Start-of-Injection (SoI) and the first stage is called the Start of Cool Flames (SoCF). The SoCF is defined as the first tracking of the onset of chemical reactions. This can be identified by a negative temperature gradient (thermal preparation). During this time, reactions with formaldehyde are consumed and hydrogen peroxide decomposes to produce OH radicals. When these radicals react, they do so exothermally, initiating the so-called Second Stage Ignition (SSI). The time between SoI and the start of SSI, which is also the start of heat release, is conventionally known as the Ignition Delay (ID). The ID time depends on the local thermodynamic conditions as well as injection pressures and turbulence levels [51].

1. Increasing ambient temperatures reduce ignition delay [47, 51]
2. Rising injection pressures reduce ignition delay [51]
3. Increasing ambient densities reduce ignition delay [47, 51]

3.1.4.1 *Effect of ambient temperatures and injection pressure on ignition delay*

The effect a swing in ambient temperature and injection pressure have on SoCF and SSI is shown in Figure 30. In Benajes *et al* [51] and Pickett *et al* [47] the decrease in ignition delay with increasing temperatures is explained with an accelerated oxidation. Figure 30 also shows that regardless of ambient temperature, increased injection pressures reduce ignition delay time. Rising injection pressures result in accelerated plume mixing [52] which produces a combustible mix earlier.

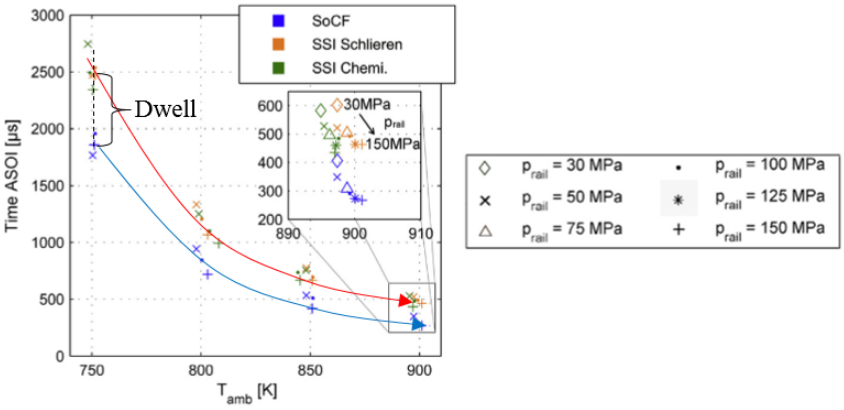

Figure 30: The effect of ambient temperatures and injection pressures on SoCF and SSI (reproduced from [51])

Another observation is the temperature effect on the SoCF-SSI time dwell. Reducing ambient temperatures has a similar effect on both, but with a minor reduction of dwell time towards increasing temperatures. This means the start of cool combustion also strongly influenced by ambient temperatures and injection pressures.

3.1.4.2 *Effect of ambient density on ignition delay*

The effect of an ambient density sweep on SoCF and SSI is shown in Figure 31. A clear non-linear decrease of ID can be observed with increasing densities. Benajes *et al* [51] explain this with the increasing spreading angle of the spray. This increases the volume of entrained air causing accelerated heating of the fuel/air mixture.

In contrast to the effect of ambient temperature and injection pressure, ambient density has a strong effect on the SoCF-SSI dwell time. It appears that the SoCF is significantly less sensitive to a density swing as the SSI.

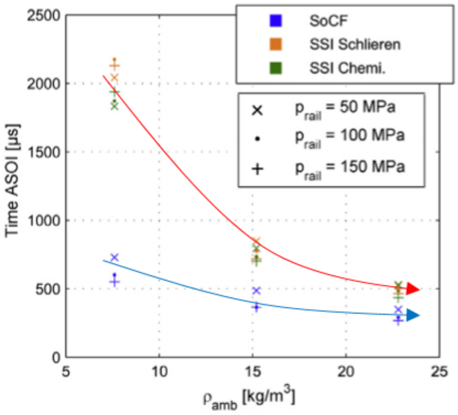

Figure 31: The effect of ambient density and injection pressures measured SoCF and SSI [51]

3.1.5 Flame lift-off-length

Various definitions of LoL exist. For example, the gas-jet theory by Peters in ([53]) describes the LoL as the distance from the tip where there is equivalence between the velocity of the fuel jet and the flame front velocity. Another definition given by Pickett *et al* in [47] links the LoL to the Arrhenius-type law. There the flame lift-off is defined by the distance travelled before the high temperature reactions start. In this thesis, the latter definition by Pickett *et al* in [47] will be used.

According to studies by various researchers [47, 49, 51], the main factors that determine the LoL are the ambient temperature, density and the injection pressure. The LoL is determined by the amount of ambient air entrained into the spray and therefore dependent on turbulent mixing described above in section 3.1.1.3.

1. An increase in ambient temperature reduces the flame lift-off (see Figure 32).
2. The LoL increases with decreasing gas densities (see Figure 32)
3. An increase of orifice diameter increases the LoL (see Figure 32).
4. An increase of injection pressure linearly increases LoL (see Figure 33).

3.1.5.1 Flame lift-off dependency on ambient temperature

The effect the ambient temperature has on the LoL is described in Siebers and Higgins [49] and shown in Figure 32. At this point, the effect of ambient density and orifice diameter will be ignored, as they will be separately discussed in sections 3.1.5.2 and 3.1.5.3. Figure 32 shows a clear non-linear decrease in LoL with increasing ambient temperature. The reasons for this are straightforward. The hotter air accelerates chemical conversion rates, which advances the spatial SoC towards the nozzle.

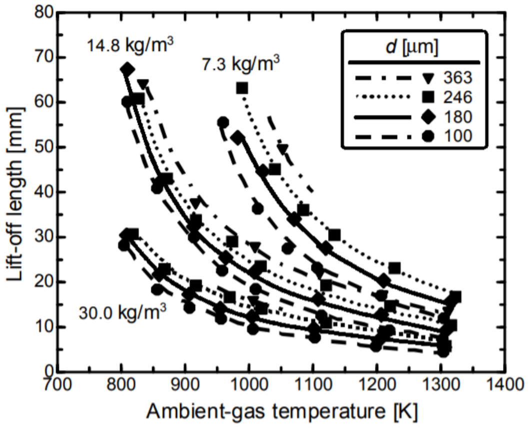

Figure 32: LoL over ambient gas temperature for a range of gas densities and four orifice diameters [49].

3.1.5.2 Flame lift-off dependency on ambient density

To clarify the effect the ambient gas density has on the LoL, the temperature and orifice diameter contributions in Figure 32 are ignored. The graph shows a strong non-linear dependency of LoL to gas densities at constant temperatures and orifice sizes.

The reason for this strong dependency is not clear. Peters' scaling law for gas jets here fails to approximate the appropriate trend. Siebers and Higgins in [49] point to two potential reasons for this: (1), the non-isothermal vaporisation of the up-stream fuel and (b), the effect of the differing densities of fuel and air have on turbulent transport an mixing of the spray.

3.1.5.3 Flame lift-off dependency on orifice diameter

The effect the orifice diameter is shown at various ambient pressures and temperatures in Figure 32. Increasing the orifice diameter results in increasing lift-off lengths. Siebers and Higgins [49] report that on a percentage base, the effect on quantitative LoL is relatively uniform across all investigated temperature and density conditions. Relative to the effect of a change in gas density or temperature, the impact is minor. The effect of orifice diameter is the second influential parameter the scaling law by Peters fails to address adequately. Some potential reasons for this uncertainty are given in section 3.1.5.2.

3.1.5.4 Flame lift-off dependency on injection pressure

Figure 33 shows the sensitivity of LoL against the injection pressure for multiple orifice diameters from Siebers and Higgins in [49]. Additionally, two discrete density and temperature conditions are plotted. The chamber pressure is held constant and the injection pressure is varied, which is the reason why the x-axis is shown as the pressure drop between the two. Figure 34 shows the same data as Figure 33 but plotted over the injection velocity. The injection velocity is calculated from Bernoulli's equation and multiplied by the orifice velocity coefficient [49].

The data show a minor non-linear increase in LoL with increasing injection pressure. The datasets with identical ambient conditions show a relatively evenly spaced increase in lift-off with increasing orifice diameters. In contrast, the condition with reduced temperature shows a strong increase in LoL with increasing pressure drop. The opposite is the case for a discrete reduction of ambient density. The fact that the x-axis of Figure 33 can be simply replaced by the velocity shows the dominance of the injection velocity over this process.

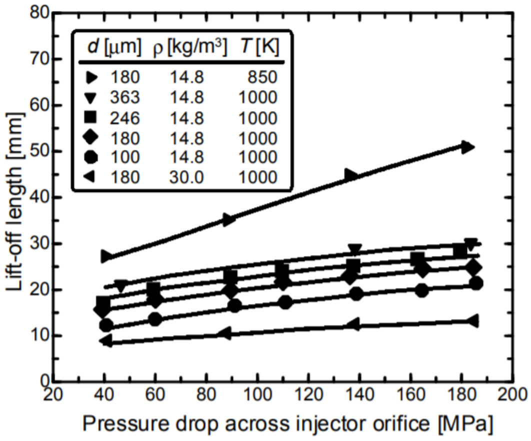

Figure 33: LoL over pressure drop across the injector orifice [49]

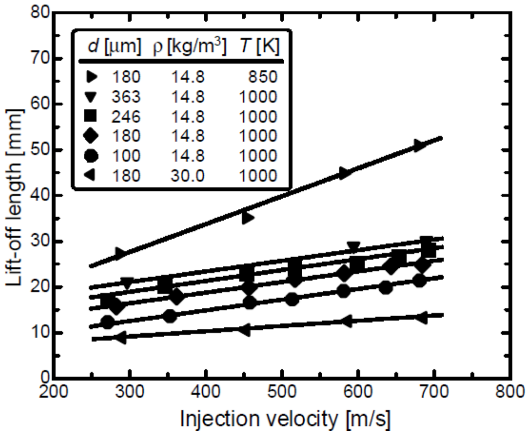

Figure 34: LoL over injection velocity [49]

The dependency of the LoL to injection velocity can be related to the Peters' scaling law [53]. There it is stated that the LoL is linearly dependant on an increase of injection velocity because of the proportional relationship of the turbulent mixing rate to injection velocity at given location. This turbulent mixing rate decreases with axial distance. The result of increasing injection velocities is a flame stabilisation retreating downstream to a location where local mixing rates and reaction rates are balanced. An increase in injection pressure has no effect on local reaction rate, which is determined by the laminar flame speed and thermal diffusivity.

3.2 Numerical approaches

There exists a plethora of numerical approaches to simulate a range of engineering problems. Due to the many different approaches for various areas of engineering, this review will be limited to the liquid injection of spray into a gaseous environment, also called multiphase flow, into a combustion chamber. Even within this narrower scope, the text will at various points set boundaries to limit the content to the most relevant approaches.

The following sections are structured as follows: (1) the main contributors to the body literature concerning simulations of the ECN Spray A configuration are listed. This is done to highlight the international attention Spray A has garnered. Following this, the main simulation approaches used in multiphase flow are introduced. The focus hereby will lie on models that are relevant to this thesis, although some alternative models are still mentioned.

3.2.1 Research groups working with the ECN data

Numerical contributions to resolve the experimental data delivered by participants of the ECN are widespread. Some groups however stand out with continuous attempts to improve understanding of simulation approaches and developing hypotheses for processes for which no experiment can currently deliver proof. These contributors are predominantly from the following groups in no particular order:

- Sandia National Laboratories (SNL, USA)
- Institut Français du Pétrole Energies Nouvelles (IFPEN, France)
- Argonne National Laboratories (ANL, USA)
- Politecnico di Milano (PM, Italy)
- University of Perugia (UoP, Italy)
- Universitario De Motores Térmicos, Valencia (CMT, Spain)
- ETH Zurich, (ETH, Switzerland)
- University of Wisconsin, (UW, USA)
- University of New South Wales (UNSW, Australia)

Far more groups, including the University of Brighton, have occasionally contributed in a more limited capacity. The list above highlights the international collaboration and the extent to which the Spray A was discussed, validated and used for both fundamental and more practical research. Most of the following discussions of numerical approaches will be based on contributions of the above.

3.2.2 Multiphase flow treatment

Liquid fuel injection into a combustion chamber can be expressed numerically as a dilute cloud of droplets in dispersed gas phase. The most common numerical implementations are the Eulerian-Eulerian and Eulerian-Lagrangian methods. However, the work shown in this thesis is done on Ricardo VECTIS, a commercial software that is based on an Eulerian-Lagrangian framework. For this reason, only a short description of the Eulerian-Eulerian framework will be given.

3.2.2.1 Eulerian-Eulerian approach

In the Eulerian-Eulerian approach, the two-phase flow of liquid and gas are considered a continuum. Some promising results when applied to ECN Spray A and other conditions were shown with this type of implementation by various authors [6, 9, 54-56].

3.2.2.2 Eulerian-Lagrangian approach

The Eulerian-Lagrangian framework is a numerical implementation for multiphase flows in which the Eulerian statistical representation of the gas phase is coupled with the Lagrangian particle framework for the liquid phase [57]. In the Lagrangian Particle Tracking (LPT) method, either each droplet can be tracked individually or collected into a statistical bundle of parcels with common physical attributes [58]. The interaction between the two phases can be done via one-way coupling, where the liquid flow does not affect the gaseous flow, or two-way coupling, where both phases affect each other. The transfer of mass, momentum and energy from the liquid phase is then accounted for in the transport equations of the gas phase. The models for the Eulerian and Lagrangian phases will be discussed in the sections 3.2.3 and 3.2.4 respectively.

3.2.3 Turbulence modelling

One of the defining factors for runtime and physical accuracy is the selected method of turbulence modelling. The three main approaches to compute turbulent motion of the Eulerian phase are in decreasing order of physical accuracy and runtime. Direct Numerical Simulation (DNS), Large Eddy Simulation (LES) and Reynolds-Averaged Navier-Stokes (RANS). The turbulence modelling in this thesis is based on the RANS approach. Nonetheless, for the sake of context a summary of the other approaches is provided.

3.2.3.1 Direct numerical simulation

In the DNS approach, the Navier-Stokes equations are solved numerically making any turbulence sub model obsolete. Thus, all present spatial scales, from the dissipative Kolmogorov scales to the integral scale, must be resolved in the computational mesh. The high level of physical accuracy is achieved at a high runtime penalty. DNS simulations are typically confined to simplified cases for fundamental research. Simulations of a multiphase spray injection under Diesel relevant conditions are scarce. The few instances where it was applied to somewhat practical cases comparable to the ones shown here, the scope of the investigation was highly limited [59-61]. The exact details of computational runtime are not given but the high run times are regularly mentioned and could range from days to weeks on a super-computer. A commercial application of DNS in commercial engine design is therefore out of question. A separate discussion of the runtime will follow in section 3.2.6.

3.2.3.2 Large eddy simulation

LES is a technique in which the large scales of the flow are solved explicitly, and the small scales accounted for implicitly by SGS models. This simplification greatly reduces the computational expense at the cost of some physical accuracy. This increased computational efficiency at still relatively good physical accuracy is the reason why LES has been receiving increased interest from academic bodies for the last two decades, and more recently from industry. While commercial interest is still limited to areas of engineering that rely on fundamental research (like gas turbine development), wider adoption is likely to occur within the next decade. However, for engine application, which has a large difference between the scales of the nozzle hole and those of the cylinder bore make well-resolved LES very computationally expensive [62].

There are many studies using a combination of LES treatment of turbulence with LPT for droplets of which some are conducted for the Spray A condition. Examples of these are given in [63-70] and a good review is presented in Kahila *et al* [39] and Kaario *et al* [71]. Some notable examples of LES combined with various combustion approaches (Turbulence Chemistry Interactions (TCI) models) are the Transport Density Distribution Function (TPDF) by Pei *et al* [72-74], Conditional Moment Closure (CMC) by Blomberg *et al* [75] and finite rate chemistry by Pei *et al* [68]. These three approaches suffer from relatively high computational run times. An alternative and more computationally efficient approach to these is based on flamelet models (e.g. [76-79]). A high-level overview over these combustion models will be given in section 3.2.5. Overall, the results presented in the mentioned LES approaches show good performance to replicate trends well while often struggling to match absolute values.

The downside of LES is that it still requires coefficient tuning, shows strong grid sensitivity while still requiring extensive computational resources. The main drawback for engine development is that if the models are tuning dependant and tuning iterations are very time consuming, the advantage over fast test bed results is lost. For this reason, LES is well represented in more fundamental research and radical combustion system development where it can use its good physical accuracy to shed light on unobserved, microscopic processes. For commercial engine design, where the focus lies more on macroscopic aspects, which are relatively well understood, the computational overhead in comparison to the potential benefit still prohibits industry-wide rollout. With continuous technological advancements, the computational overhead is set to drop in the future, making LES more accessible. However, until then, the RANS framework, which is discussed in the next section, will remain engine developers' approach of choice.

3.2.3.3 Reynolds-Averaged Navier-Stokes

In RANS approaches, the task of the turbulence model is to calculate the Reynolds stresses and turbulent scalar fluxes. RANS turbulence modelling is a very wide field. To narrow down the scope, only point 1ci), the k-ε models, will be considered because they make up most numerical Diesel spray studies in the RANS framework.

1. Linear eddy viscosity models
    a. Algebraic models
    b. One-equation models
    c. Two-equation models
        i. k-ε models
            - Standard k-ε model
            - k- ε models RNG model inert: reactive:
            - Realisable k-ε models
        ii. k-ω models
2. Non-linear eddy viscosity models
3. Reynolds stress model (RSM)

Two-equation models include two transport equations to represent the turbulent flow properties. The two transport equations determine the turbulent kinetic energy k and either the turbulent dissipation ε or the specific turbulence dissipation rate ω [80]. Both approaches are based on Boussinesq eddy viscosity assumption. This is where the strength and weakness of two-equation models lies. The Boussinesq assumption greatly simplifies the problem by introducing tuning coefficients to account for physical processes. This reduces runtime, however at the penalty of physical accuracy. The main disadvantage is however is the fact that the Boussinesq assumption is not valid for flows with steep velocity and pressure gradients because the Reynolds stress tensor is not necessarily proportional to the strain rate tensor. For this reason, two-equation models regularly have problems in simulating conditions with strong velocity and pressure gradients [80-82]. Despite this fundamental flaw, two-equation models remain the standard approach for engineering problems. This is due to their low runtimes and the possibility to work around the mathematical deficiency using modelling coefficients. Despite the rise of LES, RANS studies with two-equation models are still well represented in research. Successful simulations using k-ε models are shown for Spray A in [4, 8, 73] and for engines in [5, 83, 84].

3.2.4 Spray modelling

Using the macroscopic characteristics of the spray like liquid & jet penetration and spreading angle are the most common metrics in assessing the quality of a simulation in relation to experimental data [40-42, 85-87]. This is mostly due to the relative simplicity and technical maturity of the optical imaging techniques to deliver the required validation data. As described in section 3.2.2, the liquid phase is typically modelled with the LPT method. Within this method, there exist a range of models to handle the droplet break-up, evaporation, coalescence and collision. The following list shows just a few of the available sub models and is by far not exhaustive.

1. Initial droplet sizes
    a. Initial Droplet Size Correlations
        i. Taylor, El-Kotb, Hiroyasu-Arai-Tabati & Patterson-Reitz correlation
    b. Initial Droplet Size Distribution
        i. Rosin-Rammler
        ii. Tabulated distribution
2. Droplet drag and distortion
    a. Putnam model
    b. Liu-Mather-Reitz model
3. Droplet heat and mass transfer (evaporation)
    a. Frossling model
    b. Spalding model
4. Droplet break-up
    a. Primary break-up

        i. Huh-Gosman
    b. Secondary break-up
        i. Reitz-Diwakar, Liu-Mather-Reitz, Patterson-Reitz, Rayleigh-Taylor Model
    c. Hybrid
        i. KH-RT, KH-TAB, KH-Pilch
5. Droplet coalescence and collisions
    a. O’Rourke model

The following sub sections will discuss the main aspects of each of the above points. More detail will be given only where necessary.

3.2.4.1 Initial droplet sizes

When introducing the droplets into the domain without considering the nozzle flow, droplet sizes are a necessary input. This can be done either as a correlation or as a user input.

3.2.4.1.1 Initial droplet sizes correlations

Initial droplet size correlations are based on empirical correlations for initial droplet SMDs present at given spray conditions. Since these models are empirically derived, they do not necessarily require break-up models. A thorough literature search did not highlight any publications using any of these models for relevant cases. A reason for this may be that the empirical data these models rely on is outdated. Further, older droplet measurements were acquired in the optically thin region of the spray meaning that the measured droplet sizes were not necessarily representative of the centre of the near nozzle region.

3.2.4.1.2 Initial droplet size distribution

There are two common approaches for user-defined droplet sizes. The first is the Rosin-Rammler distribution [88], in which a mean droplet size is given and a spread parameter is used to define the distribution. While not very common, the Rosin-Rammler distribution has been used in relevant studies like D’Errico *et al* [10]. The other distribution method is in form of a tabulated probability distribution. This option is wide spread, most commonly featured in relevant publications (e.g. [63, 72]) and the one chosen for this thesis.

3.2.4.2 Droplet drag and distortion

As the droplets move through the carrier fluid, they experience aerodynamic resistance. The momentum conservation is described by Newton's second law. The equation, which is discussed in detail in section 5.1.4, contains a drag coefficient that must be computed. Two implementations are highlighted here. The first is the Dynamic model, which is commonly used, and the second is the Putnam model. The former is the most common approach which is prevalent in Converge and Star CD. The droplet is postulated to oscillate and so change its drag coefficient in the process. A detailed description can be found in the original documentation by Liu *et al* in [89] and examples of work done with this model is given in [84, 90]. The Putnam model is rarely used but was the model of choice in this work after model trials showed a technical issue with the Dynamic model. Other models like the Mach number law [91] or Schiller-Naumann [92] exist, but are not further elaborated here as they are not as commonly used and available in the used CFD tool.

3.2.4.3 Droplet mass and heat transfer (evaporation)

Evaporation plays a big role in droplet evolution in the hot environment of a combustion chamber. To simulate this, the sub-models calculate the simultaneous heat and mass transfer. The droplet heating is calculated via convection and conduction while returning the evaporation via convection and diffusion. The two most common correlations for this are the Frossling [93] and Spalding [94, 95] correlations. Both models are frequently used and literature favours neither of them. To my knowledge, there are no recent relevant publications that actively investigate the role of the evaporation model on Spray A or relevant engine cases. They are typically only mentioned as a side note.

The Spalding correlation is the default evaporation model for VECTIS with no available alternative. This model does not include any modelling coefficients hence does not play a significant role in this thesis.

3.2.4.4 Droplet break-up

Although a plethora of spray break-up models exists, the ones that are most dominant in literature are the hybrid break-up models. For this reason, there will be no further description of the other primary or secondary models. Out of the hybrid models, the Kelvin-Helmholtz Rayleigh-Taylor (KHRT) model is leading. It is so widely spread that it may be considered the current standard break-up model. Examples of applications can be found in [4, 8, 75, 96] for Spray A, or in [5, 83] for engines. This model is also the model of choice for this thesis, as it is a well-documented and validated model used widely to simulate direct injected spray conditions.

Despite it being a very popular sub model, it does suffer from drawbacks. It employs four modelling coefficients to steer the break-up time scales and the size of child droplets being shed from the parent. The single most influential coefficient is the KH-B_1 coefficient. It linearly scales the calculated rate at which the parent droplet shrinks which controls the effective evaporation rate and therefore overall spray penetration. With this tempting dial, researchers can adjust the simulated spray penetrations to experimental data. Indeed, this done in almost every study presented earlier in this section that uses this sub model for calculating spray break-up.

The key issue here is that by tuning this dial without caution, it is possible to break-up the droplets without proper account for the real heat transfer. In other words, by artificially accelerating or decelerating the droplet shrinking, too much or too little heat is drained from the ambient gas while still achieving a perfect match to experimental data. This can lead to miscalculation of ignition delay and flame lift-off, which is then often recovered by tuning coefficients in the combustion model.

3.2.4.5 Droplet coalescence and collision

Information on the used droplet coalescence models are rarely listed in publications containing spray simulations, but where it is known, it is usually the O’Rourke model. The model considers three outcomes of droplet-droplet interaction. The first is grazing collision where the droplets collide and bounce of each other. The second is a mixed collision and coalescence outcome where two same sized droplets produce a larger coalesced and smaller detached droplet. The last mode is the total coalescence of two droplets into one.

3.2.5 Combustion modelling

Various groups have employed different approaches for simulating diffusion flames. The approaches under the RANS umbrella are coupled with transported probability density function (TPDF) [62, 63, 72, 73, 96] or flamelet-type models [4, 8, 97]. In the following two sub sections, a brief discussion on the approaches and results of representative publications with these combustion-modelling approaches will be given.

3.2.5.1 Transported probability density function

Pei *et al* give an example of TPDF in [62, 72-74]. In his work, TPDF is based on using a Lagranian Monte Carlo approach to solve the transport equation. It uses a mixing model to track notional particles carrying the composition and enthalpy and calculate their chemical reaction. The unclosed turbulent flux term is treated with the assumption of gradient diffusion. The molcular mixing terms are closed using three different mixing models called exchange with the mean (IEM) [98], modified Curl (MC) [99] and Euclidean minimum spanning trees (EMST) [100]. The combustion process is approximated with first detailed, and later reduced chemical mechanisms.

The results delivered in this series are among the best for the a variety of Spray A conditions. Mixture fractions, spray and jet penetrations, combustion characteristcs are all matched well. However, despite the rigour shown in this work, some critical assumptions were made. The droplet sizes are assumed to be that of the nozzle diameter and kept constant throughout parametric swings, droplet coalescence and aerodynamic break-up are ignored (evaporation is the sole diameter reducing mechanism) to match the spray penetration. These kind of simplifcations are common even among high quality studies but highlight a fundamental flaw. Droplet sizes are not constant and droplet break-up due to aerodynamics is crucial (see section 3.1.1). The complex models that deal with mixing and combustion therefore stand on a physicaly questionable basis of spray evolution assumptions. Indeed, to match the experimental data, a mixing coefficient is introduced and tuned.

3.2.5.2 Flamelet-type models

In a flamelet-type approach, multiple laminar flamelet regions round the stoichiometric surfaces of the mixing zone are used to approximate the turbulent flame. Typically, experimental data of the laminar flame speed are used to determine the relationships between the variables of the mass fractions and temperatures. With knowledge of these relations, the transport equations for species mass fraction are solved.

Examples of flamelet-type modelling approaches used in the Spray A configuration are given in [4, 8]. The work done in both publications deals with multiple parametric variations of Spray A and analyses the performance of the combustion model against changing boundary conditions. As described in section 3.2.5.1, a sophisticated combustion model combined with well-validated chemical kinetics mechanisms is combined with a relatively simple spray injection and break-up modelling approaches. They use the KH-RT break-up model with constant modelling coefficients for all parametric variations of the operating condition. They then use the modelling coefficients in the combustion model to approximate combustion characteristics. In both publications, the trends are reproduced relatively well while the absolute values are at times well beyond the experimental error margin.

3.2.6 Computational effort

As briefly mentioned in the introduction to this thesis, commercial engine development, with its results-focused approach to R&D, will always select the most cost-effective means for developing products. For engineering areas where costs for prototyping and testing are usually lower than investments in more sophisticated computational infrastructure (e.g. ICE development), the emphasis on early-stage numerical simulations is smaller than in areas where the opposite is the case (e.g. gas turbine development). A notable exception are large marine engines, where the high cost of LES simulations is still preferable to even higher prototyping costs.

A single engine DoE campaign can deliver the performance metrics for the full engine map within a couple of hours. Since at least one iteration of prototyping is necessary for validation, the cost-efficiency of numerical simulations stand against that of engine conversion and test preparation times. Currently, the latter is still considered to be worth the effort and cost due to poor predictive capabilities of numerical approaches. Rather counter-intuitively, the solution may not be to employ improved numerical models because their runtimes and computational cost are limited by the duration and cost of the prototyping and testing process. An alternative, which is the path followed in this thesis, is the management of the limitations of simple models by improving the setup quality

To understand the selection of the simulation approach in this thesis, a brief runtime comparison between some publications is offered. A direct comparison of runtime is only rarely possible due to the different implementation, the selected sub models and the used hardware. The main numerical influences of the runtime that will be highlighted here are the turbulence model and the TCI model. This is best done in the context of the Spray A configuration because it has been widely used by different groups, allowing a relatively straight forward comparison.

3.2.6.1 Turbulence model influence on runtime

Full-scale analysis using DNS on Spray A currently do not exist. One of the reasons for this is that the turbulence Reynolds number for Spray A are between 10 000 and 20 000 [72]. Recent efforts using DNS on a hydrogen-air combustion case with the Reynolds number approaching 1000 required 40 million CPU hours [101, 102]. Even with the potential of buying access to exascale computing, it is easy to see why DNS will not be an option for regular engineering problems for at least a few decades.

The recent advancement of computational power has brought about the rise of LES approaches in academia and in some areas of more radical commercial R&D projects. It is conceivable that LES-based models could become cost-effective even for regular engineering problems within the next decade. In the area of gas turbines, aeronautics and large marine diesel applications, where prototype development and testing are very expensive, LES is already seen as the most cost-effective development tool and has established itself as the industry standard.

In combustion engine development, well-resolved LES that includes all scales from near-nozzle region to the combustion chamber are still significantly more expensive than RANS approaches. A direct comparison between the two under the Spray A condition by Som *et al* in [103] reported a runtime for 2ms injection duration of 18hrs (RANS) and 150hrs (LES) for reactive cases and 2hrs (RANS) and 20hrs (LES) for non-reactive cases on identical hardware. Runtimes of an order of magnitude higher could only be acceptable if the results and predictive capability of LES were superior. LES is certainly superior when it comes to resolving detailed flow structures; however, trends of spray, combustion and emission characteristics are still subject to tuning of modelling coefficients and are often not considerably much better.

3.2.6.2 Turbulence chemistry interaction influence on runtime

Besides the used turbulence model, the selection of the TCI model influences the runtime. Detailed chemical models are often simplified to reduced chemical mechanisms to reduce cost [63, 84]. The selection of reduced chemical mechanism also has a strong effect on the potential runtime. In Bolla *et al* [84] a normalised comparison between the Pitsch, ERCv2 and Hewson mechanisms for *n*-Heptane. It is shown that ERCv2 is 10x, and the Hewson mechanism 80x more expensive than the Pitch mechanism. To further bring down computational cost, instead of modelling the chemical interactions, tabulated chemistry may be used (for example in [104, 105]). Here, the resulting thermodynamic conditions and species transformation are extracted from tables based on spatial mixture fraction and scalar dissipation rate.

3.3 Tabulation as means to reduce computational time

Tabulation in the area of numerical simulations is a method to reduce runtime by replacing complex physical calculations by the empirically derived outcome. This can significantly accelerate runtimes at little cost of physical accuracy depending on the number of data points in the table. In in-cylinder simulations of combusting diffusion flames, tabulated chemistry is a prime example of reducing runtimes to levels where the cost-effectiveness can compete with that of prototyping and testing.

In traditional methods of tabulation used in turbulent combustion (for example in [104, 105]) reactive species concentrations are mapped as functions of mixing variables (mixture fraction and scalar dissipation) as well as combustion progress variables. The table then iteratively returns thermodynamic conditions, resulting species concentrations to the active calculation.

In this thesis, a novel approach to a tabulation of modelling coefficients is taken. The link between coefficients of the sub-models that control the turbulent combustion dynamics to the operating conditions (injection pressure, ambient temperature, density and pressure) has not previously been investigated. One important point is that is the source of much difficulties is that although, for example, in traditional tabulation of turbulent combustion there is a solid physical explanation why species concentration is dependent on mixture fraction and scalar dissipation for diffused flames, this physical link might not be so obvious when the tabulation is made for spray, jet and combustion modelling coefficients.

4 Experimental data

A major limitation of the predictive character of virtual tools for combusting liquid jets comes from the difficulty in acquiring experimental data for validation based on real scale experiments. Most of the currently available quantitative data, which can provide information up to the individual droplet scale, are based on simplified experiments. Highly resolved experimental data sets are typically obtained under steady state conditions in Constant Volume (CV) geometries or at reduced ambient pressures modified piston engines with optical accesses through the cylinder liner or the piston. The overarching difference between quiescent combustion vessels and production engines is that in the latter, piston motion at (near) constant gas mass results in varying thermodynamic conditions at every crank angle position. A single injection event on a real engine therefore may encompass multiple individual experiments in a CV – vessel as shown in Figure 35.

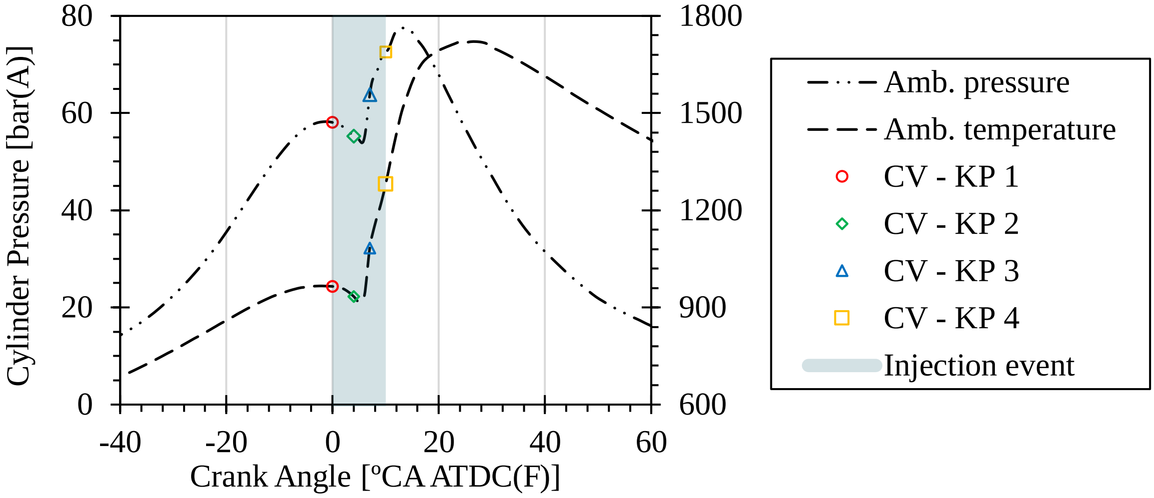

Figure 35: Schematic of how a real engine injection event is represented in multiple individual CV – experiments. These are hypothetical key points and have nothing to do with the DoE or Spray A key points.

In contrast to production engines, optical engines are operated at reduced BMEP's to avoid damage to the optical equipment leaving a persistent gap in representative experimental data for elevated load conditions.

This chapter will comprehensively discuss the experimental configurations of the ECN quiescent CV – chamber (from here on referred to as "CV chamber") in section 4.1, followed by a description of the ECN's light duty small-bore optical engine (from here referred to as "optical engine") and a production engine in section 4.2. Each section will contain sub sections describing the hardware configuration, the Fuel Injection Equipment (FIE), the operating conditions and the experimental data acquisition. The experimental data from the

ECN, especially the Spray A configuration, will receive more attention, since the bulk of the simulation work was conducted on them. The production engine will be discussed less due to confidentiality constraints.

4.1 The ECN quiescent combustion vessel

Many experiments were conducted in CV-vessels, mostly led by researchers of the SNL and IFPEN and contributors of the ECN. The focus to date has been on turbulent spray flames under Diesel-like combustion conditions, while allowing a high degree of optical access for advanced experimental diagnostics and well-characterised initial and boundary conditions for simulations, including detailed fuel injector characterisation [45, 106, 107]. Their experiments showed the effects of operating conditions like ambient pressures, densities, temperatures and injection pressures or fuel injection equipment specifications like nozzle orifice diameter on spray [13, 35, 37, 38, 108, 109], jet [51, 110-113], combustion [47, 49-51, 90, 113-116] and emission [48, 117-121] characteristics. Some of these findings were discussed in detail in section 3.1.

Despite the amount effort the experimentalists have put into controlling the boundary conditions of the Spray A condition, variations are inevitable. Pickett *et al* highlights in [45] that the experiments at two institutions will vary due to minor differences in set up or measurement technique. Further, various versions of the nominally same injector are circulated. Detailed characterisation of the injectors revealed microscopic differences that are thought to influence comparability between institutions [45, 106, 107]. Additionally, the sustained use of the injectors leads to residual build up within the nozzle.

4.1.1 ECN Spray A configuration

A preburn-type combustion vessel (see Figure 36) produced the desired high-temperature, high-pressure ambient conditions with the desired species concentrations at SoI. A spark plug ignited a controlled quantity of a premixed combustible gas with a specified density. After complete combustion, the products cooled due to heat transfer to the walls. The drop of the measured chamber pressure beneath a threshold then triggered the fuel injection event (see Figure 37).

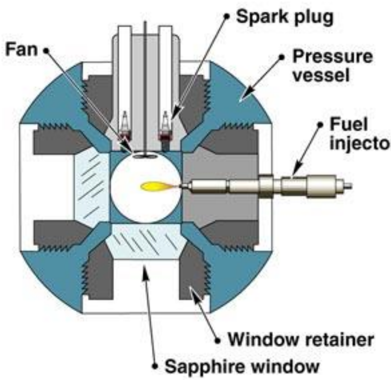

Figure 36: Schematic of the combustion vessel geometry [122]

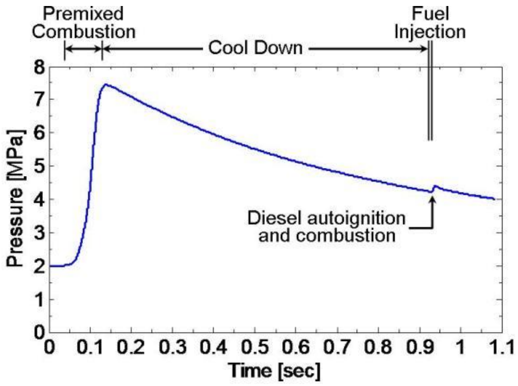

Figure 37: Schematic of the process to produce the ambient conditions at SoI [122]

4.1.2 ECN Spray A operating conditions

For this work, a subset of experiments commonly known as the ECN Spray A was selected (see Table 5). Beyond the nominal Spray A condition, there exists a plethora of parametric variations that were selected as basis for this study. Parametric variations include swings in ambient temperature and density (compensated by chamber pressure), injection pressures and gas compositions (inert & reactive).

Table 5: Selection of ECN Spray A parametric variations [123]

Key point	Amb. Temp (K)	Ambient Density (kg/m^3)	Chamber Pressure (bar)	Inj. Pressure (MPa)	Injector (#)	Gas composition at SoI (%)
1*/2*/3*	900	22.8	6.05	150/100/50	210677	$O_2 = 0$ $N_2 = 89.71$ $CO_2 = 6.52$ $H_2O = 3.77$
4*	1100	15.2	4.96	150		
5*	1400	7.6	3.19			
6/7*/8	750/800/850	22.8	4.9/5.3/5.6	150	210677 & 210370 (SNL)	$O_2 = 15$ $N_2 = 75.15$ $CO_2 = 6.22$ $H_2O = 3.62$
9*/10/11	900	22.8/ 15.2/ 7.6	5.9/3.9/2			
12/13/14	1000		6.6/4.4/2.2			
15/16/17	1100		7.3/4.8/2.4			
18*/19/20	1200		7.9/5.2/2.6			
21/22/23	750	22.8	5.1	50/100/150	210675 (CMT)	$O_2 = 15$ $N_2 = 85$
24/25/26	800		5.4			
27/28/29	850		5.75			
30/31/32	900	7.6	2.02			
33/34/35		15.2	4.03			
36/37/38		22.8	6.09	30/50/75		
39/40/41				100/125/150		

The data were obtained at different institutions, which means that depending on the available equipment and expertise, different metrics were measured. A comparable experimental setup was ensured by a strict guideline for the experiments. In occasions when methods or hardware differed from the ECN recommendations, extensive studies ensure to document the impact of these differences.

4.1.3 Fuel injection equipment characterisation

A detailed understanding of the FIE is crucial because it affects every aspect from spray injection, over combustion up to emission formation. Together with the ambient gas characteristics, knowledge of the FIE forms the first building block on which the rest of the experiment/simulation stands. Within the ECN community, there are multiple Spray A injectors in use simultaneously. They each have identical nominal specifications but differ ever so slightly on a microscopic scale. These differences were accounted for with rigorous experimental characterisation and comparisons. The different injectors are identifiable with the serial number reported with the corresponding experiment.

4.1.3.1 Injector specifications

In the ECN Spray A condition, a Diesel surrogate, n-dodecane, is injected vertically through a single-hole injector. Much effort was invested in characterising the specifications of the injector (see Table 6). The selected rail tube length of 240mm allowed flexibility of the experimental setup but also remain representative of lengths used in production engines. The large rail volume was necessary to minimize pressure drops during the supply of fuel.

Table 6: Spray A fuel injection system specifications [45, 124]

Fuel injection equipment	
Common rail fuel injector	Bosch solenoid-activated, generation 2.2
Nominal nozzle outlet diameter	90 µm
Nozzle K factor	1.5
Nozzle shaping	Hydro-eroded
Mini-sac volume	0.2 mm^3
Discharge coefficient	$C_d = 0.86$, using 10 MPa pressure drop
Spray full included angle	0˚ (single axial hole)
Common rail volume/length	22 cm3/23 cm *Use GM rail model 97303659
Distance from injector inlet to common rail	240mm
Fuel pressure measurement	70 mm from injector inlet / 240 mm from nozzle
Approx. injector driver current	18 A for 0.45 ms ramp, 12 A for steady state
Fuel specifications	
Fuel	n-dodecane
Fuel temperature at nozzle	363 K (90°C)

4.1.3.2 *Injection pressure*

High speed hydraulic measurements are conducted 240mm upstream the nozzle sac volume. The pressure transducer is either flush-mounted or mounted on the side after a T-fitting. After combining measurements of the spray momentum, where a force sensor was positioned ~3mm in front of the nozzle exit, and a separate cumulative mass measurement, the mass flow rate was calculated [45]. An ensemble average of 50 measured injection events for the Spray A baseline result is an RoI with a top-hat shape shown in Figure 38 [125]. The early spike of the RoI is possibly an effect of mass build up at the head of the spray.

4.1.3.3 *Rate of injection*

Experimental RoI measurements tend to be problematic for simulations, hence why filtered curves are necessary. For the other Spray A parametric variations with differing RoI's, a scaled version of the baseline is used as not all experiments come with individual RoI measurements. In the case of the ECN Spray A, a methodology to specifically produce the RoI's for their conditions was developed by CMT in [126] based on the theory of Payri *et al* in [127]. The used RoI's in the simulations, which differed between cases, will be provided in chapter 5.

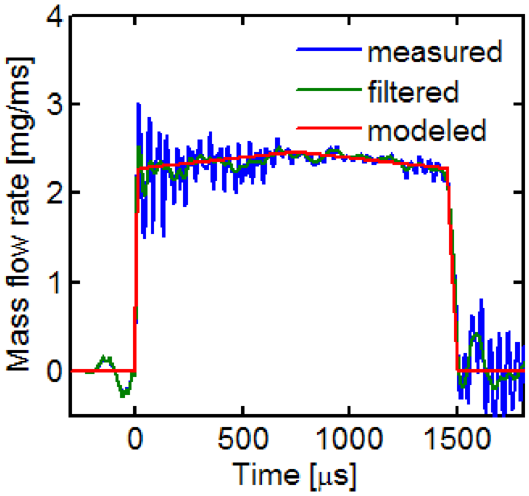

Figure 38: Measured (blue), filtered (green) and modelled (red) mass flow rate over time for Spray A using injector #210677 [125]

4.1.3.4 *Injector tip temperature*

In Pickett *et al* in [45] it is described how Teflon insulated cooling jackets around the injector and ceramic shields covering the injector tip are used to prevent heating of nozzle, sac volume and internal liquid prior to injection. Three different measurement methods to measure both internal sac volume and nozzle surface temperature are described in detail in Pickett *et al* [45]. The combination of these three methods concluded that the nozzle temperature must be regulated to 60˚C prior to premixed combustion to deliver the required 90˚C during the main injection event. Despite these efforts, controlling the fuel injection temperature remains challenging and is ultimately almost impossible to control during the injection event. This means that some level of uncertainty remains when analysing spray penetration data.

4.1.4 Combustion chamber boundary condition and spray characterisation

The fuel/air mixing process is crucial for engine combustion performance and emission formation [40]. There are a plethora of factors starting from within the FIE to the chamber conditions that have been shown to be influential for spray and jet penetration as well as spreading angle. Attempts of visualising and quantifying the processes within the sac volume and nozzle exist but are difficult due to the small scales, extreme thermodynamic conditions and limited optical imaging and are rarely conducted at representative operating conditions [128-130]. Hence, to get a better understanding of the mixing process, researchers have extensively observed the evolution of the near field liquid [28, 40, 41, 131-134] and vapour phase [23, 40, 115, 116, 135-139]. While these studies are extremely valuable, they hinge on a lack of understanding of in-nozzle processes which define the “initial state” of the liquid phase conditions at nozzle exit and are the prime contributor to plume-to-plume and shot-to-shot variations. Quantification attempts of these variations such as in Malbec *et al* [140] have improved the overall understanding of the causes. Nevertheless, to limit the scope of this thesis, geometrical nozzle effects and in-nozzle flow characteristics are neglected in favour of nominal parametric variations of thermodynamic boundary conditions.

4.1.4.1 Ambient gas temperature

For an accurate mapping of the gas temperature distribution of the gas five platinum (type-R) fine wire thermocouples were installed radially around the spray axis at approximately 40 mm downstream the nozzle as shown in Figure 39. The preburn and cooling phase are included in the measurement to later correct for radiation and heat transfer [45]. The average temperature distribution near the core and in front of the injector is spatially uniform and within 10K. The instantaneous variance is ±10 (± one standard deviation).

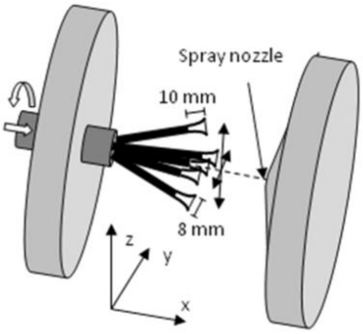

Figure 39: Schematic of the type-R thermocouple positioning in SNL's ECN CV – chamber [45]

4.1.4.2 Ambient gas pressure

The gas pressures of the combustion chamber were measured in the corners of the vessel using standard piezoelectric transducers that were calibrated against NIST-traceable sources at the operating temperature. Perforated ceramic sleeves shielded the transducers to prevent thermal drift. The accuracy of the transducers is stated at ±1% [45].

4.1.4.3 Ambient gas composition

The ambient gas composition before the premixed combustion was defined as such to accommodate the gas composition at SoI under the assumption of complete burn. The experimentalists have acknowledged the fact that complete burn is not achievable due to quenched reactions in cool crevice regions along the walls and sealing rings. Some measurements of unburned hydrocarbons confirmed their presence. Modelling efforts showed that the mole fraction of minor species decrease throughout the cooling phase and that for the baseline condition at 900K lie at under 0.02% of all combustion products at SoI [45].

4.1.4.4 Ambient gas velocity

The gas velocities (measured with particle tracking velocimetry) in the combustion vessel prior to fuel injection for Spray A are required to be under 1m/s. The liquid velocity at nozzle exit is expected to exceed 600m/s. The environment can therefore be considered near-quiescent because the gas phase velocities induced by the mixing fan are small in comparison to the liquid jet [45].

4.1.4.5 Optical Diagnostics

The liquid and vapour phase were optically resolved simultaneously using high-speed imaging. For quantitative measurements of the vapour phase, the Schlieren imaging technique was used. The liquid phase was measured using MIE-scattering. The schematic of the optical setup is shown in Figure 40 and described in detail in [134]. The detailed description of the experimental techniques of Schlieren and MIE-scattering can be found in [135, 141] and [40, 45] respectively. For both spray and jet penetration, the stated confidence level is given as 2σ.

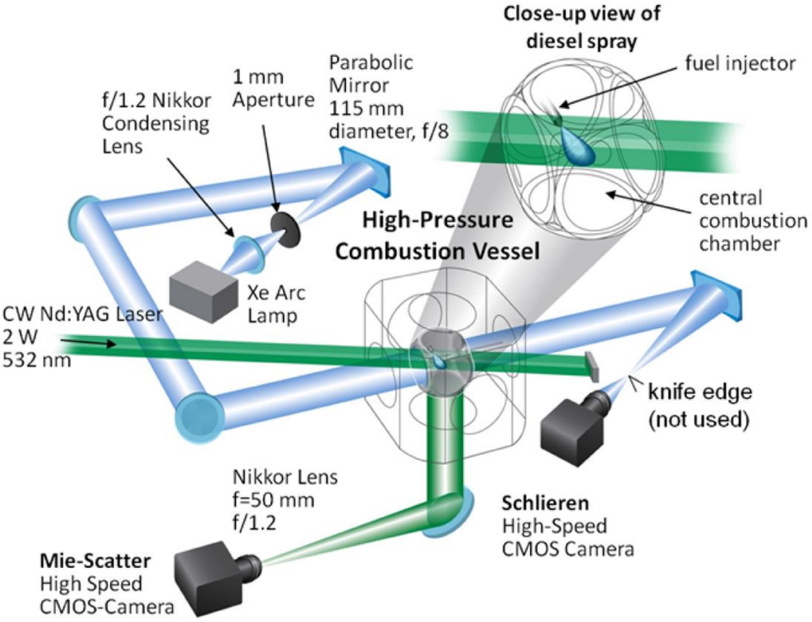

Figure 40: Schematic of the instantaneous imaging of liquid and vapour phase using MIE and Rayleigh scattering method [40, 45]

4.1.5 Limitations of the Spray A condition

In the Spray A experiments, where the investigative focus lies individually on mixture preparation, spray break-up, combustion and emission production processes, the complexity of hardware configurations and chemical compositions are significantly reduced. From a scientific standpoint, the detail of the findings for this condition are extremely valuable. For real engine development however, some crucial shortcomings must be highlighted:

1. Air motion in form of swirl, tumble and plume-to-plume interactions, which are present in a production engine, are fundamental factors
2. Production engines inject fuel through multi-hole injectors meaning the internal nozzle flow characteristics are inherently different to a single, vertical nozzle hole
3. The injection of standard pump Diesel instead of tightly controlled surrogates further introduces uncertainties into the combustion and emission formation process
4. In at full-load operation, the injection event happens under much higher ambient pressures and temperatures.

To understand the effects of these influential factors, the developed modelling coefficient table is validated on realistic engine conditions. The configuration of the hardware and the operating conditions are introduced in the following section.

4.2 The light duty small-bore engines

4.2.1 Engine configurations

For the validation of the modelling coefficient table, two geometrically similar engines with two differing operating conditions were selected. The first engine is an optical engine. The experimental data were gathered by the SNL and made accessible through the ECN platform [142]. It features a frequently used optically accessible General Motors 1.9L, single cylinder, light-duty engine (see [143-150]) which was adapted from a production engine. This optical engine was selected because it offers an extensive dataset with measurements of spray penetration and chamber pressure and images of combustion characteristics at part load conditions that resemble the ECN Spray A baseline at SoI.

The second engine is a production engine without optical access. The experimental data for a full-load condition is supplied by Ricardo Ltd. The chamber pressure, density and temperature conditions all exceed the initial confidence range of the developed coefficient table and therefore requires extrapolation to define the model setup. For this engine, time resolved measurements of global in-cylinder pressure and its derivative, the Rate of Heat Release (RoHR), are available. The configurations of both engines are listed in Table 7.

Table 7: The small-bore light-duty optical engine specifications

Engine specifications		
	Optical Engine [150]	Production Engine
Bore x stroke (mm)	82 x 90.4	Similar*
Unit displacement (L)	477.2	
Geometric compression ratio (-)	16.7:1	
Cycle (-)	4-stroke	4-stroke
Intake/Exhaust valves (-)	2/2	2/2

*Confidential

4.2.2 Engine operating conditions

To measure emissions and pressure rise of the optical engine, it was equipped with a metal piston. It was then operated in a constant speed, skip fire mode while still injecting fuel during every cycle. To simulate EGR and residual fuel fraction expected in a real engine fired continuously, the intake air was replaced with a mixture of nitrogen and CO_2 with the mass that would be present in a representative case. The compressor was used to hold a constant mass flow rate of intake gas, which at TDC would result in an ambient density of ~21.8kg/m^3. To obtain the optical measurements, the metal piston was then replaced by the fused-silica piston top and the intake mass flow of oxygen replaced by nitrogen to prevent combustion and window fouling. This setup was originally used in a larger study of injection strategies, however only one subset of this study, a condition without pilot injection, is used in this thesis [150]. This was done because split injection strategies remain outside the scope of this thesis. The production engine represents a full-load condition with an ambient density and temperature at SoI beyond Spray A range. It was run at standard continuously fired operation as part of a larger project surrounding piston geometries. A full list of the operating conditions is provided in Table 8.

Table 8: Optical and production engine operating conditions

Engine operating conditions		
	Optical Engine Part-load [150]	Production Engine Full-load
Engine speed (rpm)	1500	4000
Swirl ratio (Ricardo) (-)	2.2	Similar*
Wall temperatures (°C)	~90	~230
IMEP$_g$	9±0.1	-
BMEP	-	17.6
Valve timings		
Intake Valve Closure (IVC) (˚aTDC)	-152	
Exhaust Valve Opening (EVO) (˚aTDC)	132	
Intake Conditions at IVC		
Intake ambient mole fraction	19.7% O_2; 79.2% N_2; 1.1% CO_2	21% O_2; 78% N_2; 1% other
Intake gas flowrate (g/s)	8.51	143.2
Intake Pressure (bar)	1.51	2.86
Intake temperature (runner) (K)	353	423
EGR rate (simulated) (%)	10.3	0
Ambient conditions at SoI (calculated)		
Temperature (K)	~925	~1045
Density (kg/m^3)	~21.8	~32

4.2.3 *Fuel injection equipment*

For the optical engine, the fuel was injected through a pre-production solenoid-based injector. A single injection of a blend of two Primary Reference Fuels (PRF) is injected shortly after TDC with a rail pressure of 800bar. The seven nozzles with a nominal diameter of 139µm are equally spaced around the mini sac [150]. The production engine is fired with EU pump Diesel injected through a similar multi-hole injector / nozzle configuration to the optical engine. For this full-load condition, a rail pressure of 1600 bar was used. More parameters of the FIE is listed in Table 9.

Table 9: Fuel injection equipment specifications

Injector specifications		
	Optical Engine [150]	Production Engine
Nozzle diameter (µm)	139	Similar*
Number of holes (#)	7	
K-factor	1.5	
L/D	5.59	
Injection parameters		
Injection pressure (bar)	800	1600
Injected fuel mass (mg/cycle)	25.9	56.1
Start of injection (˚CA ATDC)	~2	~-11
Fuel	58 vol% heptamethylnonane (iso-$C_{16}H_{34}$) 42 vol% n-hexadecane (n-C_{16}-H_{34})	EU reference Diesel
Fuel temperature (°C)	90	150
Cetane number	50.7	

4.2.3.1 *Optical engine reference fuel*

The engine was operated with a blend of two PRFs named n-hexadecane and heptamethylnonane. The selection of this binary mixture was an attempt of achieving a simple 2-component Diesel surrogate, whose liquid-phase physical properties and ignition properties were closer to those of a real Diesel fuel than those of a blend of n-heptane and isooctane which were used in previous studies [146].

4.2.3.2 *Optical engine rail pressure and rate of injection*

The rate of injection was measured in a Moehwald HDA rate and quantity-measuring device. The measurements are based on the change in hydraulic pressure when fuel is injected into a pressurised, fuel-filled chamber with CV. The injection mass flow and quantities are then computed as a function of chamber pressure and speed of sound. The used hardware and experimental process is described in more detail in [151].

4.2.4 Optical engine - spray characterisation

4.2.4.1 Optical access

The engine allows optical access through fused silica windows (50 mm W x 25 mm H) at the top of the cylinder liner (see Figure 41). Emission and cylinder pressure measurements were conducted using a classic titanium piston.

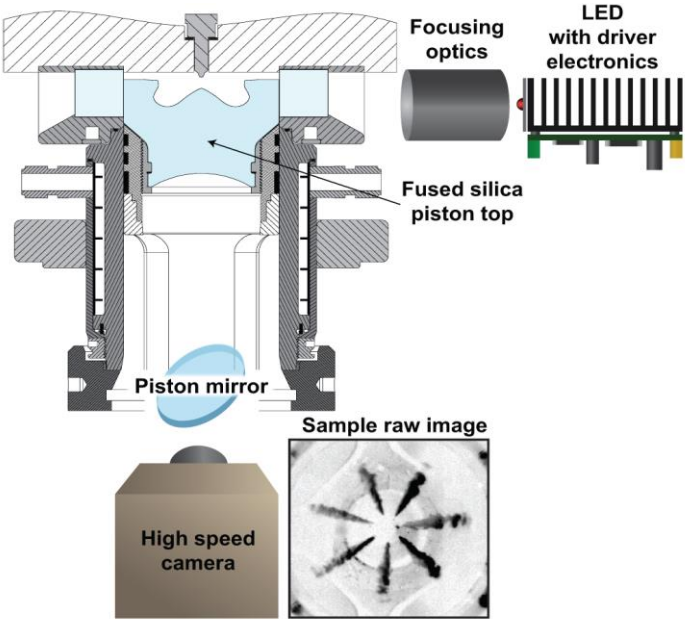

Figure 41: Schematic of the elastic scattering imaging setup for the GM 1.9L optical single cylinder engine [144]

For optical investigations, a fused silica piston replaced the titanium piston. Geometric adaptation of the fused silica piston in comparison its titanium counterpart included a wider crevice and larger top height to facilitate the image acquisition at a minor effective compression ratio penalty [144]. This geometric variation, even if they are minor, must be considered when attempting to link together the data acquired under motored and fired conditions.

4.2.4.2 Fuel injection imaging setup

To capture temporally and spatially resolved spray characteristics, an elastic scattering imaging technique was applied during motored operation. Over the course of 45 consecutive cycles, 300 images per injection event are taken. The raw images are then background subtracted and corrected for distortion. A full description of the image processing routine can be found in Busch *et al* in [144].

4.2.5 Combustion characterisation

In the optical engine, a Kistler 6125b pressure transducer mounted instead of the glow plug delivers a digitised pressure measurement at 0.25 ˚CA intervals. The pressure trace, which is an ensemble-average of 50 cycles, is then processed with an iterative, two-zone model that considers temperature and composition of the gas. To account for heat transfer and crevice flow effects, the AHRR of the motored pressure trace is subtracted from its fired counterpart. To smooth the fired cylinder pressure traces, a cosine-symmetric low pass FIR filter is used.

The experimental data for the production engine is delivered from experiments performed at Ricardo Ltd as part of a separate project. This allows direct access to the original data and knowledge of operating conditions. The downside is that the cylinders have no optical access, so the only available data are the global in-cylinder pressure and its derivative, the RoHR. This is usually the case when real metal engines are under development and highlights the importance of truly predictive CFD.

5 Numerical setup

5.1 Mathematical background of the used sub models

The simulations in this work are conducted using Ricardo VECTIS. It is a commercially available, RANS based CFD solver with a long history of application for internal combustion engine simulation [152]. Like many other commercial CFD packages, RS VECTIS offers a range of largely standard sub-models, which are listed in Table 10. This similarity allows for the methodology presented here to be carried over to other codes and may be extended to LES treatment of turbulence.

Table 10: Numerical Setup

Selected numerical sub models	
Turbulence model	Standard k-ε [80]
Spray injection method	Table (single size)
Droplet tracking method	Eulerian-Lagrangian
Droplet break-up model	KH-RT with Levich switching criterion [12, 153]
Droplet drag model	Putnam [154]
Droplet evaporation	Spalding correlation [94, 95]
Phase interaction	Droplet-droplet & droplet-turbulence (two-way coupling)
Auto-ignition model	Livengood-Wu model [155]
Combustion model	Ricardo’s Two-Zone Flamelet (RTZF) [156]
Laminar flame speed model	Metghalchi & Keck model [157]
Turbulent flame speed	Gülder equation [158]

In the following subsections, the mathematical background of the sub models and their modelling coefficients is provided.

5.1.1 *Turbulence model*

The turbulent motion in this work is modelled using the Standard k-ε turbulence model. A full description of all terms would be lengthy but can be found in Jones *et al* in [80]. Here the focus is on the two terms that have a major impact on the quality of the simulation. The terms C_1 and C_2 are responsible for scaling the dissipation rate of the turbulent kinetic energy. A higher C_2 increases dissipating effects and consequently increases the diffusion of the gas phase. The transport equation for the turbulent kinetic energy (Eq 2) and its dissipation rate (Eq 3) in the standard k-ε model are:

$$\frac{\partial(\rho k)}{\partial t}+\frac{\partial(\rho U_i k)}{\partial x_i}=\frac{\partial}{\partial x_i}\left[\left(\mu_L+\frac{\mu_t}{\sigma_{k-t}}\right)\frac{\partial k}{\partial x_i}\right]+G-\rho\epsilon \qquad \textbf{\textit{Eq 2}}$$

$$\frac{\partial(\rho\epsilon)}{\partial t}+\frac{\partial(\rho U_i\epsilon)}{\partial x_i}=\frac{\partial}{\partial x_i}\left[\left(\mu_L+\frac{\mu_t}{\sigma_{\epsilon-t}}\right)\frac{\partial k}{\partial x_i}\right]+\frac{\epsilon}{k}\left(C_1G-C_2\rho\epsilon+C_3\rho k\frac{\partial U_i}{\partial x_i}\right) \qquad \text{Eq 3}$$

Initial trials varying the turbulence dissipation coefficients showed a strong sensitivity of jet penetration. For this reason, they are selected for closer investigation.

5.1.2 Droplet introduction

The droplets are introduced as a chain of spherical blobs that are grouped in parcels of droplets with similar attributes and as such treated with the underlying equations. The diameters of these initial droplets can be defined either by the user or be left to be calculated by various initial droplet size correlations mentioned in the literature review (section 3.2.4.1). In this work, a user-defined droplet introduction typically known as “Table introduction” is selected. This list of droplet sizes vs probability is flexible and introduces no new variables. The disadvantage is that it does not consider any nozzle flow characteristics or ambient conditions. To further simplify the droplet introduction, only a single droplet size is introduced. Multiple impact studies conducted throughout the study showed that there was no apparent benefit of applying more complex droplet introduction methods and distributions.

5.1.3 Momentum conservation

The momentum equation for a droplet of mass m_d is described by Newton’s Second Law (Eq 4) in which C_d is the aerodynamic drag coefficient, A_f is the projected area of the droplet in moving direction, A_{drag} is a user-defined tuning coefficient, ρ_g is the density of the surrounding gas and the relative velocities between the droplets and the gas $\vec{U}$. This momentum contribution is then added into the energy and momentum conservation equations as a source term. The initial screening of simulation coefficients highlighted A_{drag} as highly influential, so it was added to the list of coefficients to be investigated with more detail.

Droplet momentum

$$m_d\frac{d\vec{V}}{dt}=\frac{1}{2}C_dA_fA_{drag}\rho_g|\vec{U}|\vec{U} \qquad \textbf{\textit{Eq 4}}$$

The drag coefficient C_d is calculated by the Putnam model, which is expressed as shown in Eq 5. The model defines C_d to be that of a sphere for cases where droplet Reynolds numbers exceed1000. Based on this, it was hypothesised that a value of $0 < A_{drag} \leq 1$ in Eq 5 is physically reasonable as it accounts for the droplet drag coefficient for deformed droplets. Although values >1 are theoretically possible, they would not be physically justifiable.

Drag coefficient

$$C_d = \begin{cases} \frac{24}{Re_d}\left(1 + \frac{1}{6} Re_d^{2/3}\right) & for\ Re_d \leq 1000 \\ 0.424 & for\ Re_d > 1000 \end{cases} \qquad \textbf{\textit{Eq 5}}$$

5.1.4 *Mass and energy conservation*

During the evaporation of the droplet, it experiences simultaneous heat and mass transfer processes as depicted in the schematic in Figure 42. By means of convection and conduction, the heat from the surrounding gas is transported into the droplet surface. The vaporised fuel is returned to the gas stream via convection and diffusion. A detailed recollection of the underlying equations would be lengthy but is offered in the original documentation [94, 159, 160].

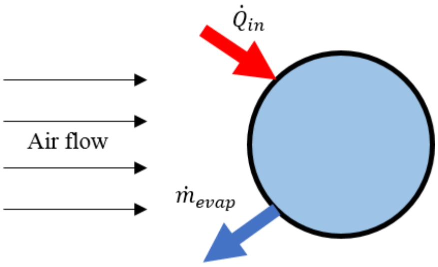

Figure 42: Schematic of droplet heat and mass transfer

5.1.5 *Spray modelling*

The comparison between real liquid fuel break-up and common computational representation is shown in Figure 43. What is thought to be a somewhat intact liquid core gradually breaking up into droplet ligaments is computationally represented as a chain of large spherical parent droplets breaking up into several smaller child droplets. Droplets with identical physical properties are grouped into parcels. Spray break-up is typically divided into two separate processes commonly termed as *primary* and *secondary break-up* [153]. The droplets undergo secondary break-up where the liquid droplets become unstable and further break-up into smaller droplets.

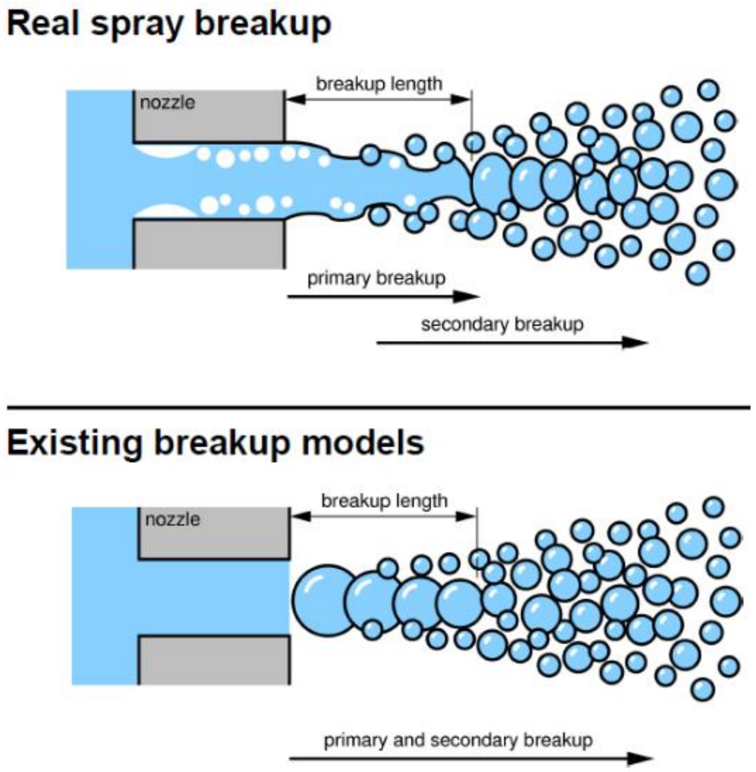

Figure 43: Real spray break-up vs common break-up models [161]

The following is an overview of the governing equations for the droplets moving in a carrier fluid. The two-phase flow is considered a dispersed liquid phase in the continuous gas phase based on the Lagrangian approach

5.1.5.1 *Hybrid break-up models*

In Hybrid break-up models, two individual break-up models are merged to improve the accuracy of the predictions for high-speed sprays. The upstream model, also called the primary break-up model, deals with the initial disintegrations of the liquid jet into droplets. The secondary break-up model then further breaks up these initial large droplets into smaller droplets. The interface between the two models is handled with a switching criterion that calculates the break-up length. The following hybrid break-up models are available in VECTIS (defined as *primary break-up* / *secondary break-up*):

- Kelvin-Helmholtz / Rayleigh-Taylor model (KH-RT)
- Kelvin-Helmholtz / Taylor-Analogy-Break-up model (KH-TAB)
- Kelvin-Helmholtz / Pilch model (KH-Pilch)

In this work, the commonly hybrid break-up model named KH-RT [12] is used. It is based on the Kelvin-Helmholtz (KH) and Rayleigh-Taylor (RT) instability theory. In the KH-RT model, a chain of droplets is introduced with the so-called "blob" method. A common approach would be to define the droplet diameter to be approximately equal to that of the effective nozzle orifice to replicate a liquid core. A discharge coefficient model calculates the injection velocity, effective nozzle diameter and spray cone angle based on ambient conditions and basic nozzle geometry.

5.1.5.2 Primary break-up modelling (KH instability model)

According to Liu *et al* [89], aerodynamic effects, of which the stripping-type is the main mechanism, dominate the break-up process. KH instabilities develop at the interface of two fluids with enough relative velocity (see Figure 44).

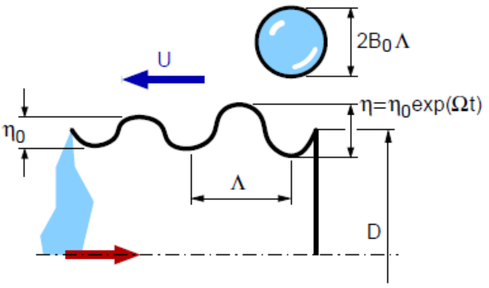

Figure 44: A schematic view of the droplet break-up based on KH instability [161]

The main assumption is that the liquid jet becomes unstable due to aerodynamic interactions at this interface. The initial disturbances are amplified by the aerodynamic interaction between the liquid and the gaseous surrounding. The result are self-exciting surface oscillations that eventually result in detachment of wave crests in form of droplets.

Evolution of the parent droplet

The evolution of these surface disturbances is based on the first-order linear instability analysis of a cylindrical liquid jet injected into a stationary incompressible gas. An infinitesimal axisymmetric disturbance of amplitude, η_0, is imposed on the jet surface, which further evolves in time as shown in Eq 6, where ω is the wave growth rate and the t is time.

Amplitude of disturbance $$\eta = \eta_0 exp(\omega t)$$ ***Eq 6***

The fastest growing wave and its associated maximum growth rate and wave length are identified using curve fitting of the numerical solution as shown in Eq 7 and Eq 8 (see Reitz [162]). They in turn depend on the Ohnesorge Number Z (Eq 9), the Taylor Number T (Eq 10) and the Weber numbers of liquid the gas We (Eq 12 & Eq 13) and the surface tension σ.

Max. wave growth rate

$$\Omega_{\mathrm{KH}}\left(\frac{\rho_l D_d^3}{8\sigma}\right)^{0,5}=\frac{0.34+0.38We_g^{1.5}}{(1+Z)(1+1.4T^{0.6})}$$

Eq 7

Wavelength

$$\frac{\Lambda_{\mathrm{KH}}}{D_d}=4.51\frac{(1+0.45Z^{0.5})(1+0.4T^{0.7})}{\left(1+0.865We_g^{1.67}\right)^{0.6}}$$

Eq 8

Ohnesorge Number

$$Z=\frac{We_l^{0.5}}{Re_l}$$

Eq 9

Taylor Number

$$T=ZWe_g^{0.5}$$

Eq 10

Reynolds Number

$$Re_l=\frac{\rho_l U^2 D_d}{2\mu_l}$$

Eq 11

Weber Number (liquid)

$$We_l=\frac{\rho_l U^2 D_d}{2\sigma}$$

Eq 12

Weber Numbers (gas)

$$We_g=\frac{\rho_g U^2 D_d}{2\sigma}$$

Eq 13

With given maximum growth rate and the corresponding wavelength, the characteristic break-up time $\tau_{b,KH}$ is calculated as shown in Eq 14. The B_1- coefficient is responsible for the rate at which the parent droplet shrinks. Its impact on the simulation is profound and is therefore added to the list of coefficients investigated in this thesis.

Characteristic break-up time

$$\tau_{b,KH}=\frac{3.788B_1D_d}{2\Omega_{KH}\Lambda_{KH}}$$

Eq 14

The droplet then continuously decreases its diameter at every time step until it reaches a stable size $D_{stab,KH}$. The rate at which the droplets shrink is approximated as

Rate of droplet shrinking

$$\frac{dD_d}{dt}=-\frac{D_d-D_{stab,KH}}{\tau_{b,KH}}$$

Eq 15

To approximate the break-up process under real high-speed conditions more accurately, the model includes considerations where small child droplets are shed from the parent droplet (based on Patterson and Reitz from [163]). The liquid mass of these new parcels is removed from the parent parcels as they are updated with a new droplet number $N_{d,n}$ and diameter $D_{d,n}$. Throughout this process of child droplet detachment, the following equations for mass conservation (Eq 16) and maintaining the Sauter mean diameter (Eq 17) must be satisfied to correspond with the break-up rate calculated in Eq 15.

Mass conservation

$$N_d D_d^3 = N_{d,n} D_{d,n}^3 + N_c D_c^3$$

Eq 16

Sauter mean diameter

$$D_d = \frac{N_{d,n} D_{d,n}^3 + N_c D_c^3}{N_{d,n} D_{d,n}^2 + N_c D_c^2}$$

Eq 17

The following two assumptions lead to the above two conservation equations being formed to the form shown in Eq 18 and Eq 19 that allows the calculation of the droplet diameter for the updated parent parcel $D_{d,n}$ and the number of droplets in the new child parcel N_c.

- The number of droplets in the updated parent parcel is equal to that in the original parcel ($N_{d,n} = N_d$).
- The diameter of the child droplets is equal to that of the stable droplet size ($D_c = D_{stab,KH}$).

$$N_d D_d^2 (D_d - D_c) = N_{d,n} D_{d,n}^2 (D_{d.n} - D_c)$$

Eq 18

$$N_c = \frac{N_d D_d^3 - N_{d,n} D_{d,n}^3}{D_c^3}$$

Eq 19

The droplet drag coefficients of the droplets within the break-up length, which represent the liquid core of the spray, are reduced to account for higher liquid fraction near the liquid core.

Evolution of the child droplet

The child droplets detaching from the parent droplet are regrouped into new parcels with their own droplet count N_c (see Eq 19) and diameter D_c. To limit the number of generated droplet parcels, the child droplet parcels are only created if the mass of the predicted child parcel given by N_c and D_c reaches at least 3% of the initial mass of the parent droplet parcel.

The child droplet diameter D_c is calculated following Eq 20. The B_0-coefficient is the tuning parameter that defines the size of the child droplet (and the stable droplet size $D_{stab,KH}$) and therefore also has an effect on the rate at which the parent size is shrinking. The impact of this coefficient will be investigated as part of this thesis.

Child droplet diameter

$$D_c = B_0 2 \Lambda_{KH}$$

Eq 20

The child droplets breaking away from the parent droplets within the break-up length are treated with secondary break-up mechanisms with a reduced drag coefficient to replicate reduced aerodynamic effects where there is assumed to be a high liquid volume fraction.

5.1.5.3 Secondary break-up modelling (RT instability model)

The RT instability model is then used in conjunction with KH to predict the secondary break-up of the droplets. Like the KH instability model, the RT instability model computes the frequency of the fasted growing wave Ω_{RT}, the corresponding wavelength Λ_{RT} and the wave number K_{RT}. Their values, however, are calculated as shown in the following equations.

Max. wave growth rate

$$\Omega_{\mathrm{RT}} = \sqrt{\frac{2}{3\sqrt{3\sigma}}\frac{\left[a\left(\rho_l-\rho_g\right)\right]^{3/2}}{\rho_l+\rho_g}}$$

Eq 21

Wave number

$$K_{RT} = \sqrt{\frac{a\left(\rho_l-\rho_g\right)}{3\sigma}}$$

Eq 22

Wavelength

$$\Lambda_{\mathrm{RT}} = \frac{2\pi C_3}{K_{RT}} = D_{stab,RT}$$

Eq 23

Droplet acceleration

$$a = \frac{3}{4}C_d\frac{\rho_g U^2}{\rho_l D_d}$$

Eq 24

The RT model predicts instabilities on the surface of the droplets that grow until a certain characteristic break-up time τ_{RT} when the drop finally breaks up. Once waves begin to grow on the surface of the droplet, the wave growth time Ω_{RT} is tracked. The wave growth time is then compared to the break-up time. Usually, C_{RT} is a tuning factor and that is kept at unity.

Characteristic break-up time

$$\tau_{RT} = \frac{C_{RT}}{\Omega_{RT}}$$

Eq 25

If the RT waves have been growing for a time greater than the break-up time, the drop is assumed to break-up. The calculated rate of the droplet shrinking until it reaches the stable size is of this stable droplet is shown in Eq 26. This process is influenced by a modifiable coefficient C_3 as becomes clear in Eq 23.

Rate of droplet shrinking

$$\frac{dD_d}{dt} = -\frac{D_d - D_{stab,RT}}{\tau_{RT}}$$

Eq 26

Both C_{RT} and C_3 are influential modelling coefficients and will be investigated in more detail as part of this thesis.

5.1.5.4 Switching criterion

The switch between when primary and secondary break-up equations is calculated by the break-up length L_b in the Levich model (Eq 27). The user can adjust the coefficients A_{bu} and B_{bu}. The original authors recommended a value of 5.5 and 0 respectively. While A_{bu} scales the break-up length based on the nozzle size and therefore appears to scale to some real boundary condition, B_{bu} being a simple addition is arguably arbitrary. Therefore, A_{bu} but not B_{bu} is added to the list of coefficients to be investigated.

Break-up length

$$L_b = A_{bu} D_n \sqrt{\frac{\rho_l}{\rho_g}} + B_{bu} \qquad \textbf{\textit{Eq 27}}$$

5.1.6 Turbulent Schmidt number

The turbulent Schmidt number Sc_t is defined as the ratio between eddy viscosity μ_t and eddy diffusivity K. By this definition, it relates turbulent momentum transport to turbulent mass transport.

Turbulent Schmidt number

$$Sc_t = \frac{\mu_t}{K} \qquad \textbf{\textit{Eq 28}}$$

5.1.7 RTZF combustion model

The RTZF combustion model is development of Ricardo Software. To the best of our knowledge it has not been previously been used to simulated ECN Spray A cases. The RTZF model solves a transport equation for each virtual species with the source terms determined by the generalised burn rate and can model both pre-mixed and non-premixed modes [156]. This approach sets it aside from other flamelet based combustion models.

The model uses ‘virtual’ species (unburnt air, unburnt fuel, residual air, liquid fuel etc.) and solves the transport equations for these species. The source & sink terms in the transport equations are determined by the combustion model, which determines the rate of conversion of unburnt species to burnt species. In this combustion model, the domain is divided into two zones, the burned and unburned zone (see Figure 45).

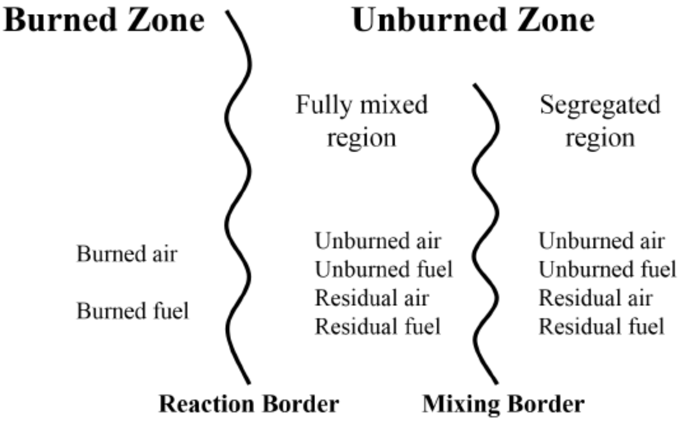

Figure 45: Representation of the two zones in the RTZF combustion model [164]

The unburned zone is further divided into the “segregated region” and “fully mixed region”. In the segregated region, air, fuel and residuals are molecularly separated and not ready for any chemical reactions. Fluid motion and diffusion on a molecular level mixes the reactants until they can be categorised as “fully mixed” and can undergo chemical reactions. After the combustion has fully consumed the reactants, they are considered fully burned and placed in the “burned zone”. In the case of a premixed combustion mode, the segregated region does not exist and the governing equations in this region are ignored. The combustion products consist of 11 chemical species (typical of those from combustion of a hydrocarbon fuel) and these are determined based on the virtual species and an assumed state of equilibrium for the calculated state (pressure, temperature, equivalence ratio etc.). Equilibrium coefficients and thermodynamic properties are based on the Joint Army-Navy-NASA-Air Force (JANNAF) tables.

The combustion calculation is divided into three stages:

1. Pre-combustion stage: In this stage, the mixing rate of all present gaseous reactants in a non-premixed mode is calculated. If the mix is initially defined as homogeneous, this stage is skipped.
2. Combustion stage: As soon as an auto-ignition model identifies a combustible mix, the chemical reactions with high-temperature energy release are initiated. It is assumed that both chemical and turbulence-controlled mechanisms are simultaneously present with their relative burn rates
3. Post-combustion stage: For given thermal conditions and mixture composition, thermochemical property tables that are stored in Ricardo Software’s VECTIS and WAVE simulation tools can then output the new thermodynamic state and species concentrations as a one-step instantaneous conversion.

5.1.7.1 Pre-Combustion stage

For non-premixed combustion such as the cases investigated in this work, the turbulent mixing rate $\omega_{mix,i}$ between fuel and air (see Eq 29) is approximated as a direct extension of the Eddy-Break-Up (EBU) model [165, 166]. The integral time scale t_I is approximated with a user-defined coefficient C_{mix} and k/ϵ. Conducted sensitivity studies showed that in the cases in this work, C_{mix} is robust towards changes in value indicating rapid mixing.

Turbulent mixing rate

$$\omega_{mix,i} = \frac{\rho Y_i^{seg}}{t_I} \cong - C_{mix} \frac{\epsilon}{k} \rho Y_i^{seg}$$

Eq 29

5.1.7.2 Combustion stage

When a computational cell exhibits a combustible mixture characteristic, a lumped one-step reaction converts the mixed species to generic intermediate ignition species. The probability of reactant auto-ignition P_{ig} is estimated by the Livengood-Wu integral [155] (Eq 30). The ID-time t_{ig} of the chemical reaction is approximated as shown in Eq 31. The autoignition coefficient C_{ig} gives the user the opportunity to adjust the chemical ID time and plays a leading role in this study. The empirical coefficients A, n and T_a are not further described or investigated here and remain at default values.

Probability of reactant auto-ignition

$$P_{ig} = C_{ig} \int \frac{dt}{t_{ig}}$$

Eq 30

Ignition delay time

$$t_{ig} = \frac{Ap^{-n}}{\phi^{n_\phi}} \exp\left(\frac{T_a}{T}\right)$$

Eq 31

Once auto-ignition is initiated, the reaction rate ω_{ig} (see Eq 32) is determined either by the chemical kinetics timescale τ_c or the simulation time-step Δt (whichever is greater). The chemical reaction rate τ_c is dependent on the pre-exponential constant B (not a user constant) and the activation and flame temperatures T_a and T_f (Eq 34). On a side note, if the CPV model were to be used to determine the reaction rate, ω_{ig} is expressed as Eq 33, where $\dot{C}$ is taken from the CPV library.

Reaction rate (Livengood-Wu & Shell model)

$$\omega_{ig} = \begin{cases} 0 & before\ ignition \\ \dfrac{\rho \sum_i (Y_{mix})}{\max(\tau_c, \Delta t)} & after\ ignition \end{cases}$$

Eq 32

Reaction rate (CPV model)

$$\omega_{ig} = \rho \sum_i (Y_i - Y_i^{seg})\dot{C} \quad \text{with } \dot{C} = \frac{dC}{dt}$$

Eq 33

Chemical reaction rate

$$\tau_c = Bexp\left(\frac{T_a}{T_f}\right)$$

Eq 34

As soon as combustion is initiated, chemical reactions generate combustion products through turbulent mixing. The reaction zone is hereby assumed an accumulation of unburned und burned gaseous pockets being mixed by turbulent eddies. The influence of mixing on the mean reaction rate ω_{pr} (Eq 35) is described by progress variable fluctuations $\widetilde{C''^2}$ (Eq 36) and a turbulence time scale τ_t (Eq 38) as described in the EBU model [165, 166] for premixed combustion. The combustion progress variable (Eq 37) is defined as the ratio of burnt species to all species within that cell. The turbulent mixing time scale τ_t is a function of the characteristic length scale l_c and the turbulent flame speed s_t.

Turbulence-controlled reaction rate

$$\omega_{pr} \propto \frac{\bar{\rho}_u \widetilde{C''^2}}{\tau_t}$$

Eq 35

Progress variable fluctuations

$$\bar{\rho}_u \widetilde{C''^2} = \overline{\rho_u (C - \tilde{C})^2} = \bar{\rho}_u\left(\widetilde{C^2} - \tilde{C}^2\right) = \bar{\rho}_u \tilde{C}(1 - \tilde{C})$$

Eq 36

Combustion progress variable

$$\tilde{C} = \frac{Y_{BA} + Y_{BF}}{Y_{BA} + Y_{BF} + Y_A + Y_F + Y_{RA} + Y_{RF}}$$

Eq 37

Turbulence time scale

$$\tau_t = \frac{l_c}{S_t}$$

Eq 38

In the third equality of Eq 36, which is only valid for a two-zone assumption, $\tilde{C}$ for the unburnt zone is 0 and for the burnt zone 1. Given these assumptions, the RTZF turbulence-controlled reaction rate is expressed as shown in Eq 39. The modifiable A_o- coefficient incorporates the proportionality indicated in Eq 35.

Turbulence controlled reaction rate

$$\omega_{pr} = A_o \frac{\bar{\rho}_u \tilde{C}\left(1 - \tilde{C}\right)}{\tau_t}$$

Eq 39

To ensure validity for non-premixed conditions, a Tennekes vortex structure is assumed to define the ratio of fully mixed reactant volume V_m to the total volume V_{tot} (Eq 40). This is done to account for inhomogeneity of turbulent mixing in the non-premixed flames. In non-premixed flames the value of r_{vol} is small, which reduces the burn rate.

Ratio of fully mixed reactant volume to total volume

$$r_{vol} = \frac{V_m}{V_{tot}}$$

Eq 40

By introducing Eq 40 and Eq 38 into Eq 39, a generalised form of the burn rate can be expressed (Eq 41). This rate generalised burn rate is valid for both premixed and non-premixed combustion modes.

Generalised burn rate

$$\omega_f = A_0 r_{vol} \left(\frac{S_t}{l_c}\right) \bar{\rho}_u \tilde{C}\left(1 - \tilde{C}\right)$$

Eq 41

The turbulent flame speed S_t is defined as the Gülder equation [158] shown in Eq 42. The laminar flame speed S_l is calculated with the empirical Metghalchi & Keck model [157] shown in Eq 43.

Turbulent flame speed

$$S_t = S_l(\phi) + S_l(\phi)\alpha_{turb}\left(\frac{u'}{S_l(\phi)}\right)^q$$

Eq 42

Laminar flame speed

$$S_l = S_l^0 \left(\frac{T_u}{T_0}\right)^\alpha \left(\frac{p}{p_0}\right)^\beta$$

Eq 43

In partially premixed mode of combustion, where direct chemical conversion of the reactants and instantaneous conversion of mixing reactants occurs simultaneously, an overall burn rate must be calculated. The overall burn rate ω_b is considered a sum of these conversion rates (Eq 44). A limiting factor hereby is the mixing rate calculated in Eq 29. The implication of this is that in the presence of a non-premixed mode of combustion, the overall reaction rate can never be higher than the mixing rate of fuel and fresh air.

Overall burn rate

$$\omega_b = \left(\omega_f + \omega_{ig}\right) \leq \rho \frac{\sum_i Y_{mix,i}}{\Delta T} = min(\omega_f, \omega_{mix})$$

Eq 44

In summary, at purely premixed or non-premixed conditions, the general burn rate corresponds either to the premixed (Eq 45) or non-premixed burn rate (Eq 46).

Purely premixed burn rate

$$\omega_b = \omega_{pr}$$

Eq 45

Purely non-premixed burn rate

$$\omega_b = \omega_{mix}$$

Eq 46

Depending on whether the flame is purely premixed or non-premixed, either the coefficients of burn velocity A_0 from Eq 39 or the turbulent flame speed α_{turb} from Eq 42 are eliminated. But in a partially premixed flame, with which the ECN Spray A shares significant characteristic overlaps (see Pei *et al* [72], reactant conversion can occur at both burn rates (ω_{ig} and ω_f) simultaneously at various locations. For this reason, both the burn velocity coefficient A_0 and turbulent flame speed coefficient α_{turb} are expected to have some effect on the simulation and are therefore included in the list of investigated coefficients.

5.1.7.3 Post-combustion stage

The reactions rates contributing to heat release are assumed far greater than the flow timescales. This is the basis for assuming chemical equilibrium in the burned zone and can be derived from JANNAF tables [167]. For given thermal conditions and mixture composition of burned/unburned air and fuel, WAVE property files can output the new thermodynamic state and species concentrations as a one-step, instantaneous conversion. These property files are derived from Ricardo Software’s 1D gas dynamics simulation tool named Ricardo WAVE. Only the main combustion products that are present in complete and incomplete combustion of hydrocarbon fuels are considered: CO, CO2, H, H2, H2O, N2, NO, O, O2, OH and N.

The RTZF model calculates the enthalpies of formation from change of absolute enthalpy to change in total sensible enthalpy. The total heat release is derived from heat release contributions in every given time-step n from the difference in formation enthalpies $h^{n}_{\dots}$ based on the conditions in every computational cell q^{n}_{cell} (Eq 47) the inlet/outlet boundaries q^{n}_{io} (Eq 48) and the compensation due to cooling effect from the spray q^{n}_{spray} (Eq 49).

Cell heat release

$$q^{n}_{cell} = \sum_{i=1}^{N_{cell}} \left(\Delta h^{0,n-1}_{f,i} - \Delta h^{0,n}_{f,i}\right)$$

Eq 47

Heat release from inlet/outlet boundaries

$$q^{n}_{io} = \sum_{j=1}^{N_{io}} m^{\dot{n}}_{j} \Delta T \left(h^{n}_{j} - h^{n}_{s,j}\right)$$

Eq 48

Cooling effect from the spray

$$q^{n}_{spray} = \sum_{k=1}^{N_{drop}} m^{n}_{evap,k} \left(h^{n}_{fg,k} + h^{n}_{f,k}\right)$$

Eq 49

The final heat release $\dot{q}^n$ is then a sum of these contributions over the time-step size Δt (Eq 50). In the simulated cases here, the heat transfer to the walls is suppressed to adhere to the adiabatic ECN measurements ($q_{io}^n = 0$).

Total heat release
$$\dot{q}^n = \frac{1}{\Delta t}\left(q_{cell}^n + q_{io}^n + q_{spray}^n\right) \quad \textbf{Eq 50}$$

5.2 Geometrical Setup

5.2.1 Constant volume vessel

The geometry shown in Figure 46 is that of the CV – vessel. It is a cubical geometry with a side length of 105mm. It is split into three main regions. In the core of the cube, where the spray is injected, a mesh refinement with a quarter of the base mesh size is added. Towards the bottom of the geometry, where the vapour plume travels slower, a mesh refinement of half the base mesh size is enough. The rest of the geometry is unrefined as there is only little fluid movement in this outside area.

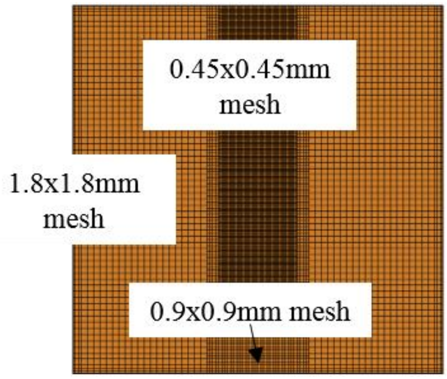

Figure 46: Geometry and meshing strategy for the CV- vessel

5.2.2 Light duty engine geometries

In the simulations of the engine cases, three meshes for the different purposes were used (see Figure 47). The first, on the left, is the base mesh, which is used for the compression stroke. When the cycle approaches SoI, the finest mesh, which is a quarter size of the base mesh, is used for all regions. This mesh is used throughout the injection and combustion phase. From after the end of combustion, when most of the high-speed motion is completed, until the end of the cycle, a mesh half the size of the base is used until the end.

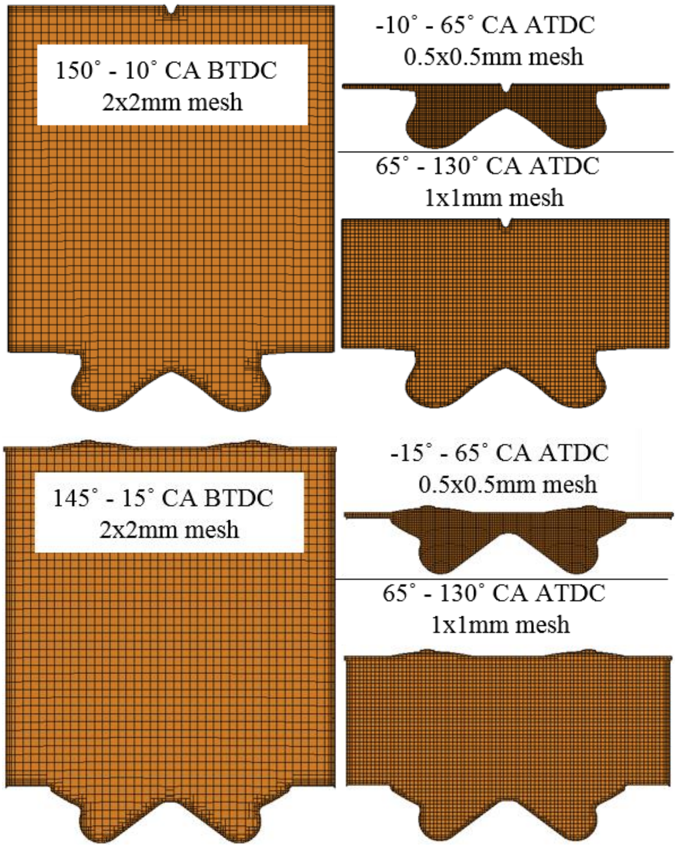

Figure 47: Geometry and meshing strategy for the optical engine (top) and production engine (bottom)

5.3 Computational and experimental definitions

The modelling standards for spray and jet penetration are aligned with the recommendations from the ECN [122]. This means that the spray penetration is defined as the maximum axial location from the nozzle exit where 99% of the total droplet mass has evaporated. The jet penetration is determined by the farthest downstream location of 0.1% fuel mass fraction.

The LoL stated by the ECN is defined as the first axial location of Favre-average OH mass fraction reaching 2% of its maximum in the domain. The combustion stage of RTZF only assumes chemical equilibrium. Consequently, a transient tracking of OH mass fraction and the direct comparison of LoL is not possible. The OH threshold identifies to which degree low-temperature combustion has progressed. In the simulations, the most similar parameter that tracks the progression of combustion is the combustion progress variable.

6 Results and discussion I: Independence studies

This chapter discusses the steps to ensure model independence towards mesh size, time-step and Parcel Introduction Rate (PIR). In all figures, the independence of the Lagrangian and Eularian phases are assessed using spray and jet penetration lengths.

In a typical CFD simulation, a continuous solution is approximated using discrete computational cells that form a mesh of the domain. With an increasing number of cells, the accuracy of the solution typically increases – however, so does computational runtime. The benefits of a continuous refinement of the mesh will eventually stall after which a further refinement would not make sense. To find this sweet spot where the solutions show independence of further refinement and runtimes are as low as possible, a mesh independence study is carried out. This means the mesh size is gradually reduced until comparison metrics like spray or jet penetration show no more noticeable changes in values.

The selection of the simulation time-step has two purposes. The first is to ensure stability of the simulation and the other to minimise the numerical damping of the solution. To find the appropriate settings for the time-step either a time-step independence or a CFL-number (Courant–Friedrichs–Lewy) study is necessary. In this thesis, the former is chosen.

In a Discrete Droplet Method (DDM) approach to introducing droplets to the system, it would be too computationally expensive to track every droplet individually. Instead, droplets of the same characteristics are bundled into parcels and the equations applied to the entire parcel. The more parcels per time-step are introduced, the finer is the resolution of droplet groups with identical characteristics becomes. The top limit to this is when each parcel contains only one droplet and the lowest is one parcel will all droplets per time-step. Since the droplets are all introduced with the same initial diameter, the parcel introduction rate (PIR) is not expected to have a strong impact on the simulations. Despite this, an independence study is performed for all the spray configurations in this thesis.

6.1 Constant volume vessel

Mesh independence

The mesh independence study for the baseline Spray A condition in the CV – vessel is shown in Figure 48. The investigated mesh sizes ranged between 0.8mm and 0.38mm. Figure 48 shows little change for spray and jet penetration from 0.5mm to 0.45mm. A further reduction in mesh sizes then appears to have an impact on both metrics. This increase following the convergence is a numerical effect that occurs when mesh sizes become too small. This means that mesh independence is reached at 0.5mm, however the 0.45mm case is chosen based on a confirmation of the Courant criterion at no runtime penalty.

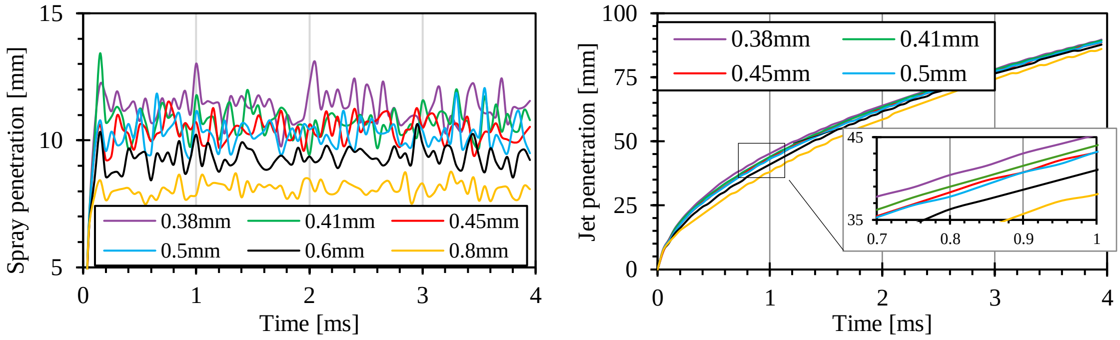

Figure 48: Mesh independence study for the Spray A condition in the CV – vessel based on temporally resolved spray (left) and jet (right) penetration

Another important factor is the runtime. The runtime on 20 cores for the six mesh variations is shown in Figure 49. The variation of runtime of the simulations with decreasing mesh sizes until 0.45mm is due to CPU performance and cluster load. The ~65% increase in runtime when the mesh size is further reduced is significant and must be considered when hundreds of simulations are scheduled to take place on a cluster.

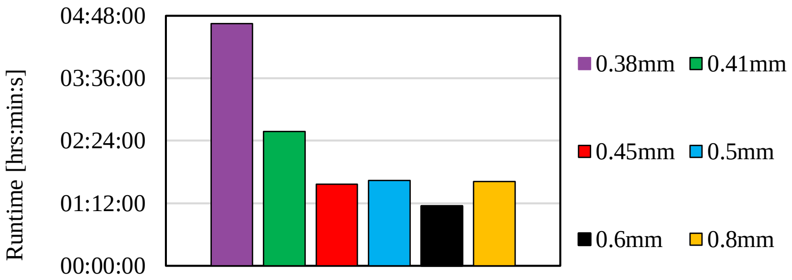

Figure 49: Runtime for the six different meshes

Time-step independence

Figure 50 shows the results of the time-step independence study of the CV – vessel. With a decrease of time-step from 10µs (orange) to 0.25µs (green), the initial spray penetration peak reduces significantly. The spray penetrations of these time-steps show only little variation during the steady state phase before sharply rising when the time-step is further reduced to 0.1µs.

The selected time-step for the following simulations is the 0.5µs variation. It shows a stabilised spray and jet penetration with only little change when the time-step is further reduced.

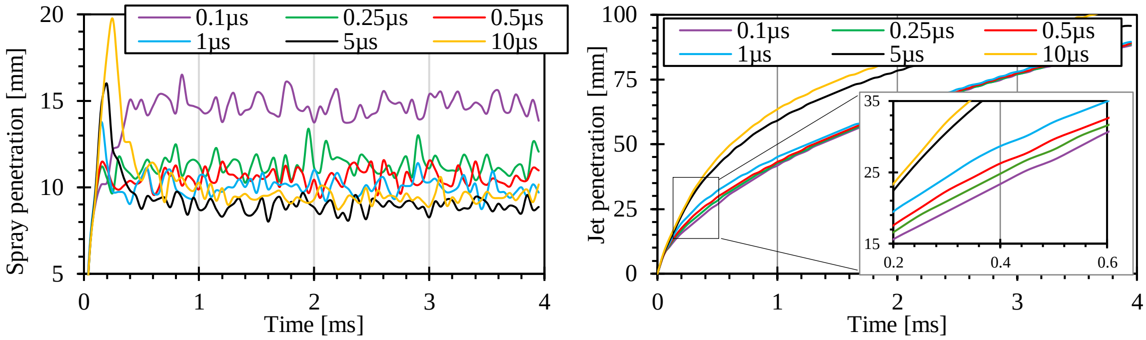

Figure 50: Time-step independence study of the CV - vessel: spray (left) and jet (right) penetration over crank angle. Selected time-step: 0.5µs

The selection of the time-step has a profound impact on the simulation runtime. The setting selection should be based on solution independence, however, when running hundreds of simulations besides customer projects, the runtime of a single simulation can have significant impact on the department routine.

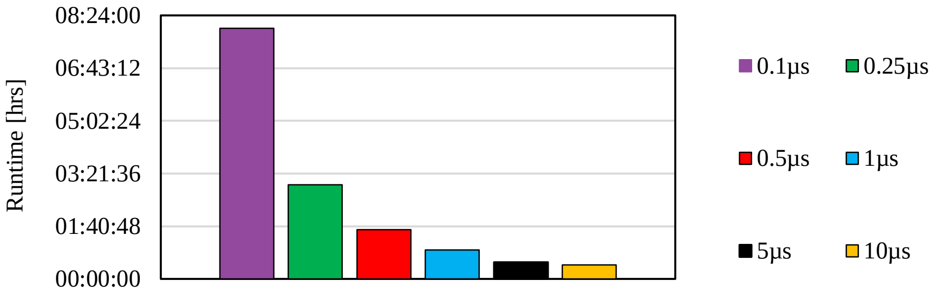

Figure 51: Runtime comparison between the different time-step options

Parcel introduction rate independence

Figure 52 shows that the PIR has a minor effect on the jet penetration. This is not the case for spray penetration. A PIR of 1mio parcels per second produces a relatively noisy spray penetration. Once increased beyond 3.6mio parcels/second, there is no significant change visible. The choice of PIR is therefore 3.6mio parcels/second.

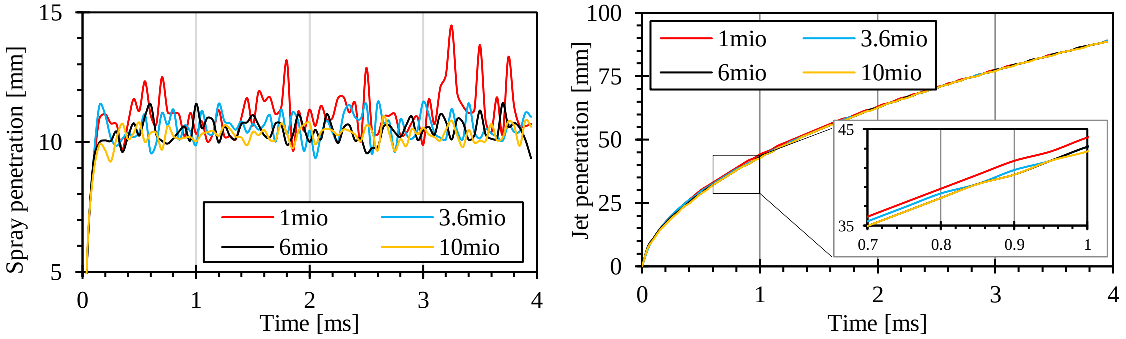

Figure 52: Parcel introduction rate independence study of optical engine - vessel: spray (left) and jet (right) penetration over crank angle. Selected PIR: 3.6mio

6.2 Optical engine

Mesh independence

The mesh independence study of the optical engine is shown in Figure 53. A mesh size range between 0.75 and 0.25mm is investigated. Besides a slight deviation in spray and jet penetration between 7 – 10˚CA, the 0.45mm (red) and 0.375mm (purple) curves follow a similar progression. The mesh size of 0.45mm is selected for further consideration because the overall similarity to the 0.375mm size. The selection is then based on the runtime benefit of the larger mesh size. The increase in spray penetration when further reducing the mesh size was discussed with reference to the CV – vessel.

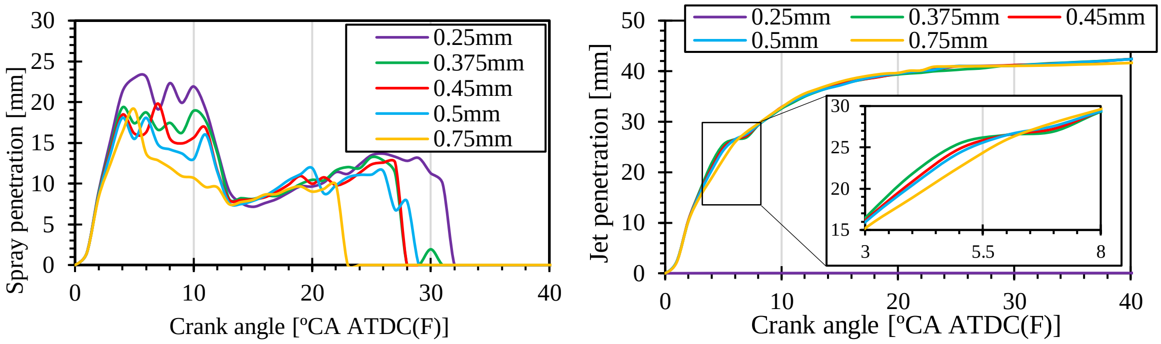

Figure 53: Mesh independence study of the optical engine: liquid (left) and vapour (right) penetration over crank angle. Selected Mesh: 0.45mm

Time-step independence

The time-step independence of the optical engine is shown in Figure 54. A reduction from 0.02 to 0.01CAs has an impact on the initial spray penetration peak. A further reduction of the time-step to 0.05CAs shows little influence for spray penetration, but a small change for jet penetration. A further reduction changes spray penetration but not jet penetration. The final selection is made to be the 0.01CAs time-step because the spray penetration appears to become independent. The jet penetration only shows little change while the overall curve characteristics are like those of the smaller time-steps. With the time-steps smaller than 0.01CAs, the simulation runtimes become unacceptably high.

Parcel introduction rate independence

The PIR of the injection process in the optical engine shown in Figure 55 has little influence on the spray and jet penetration. Slightly higher runtimes above 150K and little noticeable difference beyond 75K led to the choice of the 150K case.

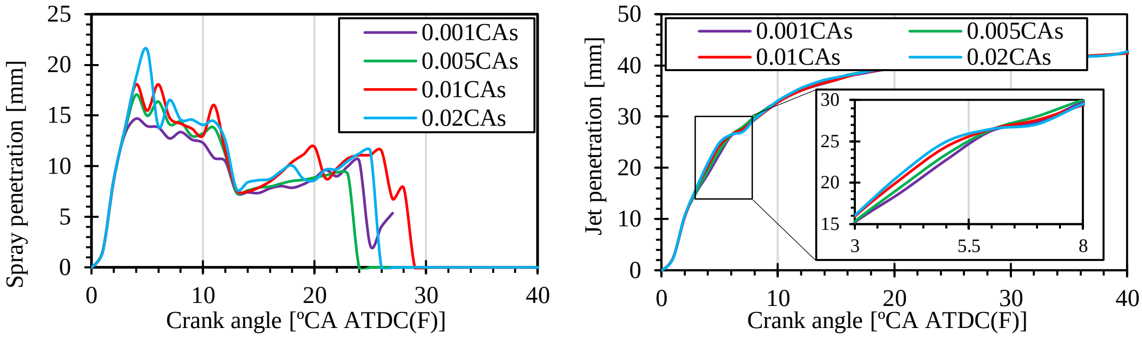

Figure 54: Time-step independence study of optical engine - vessel: liquid (left) and vapour (right) penetration over crank angle. Selected time-step: 0.1CAs

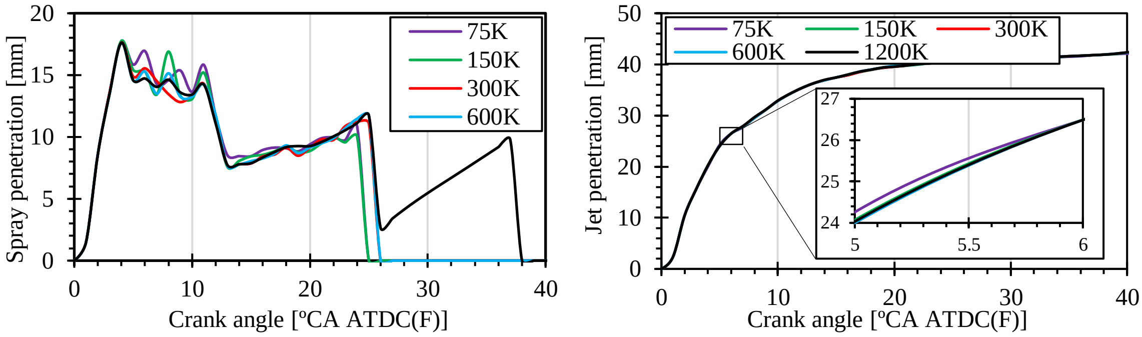

Figure 55: Parcel rate introduction independence study of optical engine - vessel: liquid (left) and vapour (right) penetration over crank angle. Selected PIR: 150K

6.3 Production engine

Mesh independence study

A similar mesh size as the optical engine is also selected for the production engine. The spray and jet penetration do not show significant variation between 0.375mm (purple) and 0.45mm (green) with exception of the initial peak just before TDC. Additionally, the vapour phase shows that after an increase from 0.75mm (blue) to 0.5mm (red), a variation against 0.375 (purple) remains small. Based on this, and the favourable runtimes, the mesh size of 0.5mm is selected.

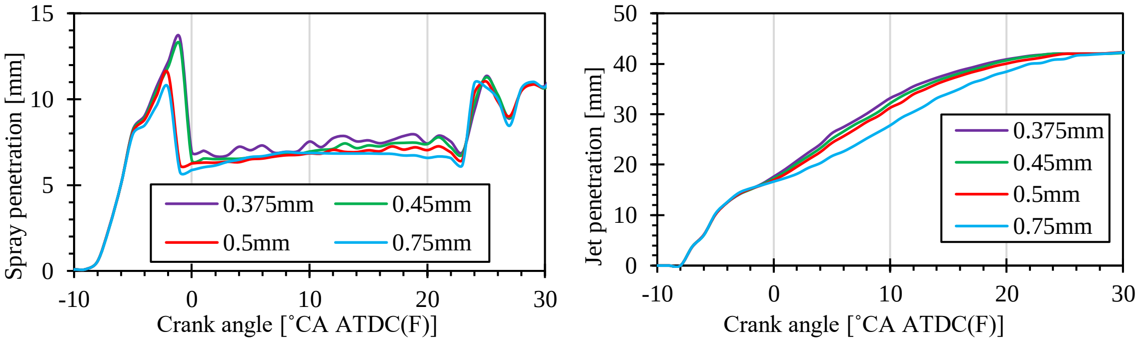

Figure 56: Mesh independence study of the optical engine: spray (left) and jet (right) penetration over crank angle. Selected Mesh: 0.45mm

Time-step independence

The time-step study of the production engine shown in Figure 57. The same time-steps are used as in the optical engine in section 6.2. The steady state spray penetration and the jet penetration are hardly affected by the time-step. A reduction of the time-step until 0.01CAs reduces the initial spray penetration peak significantly. A further decrease of time-step then increases the steady state spray penetration again.

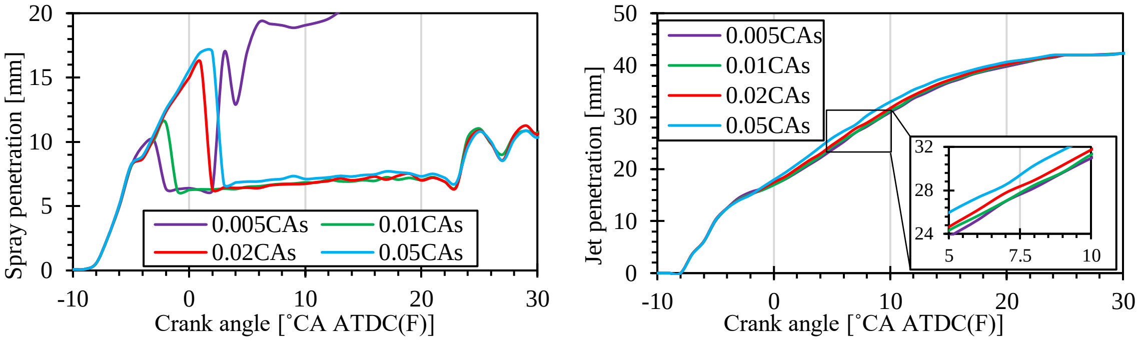

Figure 57: Time-step independence study of production engine - vessel: liquid (left) and vapour (right) penetration over crank angle. Selected time-step: 0.1Cas

A simulation of even smaller time-steps was not possible due to simulation instability. The time-step of 0.01CAs is selected because the initial spray penetration peak is not further reduced significantly, the steady state is barely affected, and the jet penetration is like the other time-step variations.

Parcel introduction rate independence

For the production engine, the same PIR as for optical engine is chosen. This is based on the case with 90K parcels/sec producing a large initial peak in the spray penetration and having a slightly higher jet penetration than all other cases.

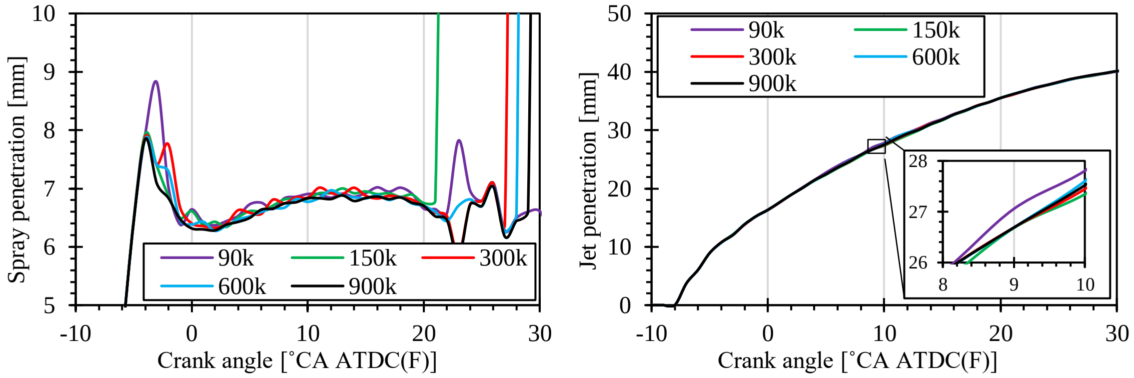

Figure 58: Parcel rate introduction independence study of the production engine: Spray (left) and jet (right) penetration over crank angle. Selected PIR: 150K

Beyond a rate of 150K, no significant change is recorded. The sudden rise of spray penetration at 20 degCA is a numerical artefact that has no impact on the simulation. Tiny droplets with negligible mass break away and penetrate deep into the combustion chamber without affecting combustion.

7 Results and discussion II: Modelling coefficient analysis

The second objective of this thesis is to conduct an extensive investigation into the performance of the modelling coefficients under different operating conditions using a DoE approach (shown schematically in Figure 59).

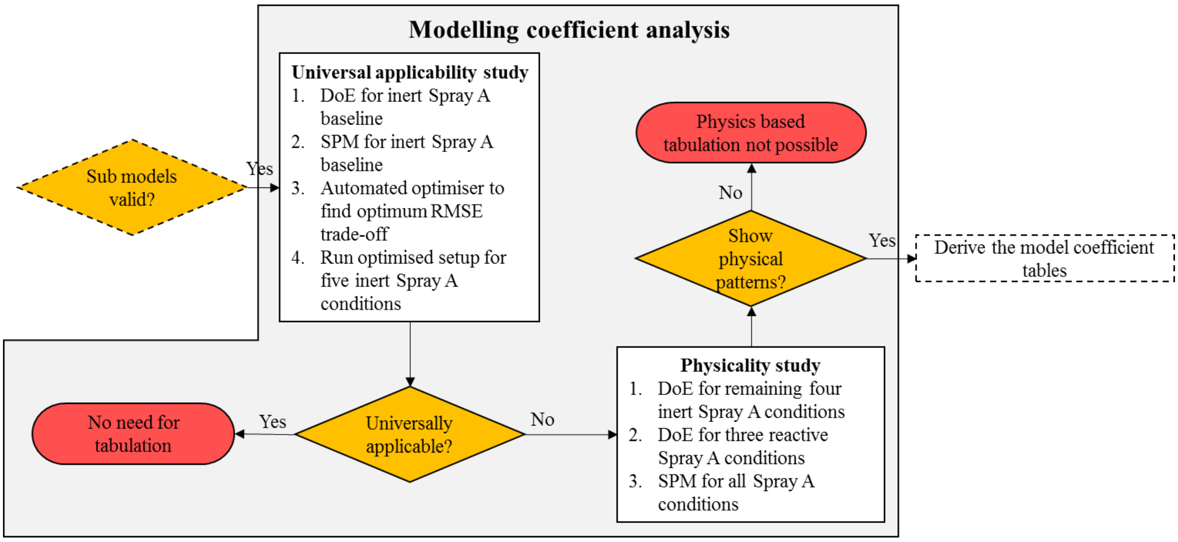

Figure 59: Task flow chart for the modelling coefficient analysis objective

To complete this objective, two research questions must be answered. The first asks whether a single simulation setup can produce reliable results for multiple conditions and is answered by running DoE campaigns for the inert Spray A baseline and producing a SPM. An optimiser is then used to find the modelling coefficients that according to the SPM would produce minimum error between the simulation and the experiment in multiple metrics. These settings are then used to run the simulations for all available inert Spray A key points. Should the results be satisfactory, tabulating modelling coefficient values would not be necessary.

However, this section will show that such a universal setting was not found. The next step therefore to identify the necessary changes to the modelling coefficients and investigate whether there exist links between the mathematical fundamentals and the changing operating conditions (third research question). To do this, further DoE campaigns are performed for a selection of inert and reactive Spray A key points which each represent a swing in boundary conditions. The produced SPMs are then manually analysed for physical patterns that could guide the definition of the modelling coefficients for all remaining Spray A variations. The analysis will focus on potential physical patterns that would greatly improve the predictive nature of the resulting coefficient table.

7.1 Universal applicability study

This section is dedicated to identifying whether a single combination of modelling coefficients can match various inert Spray A operating conditions. A DoE campaign is run for the inert Spray A baseline condition. An optimiser uses produced SPM to identify the combination of modelling coefficients that is predicted to produce the best RMSE trade-off for the available comparison metrics. The found setup is then run for all available inert Spray A conditions. The results in this section were also published in Nsikane *et al* in [168, 169]

7.1.1 Design-of-Experiment for the inert Spray A baseline

One hundred unique combinations of modelling coefficients of the baseline inert Spray A conditions were run with ten DoE variables and then compared to available comparison metrics detailed in Table 11. The detailed list of the DoE variables and their significance is given in Table 2.

Table 11: DoE details for the inert Spray A

Key point	Ambient Temp (K)	Ambient Density (kg/m^3)	Injection Pressure (MPa)	Chamber Pressure (bar)	Number of simulations	Number of DoE variables	Comparison metrics
1	900	22.8	150	6.05	100	10	Spray & jet penetration

7.1.2 SPM for the Spray A baseline

Every simulation is post processed to calculate the RMSE of the comparison metric as shown in (Figure 7). The RMSEs of the comparison metrics are then used to build the SPMs using the quality criteria described in section 2.2.1.5. This includes removing outliers from the model until the desired model quality is achieved. In the context of this task, a detailed description of the SPMs is not yet given but will be discussed later in 7.2.2.

7.1.3 Automated optimisation for inert Spray A baseline

The local optimiser, which is introduced in section 2.2.1.6, is used to find potential simulation settings that match the inert Spray A baseline conditions. For the inert Spray A condition, the spray and jet penetration, are selected as targets (see Table 12).

Table 12: Summary of DoE targets for the two Spray A conditions

Condition	RMSE optimisation targets	Output
Inert Spray A baseline	1. Spray penetration 2. Jet penetration	Pareto curve ~7 solutions

A run with a favourable trade-off between the two RMSEs is then selected. The possible solutions are delivered as a 2D Pareto diagram (e.g. Figure 60). The decision of which point, which represents a set combination of modelling coefficients, to choose is then based on the preferred bias of minimum spray or jet penetration. This setting is then used for all five inert conditions to investigate whether a single simulation setup can produce good results for varying boundary conditions.

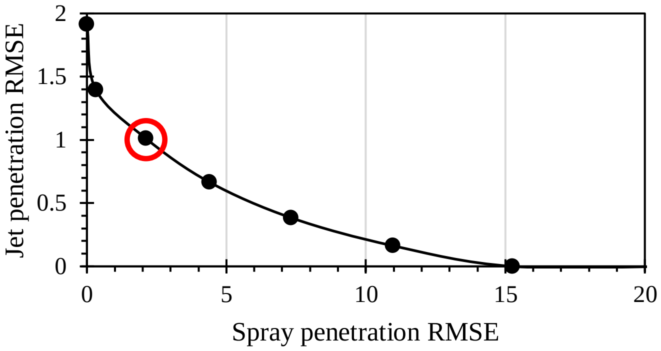

Figure 60: Optimisation using the SPM by minimising the RMSE of spray and jet. The result is a Pareto diagram with multiple possible solutions. Selection circled red.

7.1.4 Run optimised setup for all inert Spray A conditions

The final step is to take the settings from the optimiser of the baseline condition and apply them to all inert Spray A conditions. The results will be shown without much detailed analysis, as at this point the task is a relatively simple feasibility study. A detailed analysis of the simulations and experimental data follows in the section 7.2.

7.1.4.1 Spray Penetration

In Figure 61 shows the comparison between simulated (circles) and experimental (crosses) spray penetration for the inert key points 1-5. The change in ambient density and temperature is shown on the left graph and the discrete injection pressure swing on the right.

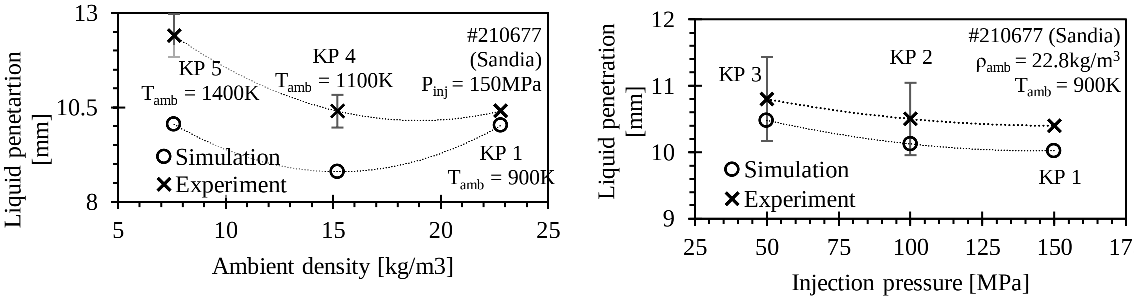

Figure 61: Simulated vs experimental spray penetration under a simultaneous ambient density and temperature swing (left) and a discrete injection pressure swing (right) for key points 1 – 5

For both graphs, a second-order polynomial trend line for both simulation and experiments are added to emphasise the trends. The ambient condition swing (left) shows a qualitatively similar progression but at strongly deviating absolute values for key points 4 and 5. The injection pressure swing shows a very similar progression at a slightly lower absolute value.

7.1.4.2 Droplet size evolution

The match of the spray penetration data for the injection pressure swing introduces an intriguing question. As described in the section 3.1, an increase of injection pressure has a strong effect on the injection dynamics. The spray penetration depends largely on the sizes of the droplets both in the sense of evaporation and aerodynamic effects. Rising injection pressures are thought to either introduce small droplets and/or initiate rapid early stage break-up which results in lower aerodynamic drag (increase spray penetration) but also evaporate faster (shorten spray penetration). The question is therefore: Is the trend in Figure 61 based on an accurate description of the physical droplet sizes evolution or an artefact of coincidental matching?

To answer this, the droplet size evolution of key points 1 and 3 are plotted as a probability distribution functions at three axial locations of the spray in Figure 62. The evolution shows that the droplets of identical initial size shrink faster at lower injection pressures than at higher pressures. This is rather counterintuitive and runs against findings in the literature provided in section 3.1.1.

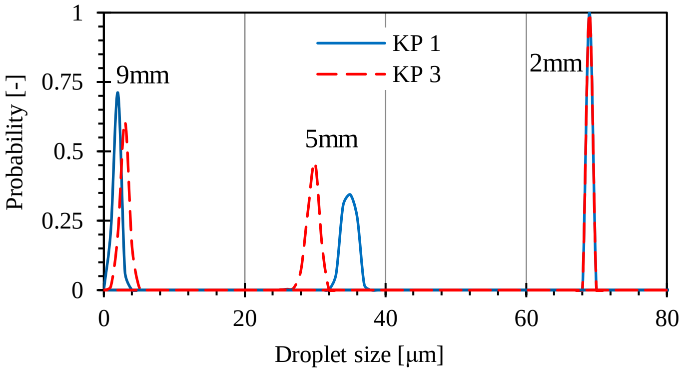

Figure 62: Probability distribution of the droplet sizes of key points 1 (150MPa) and 3 (50MPa) at three axial locations in the spray

7.1.4.3 Jet Penetration

The results of the setup for jet penetrations is shown in Figure 63. The simulation setup (solid line) performs well in capturing both the ambient condition and injection pressure swings shown by the experimental data (dashed line). The discussion of the reasons for the differing penetration rates will be discussed in section 7.2.

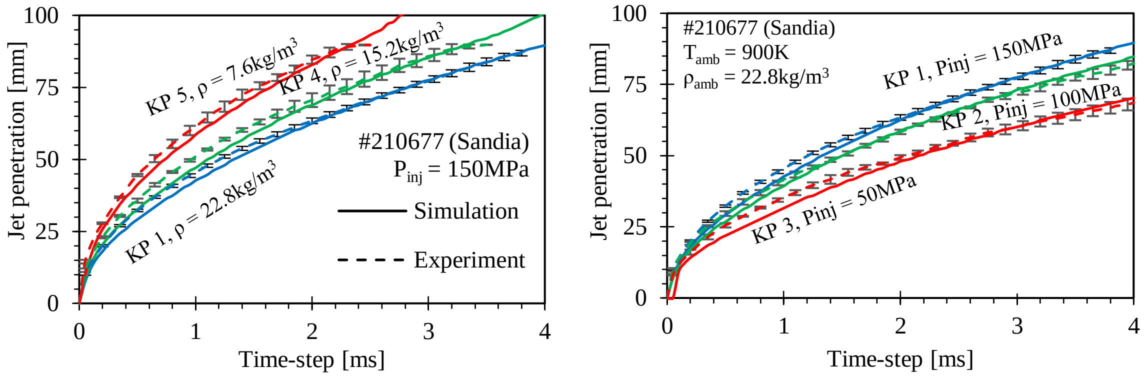

Figure 63: Simulated vs experimental jet penetration under a simultaneous ambient density and temperature swing (left) and a discrete injection pressure swing (right) for key points 1 – 5

7.1.4.4 Mass fraction distributions

The metrics of spray and jet penetration both have the shortcoming that they only show the temporally resolved tip evolution. Available experimental mass fraction distributions allow the comparison of the intermediate radial expansion of the fuel/air mixture. This comparison between simulation (solid blue) and experimental (dashed red) mass fraction distribution at three axial locations of key points 1-4 is shown in Figure 64. No experimental data are offered for KP5 because the high temperature affected the refractive index of the fuel and therefore caused large uncertainties [40]. In all cases, the simulation lies within or near the experimental error.

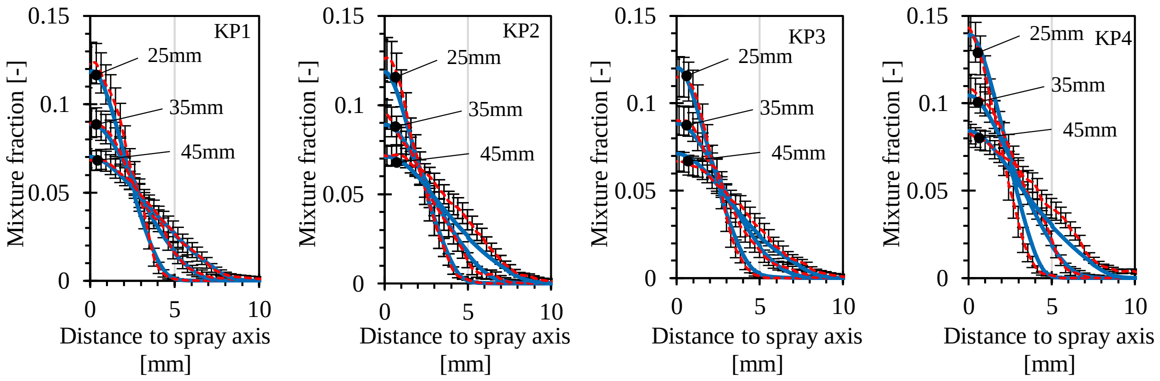

Figure 64: Radial mixture fraction distributions at 25, 35 and 45mm axial distance to the nozzle at a steady state time (at 3.2ms for key points 1-3 and at 4ms for KP 4) and for key points 1-4. No experimental comparison data for KP5 is published. Experiment [40]: red dashed; Simulation: blue solid

In Figure 65 shows the mixture fraction along the spray axis at the same time as before in Figure 64. For all key points, the mixture fraction distribution is well resolved. However, KP4 shows minor deviations that are not evident in the other three cases.

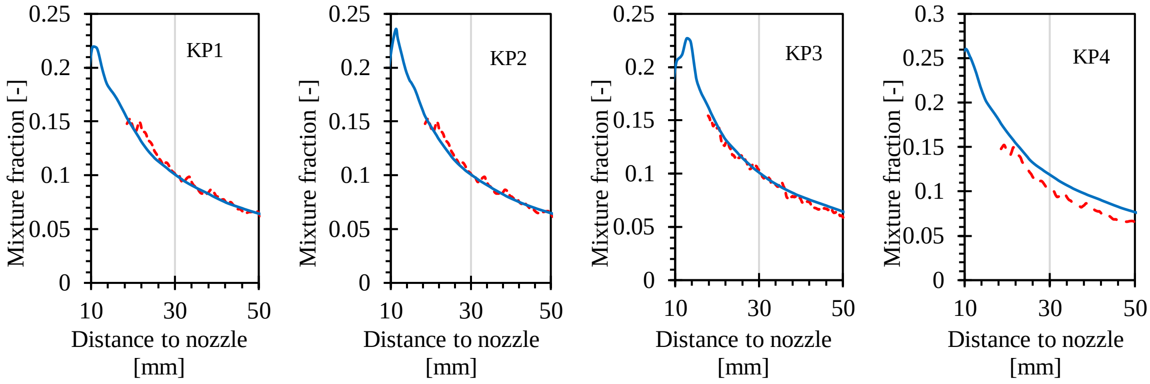

Figure 65: Mixture fraction distributions along the spray axis at a steady state time (at 3.2ms for key points 1-3 and at 4ms for KP 4) and for key points 1-4. No experimental comparison data for KP5 is published. Experiment [40]: red dashed line; Simulation: blue solid line.

7.1.4.5 Ambient temperature distribution

The comparisons between simulated and experimental ambient temperature distributions are shown in Figure 66. Again, data for three axial locations at a given time are provided for key points 1-4. An experimental error margin was not given for this dataset. The three temperature distributions for key points 1 and 3 match the experimental data well. For key points 2 and 4 some disagreement can be seen on the flanks of the 45mm slice. At all key points, the simulated ambient gas is usually slightly hotter than the experiment, indicating that the liquid is not removing enough energy from the surrounding air.

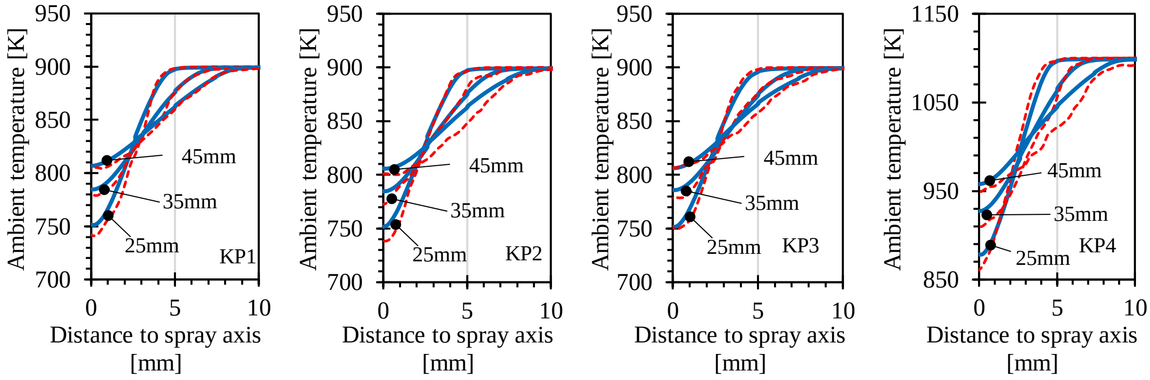

Figure 66: Radial ambient temperature distributions at 25, 35 and 45mm axial distance to the nozzle at a steady state time (at 3.2ms for key points 1-3 and at 4ms for KP 4) and for key points 1-4. No experimental comparison data for KP5 is published. Experiment [40]: red dashed line; Simulation: blue solid line.

7.1.5 Summary of single setup for multiple cases

This section summarises the results of the investigation into the common practice of using a single simulation setup for various parametric variations of experiments. A DoE campaign for the inert baseline Spray A was run and the results used to produce an SPM. An optimiser then offered multiple potential simulation settings based on a trade-off of predicted spray and jet penetration error. The selected simulation setup was then used to simulate five inert Spray A variations. The results were as follows:

1. Both spray and jet penetration are matched well for the baseline Spray A key point. The mass fraction and gas temperature distributions lie within the experimental error where stated.
2. The simulated spray penetration increasingly deviates from the experimental data for the ambient thermodynamic condition swings (KP1, 4 & 5). The trend of the absolute values however is replicated.
3. In the injection pressure swing, both the trend and the absolute values of the simulated spray penetration match the experiments well. A detailed analysis into the droplet size evolution however uncovers a break-up process that cannot be aligned with findings in literature.
4. The simulation of the jet penetration, radial and axial mass fraction distributions and ambient gas temperature distribution at various locations in the spray are mostly within the experimental error for both parametric swings.
5. The reason for the robust and high-quality solutions of the jet penetration is that the optimum value for the coefficients that are most influential for the vapour phase do not change with boundary condition (more about this in the physicality study in section 7.2).

A legitimate argument can be made that the initial simulation setup for the baseline condition that led to the match may just be a combination that happens to match but was not the “right” one to swing the conditions successfully. The counterargument to this is twofold: First, the combined use of the statistical approach with a DoE and an optimiser based on the SPM significantly increases the confidence in the found “best setup”. Secondly, there exist too many possible combinations of available modelling approaches, their sub models and their coefficients for CFD analysts to identify that “right” one manually. Perhaps there exists a simulation setting that performs better under swinging conditions but until that setting is found, holding simulation coefficients at varying boundary conditions is unlikely lead to successful matches for a range of conditions. Considering that simulated case in this section is an experiment under simplified hardware (CV – chamber) and inert conditions, the chances of finding a universally applicable settings for complex engine operation are even smaller.

7.2 Physicality study

With the conclusion of the previous section discouraging the use of a single setup for a range of boundary conditions, the focus of this section lies on the process of identifying individual simulation setups that can produce good results for all Spray A cases. Individual DoE campaigns for the eight Spray A cases are performed and the produced SPMs analysed for any patterns shown by the modelling coefficients that could be used to match changing boundary conditions. The results from the inert conditions in this section were first published in Nsikane *et al* [15], and then improved and expanded in Nsikane *et al* in [16] . The detailed discussion of the reactive cases is at the point of submission under peer review.

7.2.1 Design-of-Experiment for all Spray A conditions

One hundred unique combinations of modelling coefficients of the five inert Spray A conditions were run with each ten DoE variables and then compared to available comparison metrics detailed in Table 13.

Table 13: DoE key points for the physicality study

Key point	Ambient Temp (K)	Ambient Density (kg/m^3)	Injection Pressure (MPa)	Chamber Pressure (bar)	Number of simulations per key point	Number of DoE variables	Comparison metrics
1	900	22.8	150	6.05	100	10	Spray & jet penetration
2			100				
3			50				
4	1100	15.2	150	4.96			
5	1400	7.6		3.19			
7	800	22.8	150	5.3	140	14	Spray & jet penetration, LoL & RoHR
9	900			5.9			
18	1200			7.9			

Additionally, 140 simulations with 14 DoE variables were run for the reactive Spray A condition. The detailed list of the DoE variables and their significance is given in Table 2.

7.2.2 Stochastic process modelling

Every simulation is post processed to calculate the RMSE of the comparison metric as shown in 0. The RMSEs of the comparison metrics are then used to build the SPMs following the quality criteria described in section 2.2.1.5. The detailed analysis of the SPMs will be given separately for inert and reactive Spray A conditions. Within this separation, the SPMs will be further analysed for the individual comparison metrics from Table 13 to highlight the effects of the modelling coefficients.

7.2.2.1 Inert Spray A

Figures 67 and 68 show the SPM's for the key points 1-5. The significance of the coefficients on the x-axis are explained in Table 2. Each field in the rows represent the RMSE between the experiments and simulations as a function of the modelling coefficient in the column. The x-axis (which indicates the coefficient value) was removed from the columns for confidentiality reasons. This does not obstruct the qualitative nature of the graph. The gradient represents the sensitivity of the RMSE towards a change of that modelling coefficient. The dotted lines represent 2σ confidence of the prediction.

Spray Penetration

Th red box in Figure 67 shows the two most influential modelling coefficients for the inert Spray A cases. The level of influence of a coefficient is indicated qualitatively by the curvature of the RMSE curve over coefficient value. The first one is the drag scaling coefficient A_{drag} and the second is the KH – B_1 coefficient. The remaining eight modelling coefficients do not show strong sensitivities.

The drag scaling coefficient A_{drag}, which influences the liquid/gas momentum transfer, is crucial for liquid and to some extent jet penetration. For key points 1-4, it is assumed there is a minimum beyond the investigated range, leaving merit to extend the ranges in future work. However, not including the minima's does not hinder the results because the trade-off required to keep vapour RMSE low requires selecting a value within the range. The steep inclinations of the RMSE curves and different value for each condition highlight the condition sensitivity of this parameter. Generally, a reduction of RMSE sensitivity with decreasing density can be observed (compare absolute maximum liquid RMSE between KP 1, 4 & 5). Additionally, key point 5 (1400K, 7.6kg/m3, 150MPa) shows a clear increase for required absolute coefficient value.

The KH – B_1 coefficient, which influences the primary break-up time scale, is also paramount for liquid length calculations. However, unlike the characteristics of the drag scaling coefficient, KH – B_1 shows its minimum at approximately the same axial location and similar absolute RMSE sensitive at all key points. This means that although KH – B_1 is an influential parameter, the variations of the absolute value between conditions are small and therefore justify the parameter to be held constant across key points.

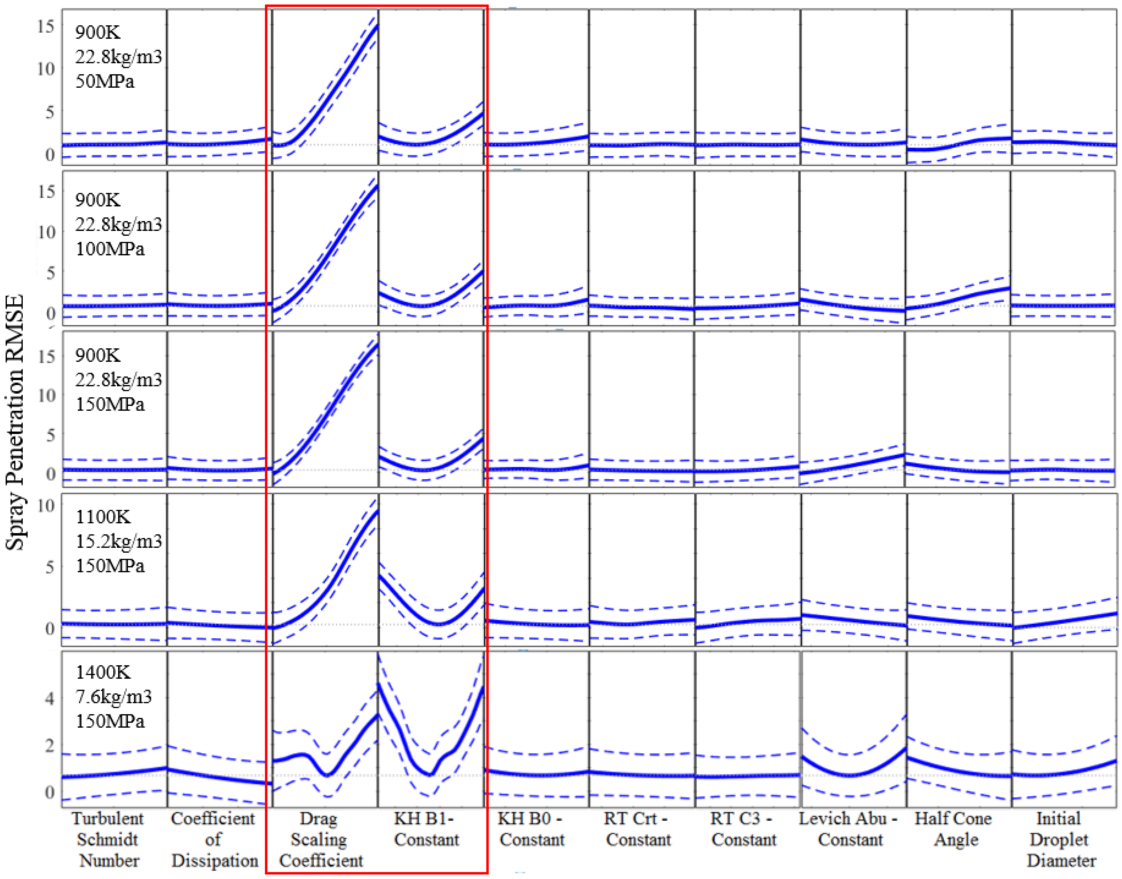

Figure 67: Graphical representation of the SPM that highlights sensitivities of the RMSE of the jet penetration (rows) on a change of modelling coefficient value (columns) for the DoE key points. The dashed lines represent the 2σ confidence range.

Jet Penetration

In Figure 68, the coefficient of dissipation C_2 shows to have a significant impact on the jet penetration and only little on the spray penetration. The C_2-coefficient is the single most influential parameter to adjust the jet penetration. It also shows a clear minimum, which indicates that there is only a small range in which it may vary. The axial location of this minimum, which represents the coefficient’s value, does not vary with operating condition.

This is not to say that they are not important as they do affect the microscopic characteristic of the spray plume. For example, SPMs on reactive cases show initial droplet sizes and the RT C_3 – coefficient to be influential for secondary break-up, which influence combustion characteristics for combusting cases. Given some quantitative droplet size measurements at any location of the spray plume, an additional target metric for the DoE could increase accuracy of the response of the simulation coefficients that are more influential for microscopic spray characteristics. While not influential here, the turbulent Schmidt number was shown to become more influential under realistic engine conditions with swirl motion and fuel injection through a multi-hole injector.

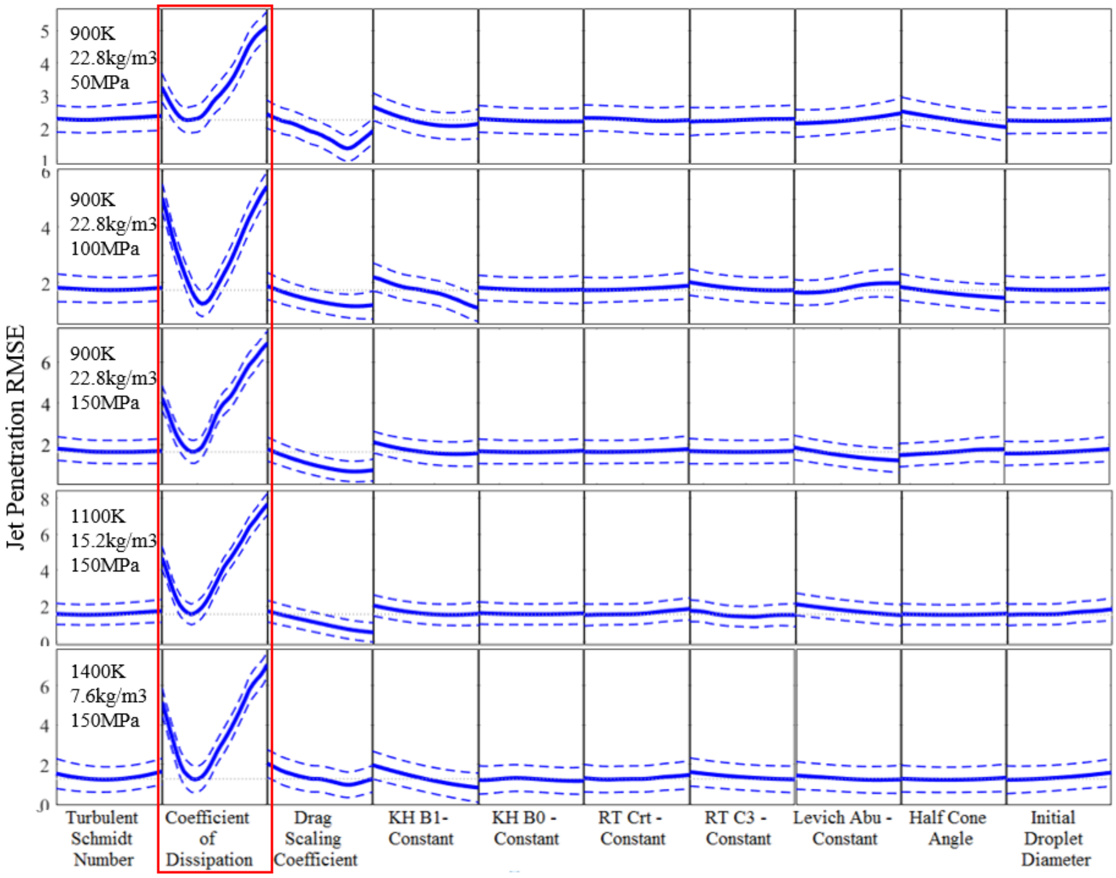

Figure 68: Graphical representation of the SPM that highlights sensitivities of the RMSE of the jet penetration (rows) on a change of modelling coefficient value (columns) for the DoE key points. The dashed lines represent the 2σ confidence range.

7.2.2.2 Reactive Spray A

A graphical representation of the SPMs of the DoE key points for the reactive cases is shown in figures 69-72. The significance of the coefficients on the x-axis are explained in Table 2. Each field in the rows represent the RMSE between the experiments and simulations as a function of the modelling coefficient in the column. The x-axis with the coefficient values in the column were removed for confidentiality reason, however this does not obstruct the qualitative nature of the graphs.

Spray Penetration

The spray penetration for these reactive key points has not been measured by the ECN but work by Pickett *et al* in [45] suggests that a comparison to inert spray penetrations is justified due to the negligible effect downstream combustion has on the absolute value. The spray penetration RMSE shown in Figure 69 is predominantly influenced by drag scaling coefficient A_{drag} and the break-up model's KH - B_1. The turbulence dissipation coefficient C_2 and the initial cone angle α_{cone} show increased sensitivity, with their optimum value resting on the higher end of the range.

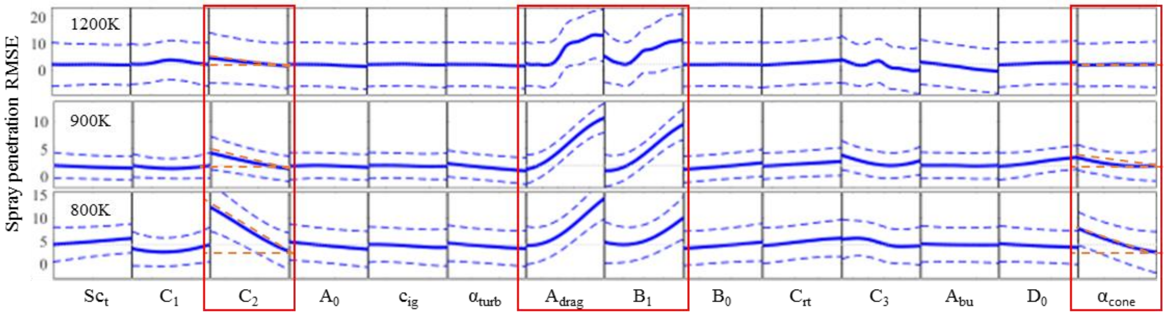

Figure 69: Graphical representation of the SPM that highlights sensitivities of the RMSE of the spray penetration (rows) on a change of modelling coefficient value (columns) for the DoE key points. The dashed lines represent the 2σ confidence range.

Unlike in the ambient temperature and density swing under inert conditions discussed earlier, the axial location of the minimum of A_{drag} remains unchanged at the lower end of the range. The strong sensitivity shown in the inert conditions can therefore be clearly associated with the changing ambient density.

The axial variation of the minimum of KH-B_1 is small despite such a large ambient temperature variation. This confirms the findings from the inert conditions that this coefficient may remain unchanged across a range of thermodynamic conditions.

At lower ambient temperatures, the C_2 coefficient and the cone angle also become more influential (orange dashes). At colder conditions, when thermal effects reduce and the turbulent mixing becomes the dominating effect breaking up the droplets (shown experimentally by Siebers [13] and Naber *et al* [41]), changing C_2 and the cone angle has a big effect on the spray penetration. However, a selection at the higher end of the range is applicable for all three conditions making a tabulation for this condition swing obsolete.

Flame lift-off-length

The RMSE of the flame lift-off in Figure 70 shows three main sensitivities. The first is a dependency on the auto-ignition coefficient c_{ig}, the second shows a trend for the KH-B_1 coefficient and finally an increasing sensitivity of the RT-C_3 coefficient with rising temperatures.

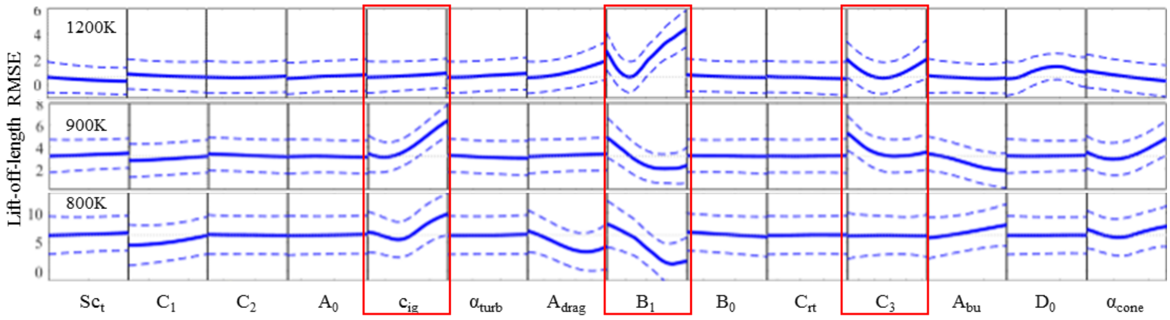

Figure 70: Graphical representation of the SPM that highlights sensitivities of the RMSE of the LoL (rows) on a change of modelling coefficient value (columns) for the DoE key points. The dashed lines represent the 2σ confidence range.

With increasing ambient temperatures, the auto-ignition coefficient c_{ig} becomes less influential (see RMSE scale). In addition, the optimal value (minimum) varies from 800K to 900K. The c_{ig} coefficient linearly scales the chemical ignition delay. When this chemical ignition delay becomes very small at increasing temperatures, the scaling of it has a negligible effect on the SoC.

The KH-B_1 value also influences the LoL. A shifting of the axial location of the minimum from right to left is visible with increasing temperature. The spray penetration and LoL are directly linked to each other in way that their trends follow the same progression in a temperature swing (see Siebers and Higgins [49]). However, the absolute value of spray penetration length is not as sensitive as the lift-off length. An adjustment of B_1 would lead to much stronger spray penetration variations than were measured under inert conditions. For this reason, a single value is chosen as a trade-off that can produce acceptable results for both metrics as defined in section 1.4.2.

Another observation is an increasing influence of the RT-C_3 coefficient with increasing temperature at nearly unchanged axial position of the minimum. The cause of this rising influence is speculated to be related to the high temperature case approaching the trans-critical regime (see Crua *et al* [28]). Why the effect on the RMSE is not visible for the spray penetration may have to do with the microscopic processes influencing the LoL but are not considered when looking at macroscopic spray penetration lengths. More research is necessary to determine if this path of reasoning has merit.

Jet Penetration

For the RMSE of the jet penetration (see Figure 71), like in the inert cases, the turbulence dissipation coefficients are of main importance. The C_2 coefficient converges clearly at a minimum that is the same for all three temperatures. The sensitivity is so strong that the selection of these two coefficients for the setup is almost solely based on this minimum. A minimum for C_1 is not visible, which indicates the DoE range should be expanded in future work.

The transition from inert to reactive spray requires an increase of the C_1 and C_2 coefficients in the standard k-ε model turbulence model to adjust for combustion induced turbulence [46]. For the inert conditions, C_2 was shown to have a significantly lower optimum value. The C_1 coefficient was not included in the DoE coefficient matrix of the inert conditions and was left at default. Like in the inert cases, once the value for C_2 is found, it can remain constant across conditions.

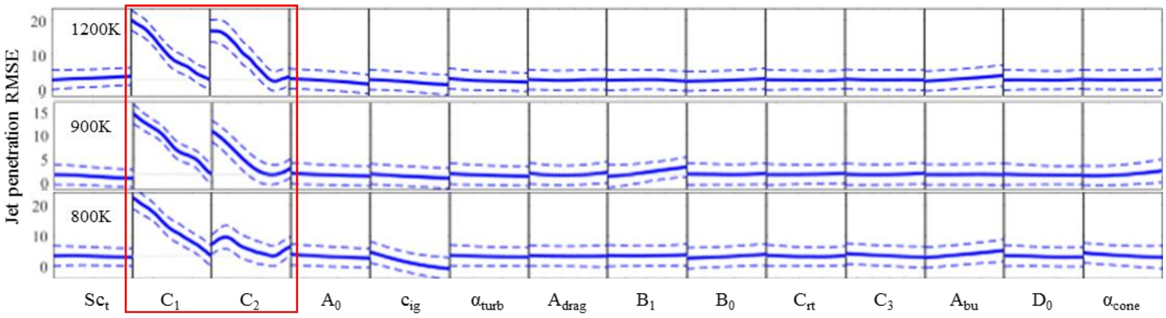

Figure 71: Graphical representation of the SPM that highlights sensitivities of the RMSE of the jet penetration (rows) on a change of modelling coefficient value (columns) for the DoE key points. The dashed lines represent the 2σ confidence range.

Total heat release

The error of the total heat release shown in Figure 72 appears to be controlled mainly by the turbulence coefficients and the turbulent flame speed multiplier. This is expected because turbulence mixing is one of the controlling factors of heat released during combustion. The reason the turbulent flame speed multiplier becomes important is because Spray A is a partially premixed rather than a pure non-premixed flame (see Pei *et al* [72]).

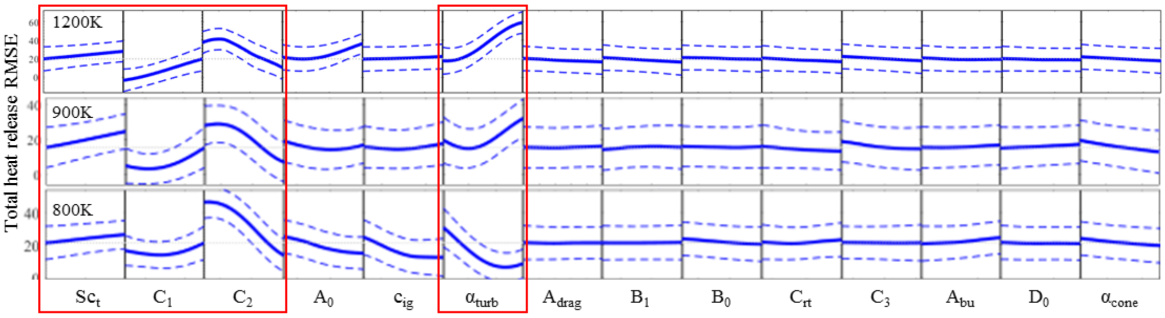

Figure 72: Graphical representation of the SPM that highlights sensitivities of the RMSE of the jet penetration (rows) on a change of modelling coefficient value (columns) for the DoE key points (800K, bottom, 900K, middle, 1200K, top). The dashed lines represent the 2σ confidence range.

In Siebers and Higgins [49] it is mentioned that the flame speeds are thought to accelerate with increasing ambient temperatures. The requirement to reduce the α_{turb} coefficient with increase temperature indicates that the Gülder model would otherwise overestimate the turbulent flame speed.

7.2.2.3 Summary of the stochastic process models

After running the DoE campaigns for the eight selected key points, individual SPMs are produced and analysed for characteristic patterns of the modelling coefficient's effect on the simulated result. The findings are separated in the same way their results were sectioned to highlight the different sensitivities.

Initial conditions

This section is to summarise the predicted effect of the initial conditions, i.e. the initial spray half cone angle α_{cone} and the initial droplet sizes D_0 on the comparison metrics. The results regarding α_{cone} are as follows:

1. At lower ambient temperatures of the reactive Spray A condition, the RMSE of the spray penetration becomes more sensitive to the cone angle.
2. This is explained physically by the turbulent mixing becoming the dominating effect breaking up the droplets that was shown experimentally by Siebers [13] and Naber *et al* [41]. Nonetheless, no tabulation is required because a single value at the higher end of the range is suitable for all ambient temperature conditions.

Running the simulations with the values derived from these SPMs produced good results but also highlighted a sensitivity was been missed in the SPMs. Despite the RMSE of spray penetration and flame lift-off not showing any strong sensitivity toward the initial droplet sizes, a dependency was later discovered. Leaning on the Patterson-Reitz initial droplet sizes correlation, a change of droplet sizes depending on the boundary conditions was derived. The summary of the behaviour of the initial droplet sizes is given as follows:

1. With increasing ambient density at constant temperature (compensated by chamber pressure) and injection pressure, a necessary decrease in initial droplet sizes is noticed. These changes of droplet sizes cannot solely be attributed to nozzle dynamics because the difference in pressure drop between these cases ranges only between 144 and 148MPa.

2. The impact of gas density on a droplet is instead linked to the Weber number, which increases with a rise in density. This makes the droplet more unstable and easier to break-up [24].
3. The initial droplet sizes are set to decrease as the injection pressure increases. This is in line with findings by Crua *et al* in [131] where with an increasing injection velocity the droplet break-up becomes more rapid as shear forces become stronger.
4. The initial droplet sizes are expectedly insensitive to ambient temperature swings. Although higher evaporation rates play a role, they are negligible in comparison to the aerodynamic effects of density or injection pressure changes. For this reason, temperature sensitive tabulation is not necessary for these two modelling coefficients

An argument can be made that the droplet size evolution should be adjusted using the spray model coefficients rather than using the initial droplet sizes. This may be to an extent true, but there is not enough conclusive experimental data with which a spray model can be calibrated. By using the initial droplet sizes, the main parametric condition variations are accounted for and the complex spray models can remain untouched. This reduces the number of variable coefficients from five to one. Despite this, a further investigation in the area of spray modelling certainly has merit.

Spray modelling

The KH-RT break-up model can, without being altered, accurately simulate droplet break-up and evaporation under the assumption that the initially introduced droplet diameters are adjusted to the boundary condition. Besides this, three major findings regarding the coefficients of the spray model are:

1. The SPMs of all conditions confirm the known sensitivity of spray and jet penetration towards a change KH-B_1. The distinct minima, which represent low RMSE's, settles for the similar value regardless of boundary condition. This suggests that although the simulation is highly sensitive to this coefficient, once its optimal value is found, it may remain unchanged for other operating conditions.
2. An increasing influence of the RT-C_3 coefficient with increasing temperature at nearly unchanged axial position of the minimum is noticed. The cause of this rising influence is speculated to be connected to the high temperature case approaching the trans-critical regime

3. The remaining KH-RT model coefficients B_0, C_{RT} and A_{bu} show negligible sensitivities in comparison to the others. This means their selected values (which is not default) may remain unchanged regardless of boundary condition.

The drag scaling coefficient A_{drag} introduces the necessary flexibility of the effects of droplet deformation in the Putnam drag model, which assumes that all droplets are spherical. The conclusions are:

1. The drag scaling coefficient A_{drag} indicates that with increasing injection pressures the droplets become increasingly deformed. This is a characteristic found within droplets exposed to high sheer due to increased relative injection velocities.
2. When increasing ambient densities, an increase of aerodynamic effects can be expected. This is thought to deform the droplets stronger, which is also supported by the decrease of the coefficient with increasing density.
3. The drag scaling coefficient A_{drag} is not expected to require adjustment for ambient temperature changes. This is confirmed in the SPMs where the optimum coefficient value remains the same for a swing in ambient temperature.

Gas phase modelling

The coefficients C_1 and C_2 in the standard k-ε model are responsible for scaling the dissipation rate of the turbulent kinetic energy. A higher C_2 increases dissipating effects and consequently increases the diffusion of the gas phase while C_1 scales the generation rate of turbulence energy. The results derived from the SPMs are:

1. Two of the dominating modelling coefficients for simulating the gas phase and to smaller extent the liquid phase are the turbulence coefficients C_1 and C_2. Their value may remain unchanged for all conditions.
2. A direct transfer of the turbulence coefficients from inert to reactive cases is not possible. Under reacting conditions, the turbulence coefficients must be raised to account for combustion-induced turbulence.

The turbulent Schmidt number Sc_t is responsible for adjusting the intensity of the heat release by shifting the ratio of viscous diffusion rate to molecular diffusion rate.

1. Initial analysis of the SPMs indicated a small influence of Sc_t. When running the engine conditions, it was later discovered that Sc_t had to be strongly reduced to match pressure rise and heat release characteristics.

2. The revision of the SPMs then highlighted that the simulations are not as insensitive as initially thought, but rather the range of investigated Sc_t was too small with the ideal value likely being lower than the lower end of the defined range.

A tabulation of the turbulence coefficients is only necessary when changes to the turbulence levels in the conditions are present. This means significant changes to the setup like a transition from inert to reactive, from single hole to multi-hole or from no swirl-to-swirl. A tabulation of these aspects may be difficult but is feasible. A tabulation for changing thermodynamic boundary conditions and injection pressure however is not necessary.

Combustion modelling

To replicate the combustion characteristics, the SPMs showed the auto-ignition coefficient c_{ig} and turbulent flame speed multiplier α_{turb} to be the influential modelling coefficients. A swing of the turbulent flame speed multiplier showed some effect, however to such a small extent that a tabulation of this coefficient would not be necessary. The sensitivity of the simulation results to the auto-ignition coefficient on the other hand were significant. It links the complexity of the fuel specific ignition delay process with the simplistic Livengood-Wu auto-ignition model.

1. This c_{ig} coefficient shows strong sensitivities for thermodynamic boundary condition swings. Its influence however declines sharply with increasing ambient densities and temperature (shortening ignition delays). It may remain unchanged under a changing injection pressure.

The sensitivity of the simulations to this coefficient complicates the adaptation to other fuels like EU reference Diesel, as a fuel specific tabulation would be required. However, should an extensive database such as for Spray A exist for a range of fuels, this could be a solvable problem. Additional work could also identify to which extent the chemical composition of fuels affects this coefficient.

The burn velocity coefficient A_0 linearly scales the reaction rate of the mixture. The reaction rate of diffusion flames is fast comparing to the mixing rates. Therefore, scaling the reaction rate is less influential. This effect is indicated with a relatively flat RMSE response to A_0, which also means that the value can be held unchanged across boundary conditions changes.

7.2.3 Performance of simulations settings derived from the SPM

This section is dedicated to discussing the results of running the simulations of the inert and reactive Spray A variations with the modelling coefficients derived from the SPMs in the previous sections. The results are again separately discussed based on the reactivity of the condition.

7.2.3.1 Inert Spray A

Droplet size evolutions

The droplet size evolution of key points 1 and 3 are shown in Figure 73. The droplets that are introduced based on using the Patterson-Reitz initial droplet size correlation suggests the initial droplet size of the lower injection pressure case should be larger. Unlike in the case of the identical droplet sizes being introduced (see Figure 62), the droplets of the higher injection pressure case are always smaller than their low-pressure counterpart. The macroscopic liquid length is thought to be predominantly affected by air entrainment (or turbulent mixing)[13, 41]. As the injection rate increases, so does the turbulent mixing, which continues to deliver energy that can break-up the droplets around the same axial location.

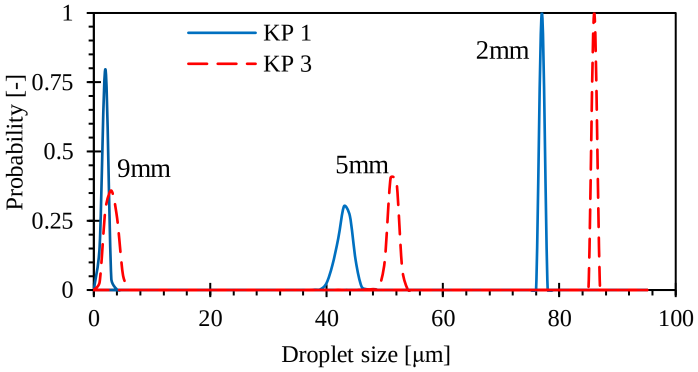

Figure 73: Probability distribution of the droplet sizes of key points 1 (150MPa) and 3 (50MPa) at three axial locations in the spray

Spray penetration

In the case of an isolated ambient temperature increase, it is assumed the spray penetration would decrease with increasing ambient temperature due to increased droplet evaporation. Vice-versa, an isolated decrease of chamber density would increase spray penetration [41]. When these two effects happen simultaneously, the effects partially counteract each other until one of the effects becomes dominant. The authors see strong indication of this phenomena occurring in the cases shown Figure 74. As the ambient temperature increases and ambient density inversely decreases from KP1 to 4, the spray penetration decreases slightly. This decrease is due to the increased evaporation rate outweighing the aerodynamic effects. When this progression continues to KP5, the spray penetration increases strongly. It is suggested that while between KP1 and 4 the temperature influence is slightly stronger, aerodynamic effects become dominant between K 4 and 5.

Figure 74 shows a comparison between the simulation setup derived from the SPM and the ECN test data of spray penetration length over ambient density. The simulation settings produce average liquid lengths within the supplied error bands and evidently follow the trends of the experimental data. For KP1 no experimental error in the spray penetration is stated, however is not expected to be significantly different to other cases.

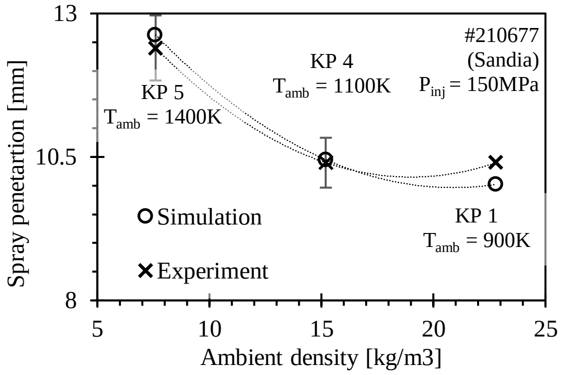

Figure 74: Simulated vs experimental spray penetration under a simultaneous ambient density and temperature swing (left) for key points 1, 4 & 5)

The experimental data show that spray penetration decreases only slightly with increasing injection pressure (see Figure 75). The microscopic processes of the break-up, however, change with increasing injection pressures. Crua *et al* in [131] shows that the initial stages of injection are different between injection pressures. He shows that at low injection pressures, surface tension is strong which allows slow but large droplet ligaments to be introduced. At higher injection pressures, break-up forces exceed surface tension and fast and small droplet-like ligaments exit the nozzle. Since the injection rate and velocities are reduced at lower pressures, less inertia is passed onto the vapour phase resulting in their slower progression (more to this in the next section).

The spray penetration of the refined setup shows good average spray penetrations for all three conditions and a comparable response of the absolute value to increasing injection pressures. The trend and the absolute values are comparable to the findings from the universal applicability study (see Figure 62), but the key difference is that now the droplet shrinking follows a more physically sensible process (see Figure 73).

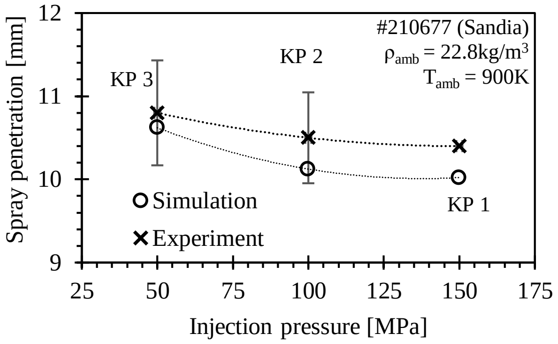

Figure 75: Simulated vs experimental spray penetration for a discrete injection pressure swing for key points 1-3

Jet Penetration

The jet penetration shows a clear sensitivity to reducing chamber density, presumably due to reduced aerodynamic resistance resulting in less mixing. An isolated temperature increase under constant density is not thought to have much effect on the vapour motion. The overall smaller RMSE range for jet penetration means the setup is more robust to changes of even the most sensitive modelling coefficient. The temporal jet tip evolution is well captured at all three conditions, however, show some deviation between 0.5 and 1.5ms.

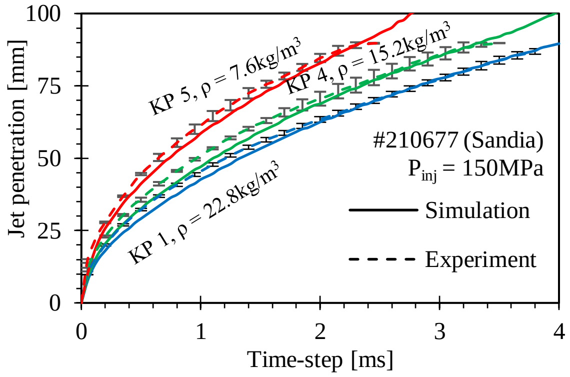

Figure 76: Simulated vs experimental jet penetration under a simultaneous ambient density and temperature swing for key points 1, 4 and 5

The experimental data show that while the spray penetration (see Figure 75) only slightly decreases with increasing injection pressure, the jet penetration (see Figure 77) rises significantly, deeming the liquid/gas phase momentum transfer an influential process.

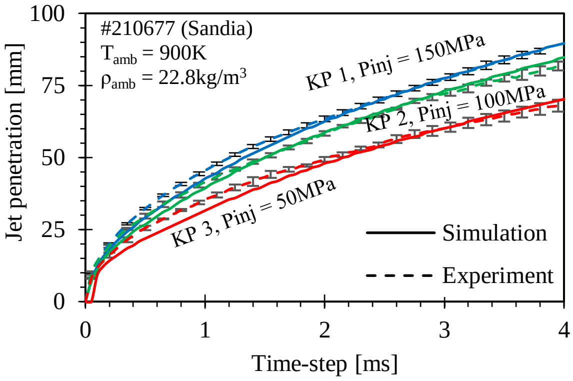

Figure 77: Simulated vs experimental jet penetration at a discrete injection pressure swing for key points 1-3

To increase confidence in the simulated mixture preparation, the radial mass fraction distributions at three plume cross sections and axial mass fraction along the centreline of the plume are compared to available experimental data captured at a steady state time interval.

Mass fraction distributions

The results of the simulations are shown in Figure 78. In all metrics, the simulations perform well and, where available, lie within or near the stated experimental error. No mass fraction and temperature measurements were taken for the 1400K key point (KP 5) because of increasing measurement uncertainties due to the experimentally challenging in-cylinder conditions.

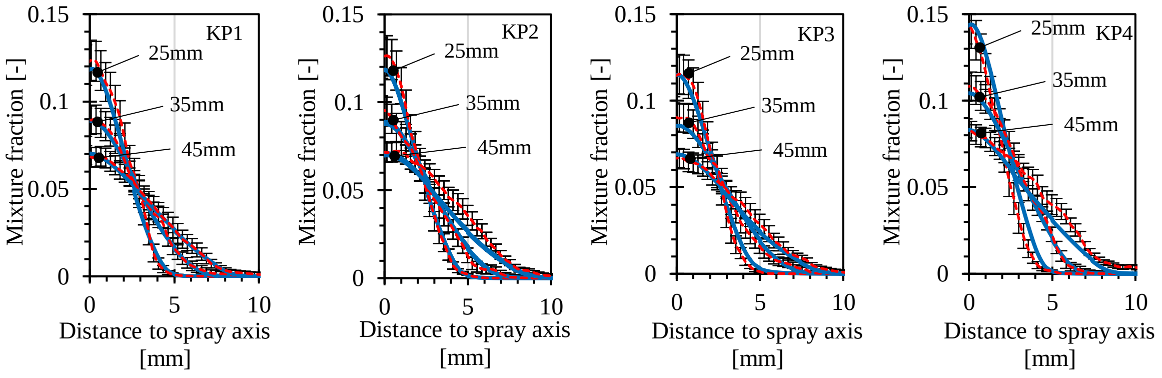

Figure 78: Radial mixture fraction distributions at 25, 35 and 45mm axial distance to the nozzle at a steady state time (at 3.2ms for key points 1-3 and at 4ms for KP 4) and for key points 1-4. No experimental comparison data for KP5 is published. Experiment [40]: red dashed line; Simulation: blue solid line.

The mixture fractions along the spray axis shown in Figure 79 are well captured for key points 1-3. Like in Figure 64, KP4 shows slight deviation from the experimental data. The reason that this metric has not improved despite case specific modelling coefficients is that the vapour phase is less susceptible to varying modelling coefficient and mainly relies on the turbulence coefficients. These coefficients have remained unchanged between the universal applicability study and the targeted selection method.

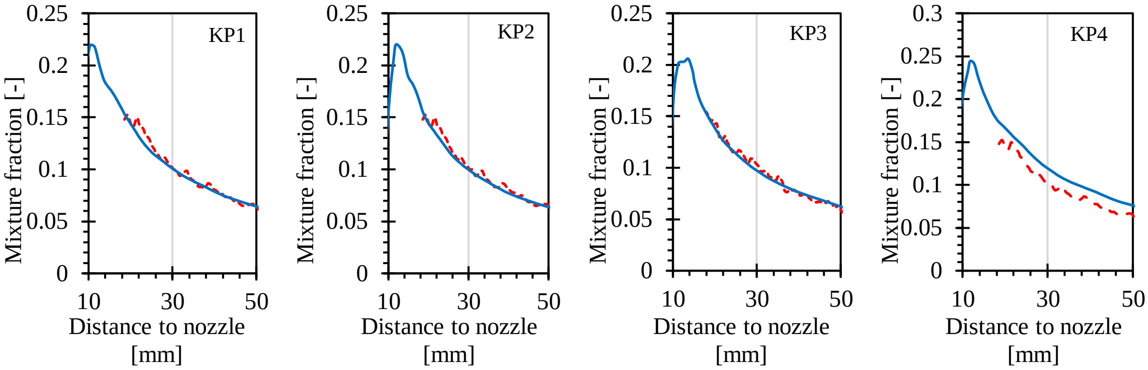

Figure 79: Mixture fraction distributions along the spray axis at a steady state time (at 3.2ms for key points 1-3 and at 4ms for KP 4) and for key points 1-4. No experimental comparison data for KP5 is published. Experiment [40]: red dashed line; Simulation: blue solid line.

Ambient temperature distributions

The ambient gas temperatures are of similar quality as previously shown in section 7.2.2.1, where the setup remained unchanged. An experimental error margin was not given for this dataset. The three temperature distributions for key points 1 and 3 match the experimental data well. For key points 2 and 4 some disagreement can be seen on the flanks of the 45mm slice. At all key points, the simulated ambient gas is usually slightly hotter than its measured counterpart is.

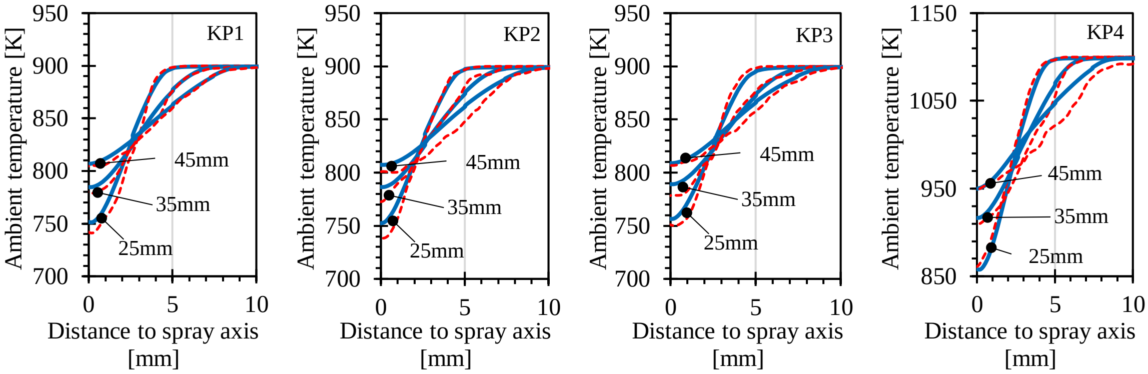

Figure 80: Radial ambient temperature distributions at 25, 35 and 45mm axial distance to the nozzle at a steady state time (at 3.2ms for key points 1-3 and at 4ms for KP 4) and for key points 1-4. No experimental comparison data for KP5 is published. Experiment [40]: red dashed line; Simulation: blue solid line.

7.2.3.2 Reactive Spray A

Droplet size evolution

Although droplet sizes were not measured for the reference conditions, they give a good indication of the how physically representative the derived setup is. The well-known decrease in spray penetration with increasing ambient temperature is mainly due to accelerated droplet heating as described by Naber in [41]. It is therefore expected that for the hotter condition the droplets evaporate earlier. This behaviour is captured well by the three simulation setups shown in Figure 81. The droplet size evolution is shown in form of multiple probability distribution functions at various nozzle distances. After the droplets leave the nozzle with the same size, the hotter environment shows its effect ~6mm downstream the nozzle. From there onward, the probability of smaller droplets increases sharply for the high temperature condition.

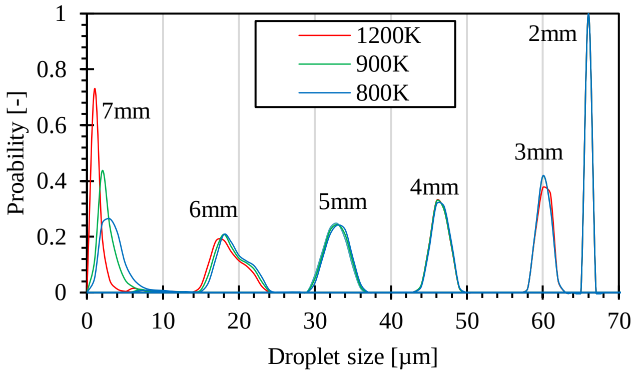

Figure 81: Droplet sizes probability distributions at given locations of the spray axis for three ambient temperature conditions

Initial droplet sizes, which depend mostly on orifice pressure drop and ambient densities [19, 131], and deformation are not expected to vary in an ambient temperature swing. Therefore, the initial droplet diameters and the droplet may remain unchanged.

Spray Penetration

In Figure 82 the time-averaged values for spray penetration are plotted as a function of ambient temperature. The data points are marked as crosses for experiments and squares for the simulations. The spray penetration for these reactive key points has not been measured by the ECN but work by Pickett *et al* in [45] suggests that a comparison to inert spray penetrations is justified due to the negligible effect downstream combustion has on the absolute value.

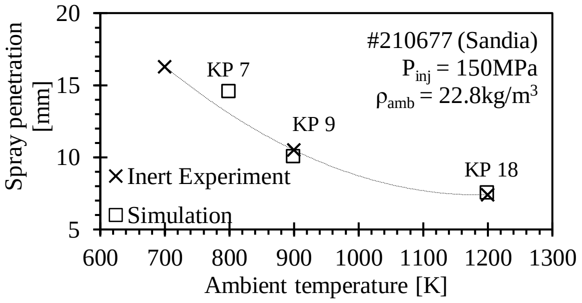

Figure 82: Comparison between DoE optimised simulated spray penetration against experimental ECN data at constant injection pressure and ambient density conditions. Note that the spray penetration data are sourced from inert operating conditions and only serves a qualitative comparison [122]

The simulation, which is derived from the SPMs performs well in replicating the experimental trend. Since all relevant modelling coefficients remain unchanged, it can be concluded that the decrease in spray penetration is brought about by increasing droplet evaporation.

Lift-off length

The definitions of LoL between the simulations and the experiments differ in the sense that the experimental LoL is derived from OH concentrations at the early stage of combustion and simulations rely on a numerical combustion progress variable. Therefore, while the absolute values of LoL are not directly comparable, the trends between key points are clear and of paramount importance. The effect the ambient temperature has on the LoL is described in Siebers and Higgins [49]. Figure 83 shows a clear non-linear decrease in LoL with increasing ambient temperature. The reasons for this are straightforward. The hotter air accelerates chemical conversion rates, which advances the spatial SoC towards the nozzle. The trend of the lift off length is well reproduced by the simulation setup.

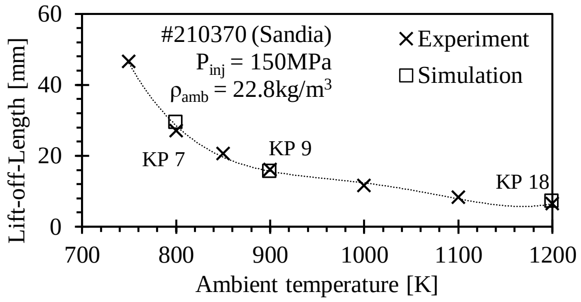

Figure 83: Comparison between simulated LoL against experimental data at constant injection pressure and ambient density conditions.

Jet Penetration

Figure 84 shows temporally resolved reactive jet penetration. The simulation data only starts when the fuel vapour has reacted, hence until the SoC no data are shown in the curve. The experimental data show that a discrete change of ambient temperature has a minor effect on jet penetration if density is kept constant. This indicates that the jet mixing is insensitive to a change in ambient temperature. The SPM’s of the three conditions indicated that the absolute value of turbulence related coefficients in all cases were very similar which reflects this observed insensitivity of the jet to the ambient temperature swing.

The transition from inert to reactive spray requires an increase of the C_1 and C_2 coefficients in the standard k-e model turbulence model to adjust for combustion induced turbulence [46].

Like in the inert cases, once the coefficient value for C_2 is found, it can remain unchanged across conditions.

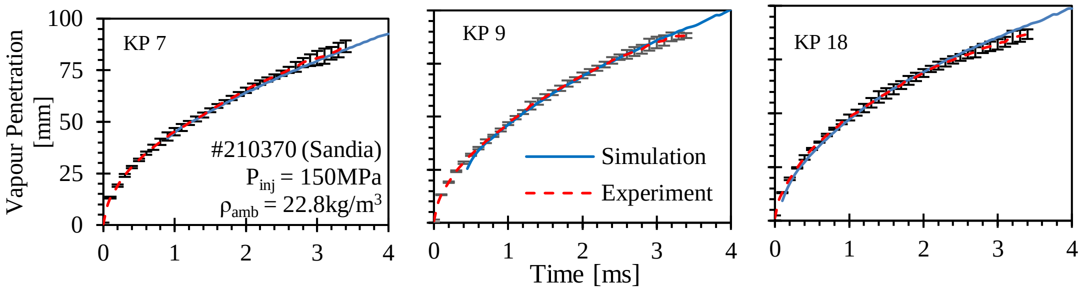

Figure 84: Comparison between simulated jet penetration against experimental data at 800K (l), 900K (m) and 1200K (r) with constant injection pressure and ambient density (#210677, SNL, ρ_{amb} = 22.8kg/m^3, P_{inj} = 150MPa)

Heat release

The temporally resolved RoHR (on the left scale and the total heat release on the right scale of the second row of Figure 85) show that the overall predictions are accurate even though a simple chemical mechanism and auto-ignition model is used. The temporal location of SoC (i.e. the initial heat release rise) are captured well.

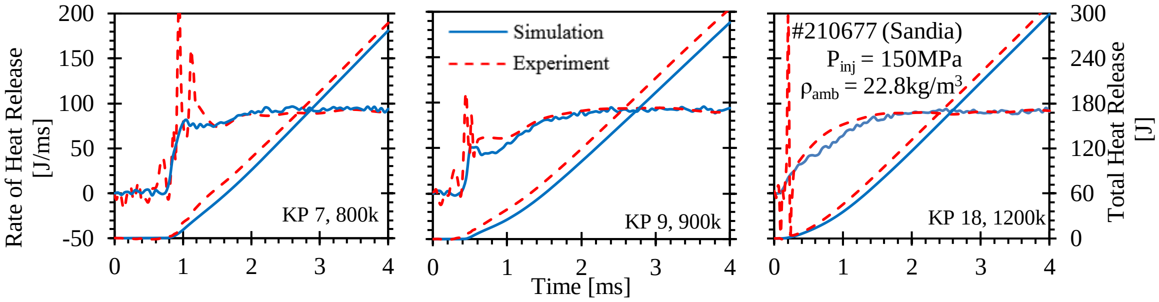

Figure 85: Comparison between simulated RoHR and THR against experimental data at 800K (l), 900K (m) and 1200K (r) with constant injection pressure and ambient density (#210677, SNL, ρ_{amb} = 22.8kg/m^3, P_{inj} = 150MPa)

The discrepancy between simulated and experimental RoHR peaks just after SoC is suspected to be because of underprediction of turbulent viscosity due to high turbulent Schmidt number Sc_t. Recent simulations on light duty Diesel engines in Nsikane *et al* [170] have shown that higher Sc_t raise initial combustion heat release by increasing initial mixing.

7.2.4 Summary of the physicality study

The physicality study was conducted as a reaction to a single setup not being capable of delivering acceptable results for a range of parametric variations of the Spray A configuration. On top of the DoE campaign already conducted for the inert Spray A baseline, seven more DoE campaigns for strategical key points were completed. The resulting SPMs were thoroughly investigated for physically reasonable modelling coefficient patterns.

By comparing the SPM derived simulation settings, some modelling coefficients that were robust to changing boundary conditions and others that had to be adjusted to match the condition were identified. Most importantly, the sensitivity or robustness of the value of a constant was traceable to its original physical expression of the coefficient. A large summary of the individual conclusions of the coefficients is provided in section 7.2.2.3. Here only the most notable are listed as follows:

1. The SPMs helped identify the turbulence coefficients C_1 and C_2 in the standard k-ε model, the KH – B_1 coefficient in the KH-RT model, the drag scaling coefficient A_{drag} in the droplet force calculation and the auto-ignition coefficient c_{ig} in the Livengood-Wu model as the most influential to match experimental data.
2. All turbulence and spray model coefficients can be left unchanged when swinging the boundary conditions. Additionally, the turbulent flame speed multiplier and burn velocity coefficient showed some sensitivity but their effect was negligible in comparison to the auto-ignition coefficient. Lastly, despite some solution sensitivity to the initial cone angle, the trade-off value may remain unchanged due to contradicting optimum values between different metrics.
3. The drag scaling coefficient A_{drag} indicated that droplet deformation increases with rising injection pressures and ambient densities.
4. Initial droplet sizes D_0 are not shown to be sensitive in the SPMs, however a study based on literature and leaning on the Patterson-Reitz droplet introduction model highlights important boundary condition sensitivities that will be considered when tabulating their values.

Running the simulations with their setup derived from the SPMs showed promising results in all available comparison metrics. The performance is summarised as follows:

1. All comparison metrics used for this study are matched in trends and largely absolute values for all inert and reactive Spray A variations.
2. The droplet size evolution for the injection pressure swing now follows a more physically explainable trend while capturing the overall spray penetration accurately.

7.3 Summary and conclusions of modelling coefficient analysis

It is a common approach to simulate parametric variations of boundary conditions with fixed modelling coefficients. To test the validity of this method, an optimiser uses the SPM of the inert Spray A baseline to derive a simulation setup that is predicted match spray and jet penetration. The setup is then validated and all simulated metrics including gas phase temperature, axial and radial mass fraction distributions lie within the experimental error of the source data. Next, the same simulation setup is used for injection pressure and ambient thermodynamic condition swings (all inert). The results of these simulations answer the second research question, which is stated as:

Answer to research question 2

With the given combination of sub models and their modelling coefficients, a single simulation setup valid for multiple parametric variations of a single hardware setup is unlikely to exist.

Following the confident negation of the second research question, parametric variations of the inert and reactive Spray A conditions were used to investigate the links between the physical process of a discrete ambient condition swings and the necessary coefficient adjustments to numerically replicate them. A DoE approach was used in which hundreds of simulations for each condition were run. SPMs then allowed the visualisation of the sensitivities of the different metrics to the change of selected modelling coefficients. Using these models, one simulation setup per key point was selected that was predicted to produce good simulation results. A detailed analysis into the characteristic patterns of the modelling coefficients concerning the changing boundary conditions answered the third research question:

Answer to research question 3

Characteristic and physically reasonable modelling coefficient patterns are found for changing boundary conditions that can be used to guide a priori definition of the simulation setup.

8 Results and discussion III: Tabulation of modelling coefficients

From the physicality study in section 7.2 the boundary condition sensitivities of the key modelling coefficients are now known. This means it is clear whether coefficients must be reduced, increased or may remain unchanged with respect to governing boundary condition. The next step is to derive the modelling coefficient table using the remaining Spray A conditions from Table 5 by simulating them and strictly only changing the modelling coefficients that showed relevant sensitivities.

Using the matching modelling coefficient values of the DoE key points as the basis, only a few iterations are necessary to completely match all Spray A parametric variations. Iterations were necessary due to the auto-ignition coefficient not perfectly following the logic set out for them in the SPMs. These aspects will be discussed in the next sections, where the derivation of the table was split into the different characteristic swings of thermodynamic conditions and injection pressures. The initial results of this modelling coefficient table are published in Nsikane et al in [15]. The detailed analysis shown here are at the point of submission under review.

8.1 Tabulation of changing thermodynamic conditions

This section starts by examining variations of Spray A (KP 9-20, see Table 14) for a range of thermodynamic conditions at constant injection pressure. For these cases, experimental data for heat release and flame-lift off are available for nozzle #210370. The spray penetration is compared to available inert data collected for the #210677 nozzle hence only a qualitative comparison is permitted. The reacting jet penetration is compared only to available data for the temperature swing conducted with the #210677 nozzle. The spray, jet and combustion characteristics are discussed in their separate sub sections starting with the droplet size evolution.

8.1.1 Droplet size evolution

In Figure 86, the droplet size evolution between the lowest and highest density conditions for two temperature conditions are shown. A direct comparison of the temperature effect has already been discussed in section 7.2.3. The ambient temperature change is not expected to influence the initial droplet sizes nor the droplet deformation throughout the break-up. Nonetheless, the higher temperature condition should break the droplets up faster due to increased evaporation rates. This is the reason why a cross-comparison between the temperatures only shows a difference until the 7mm slice.

Table 14: Spray A parametric variations for the tabulation of thermodynamic boundary conditions. For all conditions, the injection pressure is 150MPa.

Key point	Ambient Temp (K)	Ambient Density (kg/m^3)	Chamber Pressure (bar)	Injector (#)	Gas composition at SoI (%)	Comparison data
6	750	22.8	4.9	210370 (SNL NL)	O_2 = 15 N_2 = 75.15 CO_2 = 6.22 H_2O = 3.62	LoL, total heat release, absolute pressure, (inert spray & jet penetration from #201677)
7*	800		5.3			
8	850		5.6			
9*/10/11	900	22.8/ 15.2/ 7.6	5.9/3.9/2			
12/13/14	1000		6.6/4.4/2.2			
15/16/17	1100		7.3/4.8/2.4			
18*/19/20	1200		7.9/5.2/2.6			

*Marked key points were used to in the DoE and stochastic process modelling

The initial droplet sizes are defined leaning on the correlation of the Patterson-Reitz model. As such, the initial droplet sizes of the lower density conditions are larger. Figure 86 also shows that throughout the injection process, the droplets of the lower density case are smaller than those of the high-density case are. This aligns with findings from Jeon and Moon in [25] and Nawi *et al* in [23].

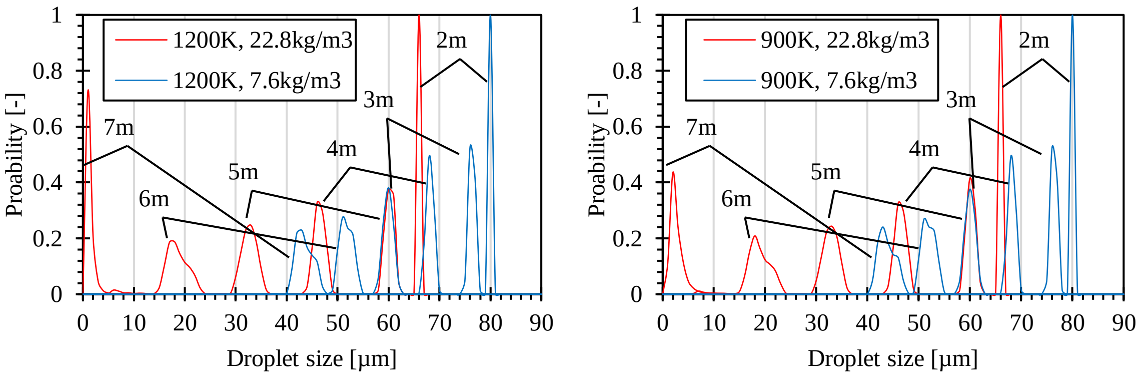

Figure 86: Droplet size comparison between ambient densities for two temperature conditions.

8.1.2 Spray penetration

Figure 87 shows the time averaged spray penetration and LoL over ambient temperature at three ambient density conditions. The simulations are plotted as circles with colours representing different ambient density conditions. The experimental data are plotted as crosses in the corresponding colour. The square symbols indicate the simulations derived from the SPMs.

The effect of gas density on spray penetration is related to turbulent mixing [47, 49, 51]. A detailed discussion of the effect of ambient thermodynamic conditions is given in section

3.1.2. In short, an increase of ambient density comes with an increase of carried energy in the air. The proportion of this is to the square root of the gas, leading to the strong non-linear reduction in of spray penetration. The reason for the decrease in spray penetration at rising ambient temperatures is straightforward. Due to the hotter air, which carries more energy that is being entrained, less time is required to break-up and evaporate the droplets. All simulations using the coefficient table capture this trend accurately. The spray penetrations for lower ambient temperatures and high densities are less well captured.

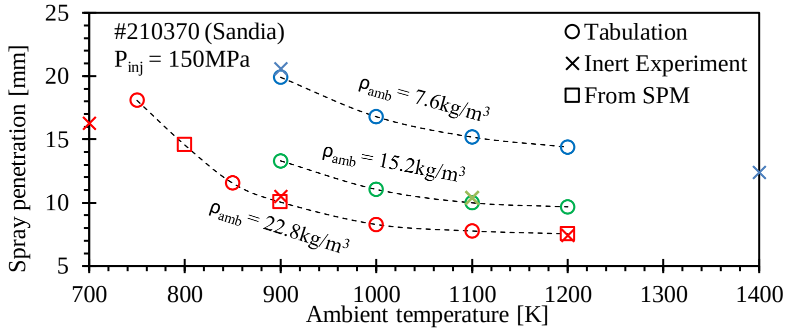

Figure 87: Simulated vs experimental spray penetration at all ambient temperature conditions and at three ambient densities

8.1.3 Lift-off length

Figure 88 shows the time averaged LoL over ambient temperature at three ambient density conditions. The simulations are plotted as circles with colours representing different ambient density conditions. The experimental data are plotted as crosses in the corresponding colour. The square symbols indicate the simulations derived from the SPMs.

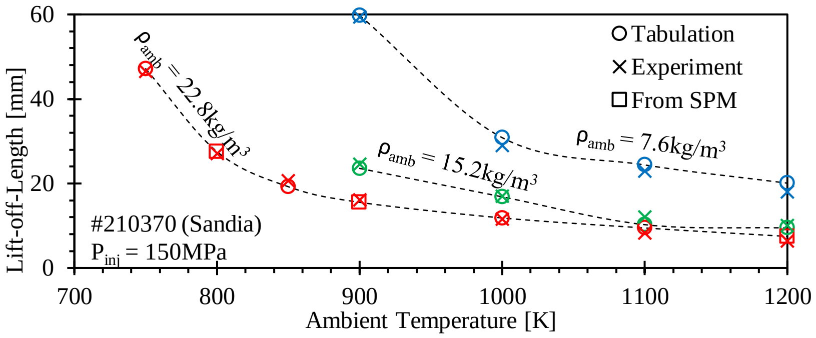

Figure 88: Simulated vs experimental spray penetration and LoL over ambient temperature at three ambient densities

According to Peters' scaling law for gas jets [53], an increase in ambient temperature at constant density affects the thermal diffusivity and the laminar flame speed in a way that results in a faster local flame reaction rate that in turn reduces flame lift-off. This claim is supported experimentally in [47, 49, 51]. The LoL sensitivity to gas densities (decreases with increasing gas densities) cannot be explained with the scaling law but is thought to be a result of combined effects of density induced changes in the laminar flame speed & thermal diffusivity and density effects on the spray development.

8.1.4 Jet penetration

Jet penetration data are only offered for the temperature swing using the #210675 injector of the Spray A condition. Although the nozzles are nominally identical, minor geometrical differences and the operating points of the different datasets must be kept in mind. The simulations of jet penetrations are shown in Figure 89. The discrete temperature swing shows a slightly lower plume velocity (gradient) from 750K – 850K. The ambient temperature appears to have no effect on the jet tip penetration. Knowing that ambient temperatures beyond 850K have no noticeable effect on the jet penetration implies that the increase in jet penetration with the thermodynamic condition swing shown in Figure 76 is predominantly down to density effects. From there it is known that decreasing density leads to increasing jet penetration (Pickett *et al* [40]). Although comparison data are not available for these cases, it can be concluded that at the very least the trends shown by the simulation are correct. The jet penetration is only shown from the start of combustion. This highlights the trend of the ignition delay decreasing when ambient temperatures increase. This effect will be discussed in the next section.

8.1.5 Heat release

The total heat release and RoHR for these cases are shown Figure 90. The simulations show good agreement with the experimental data. The start of ignition, the shape of transition from ignition to steady state burn and the absolute value of the steady state heat release are well captured by the simulations. At the time of writing, the results shown here are, to the best of my knowledge, the best agreements for heat release data of the Spray A condition and its parametric variations. One clear weakness of the used modelling coefficients appears to be capturing the heat release spikes. This was previously discussed in section 7. There the problem is identified to be the high turbulent Schmidt number Sc_t causing slower mixing due to low turbulent viscosity. In the engine cases that will be discussed in the next chapter, lowering Sct greatly benefited the capturing of this early combustion event.

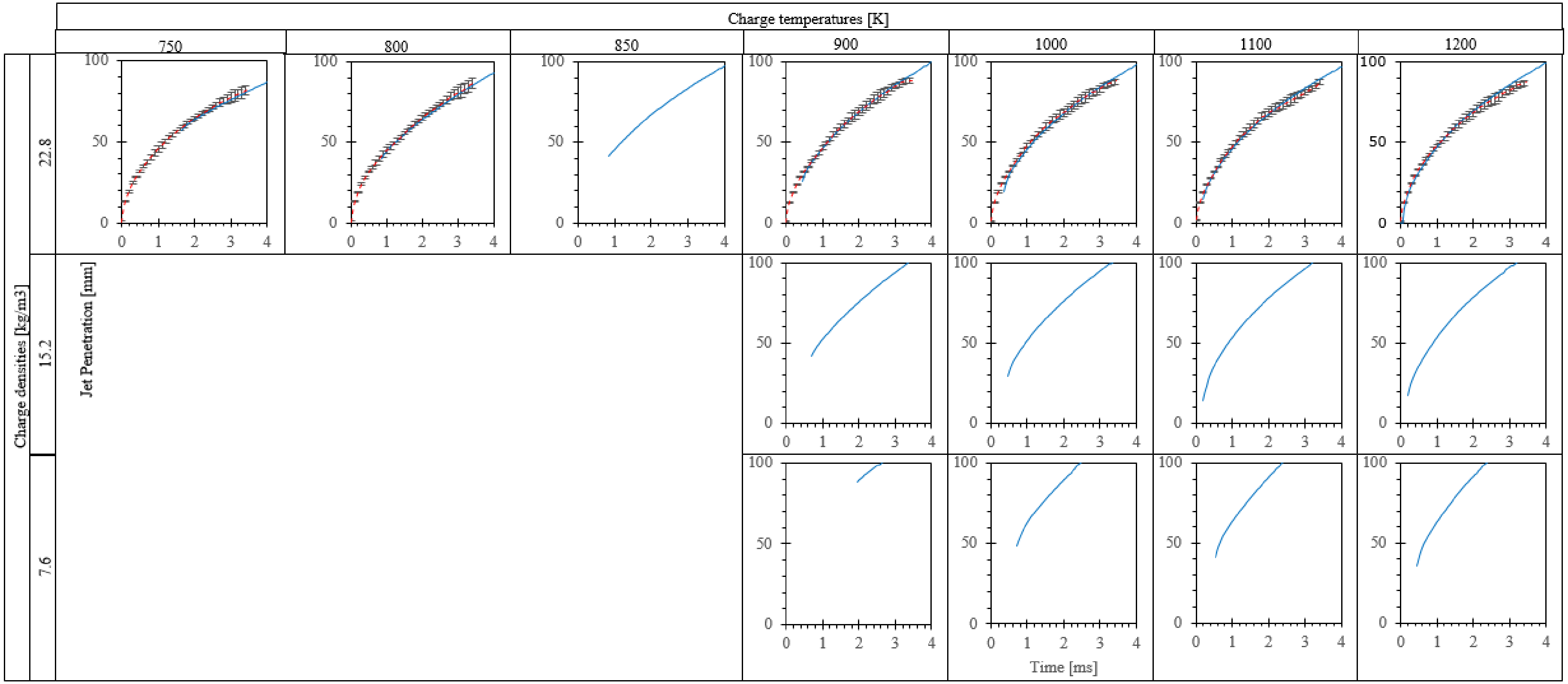

Figure 89: Simulated (blue solid) vs experimental (red dashed) jet penetration for different thermodynamic chamber conditions.

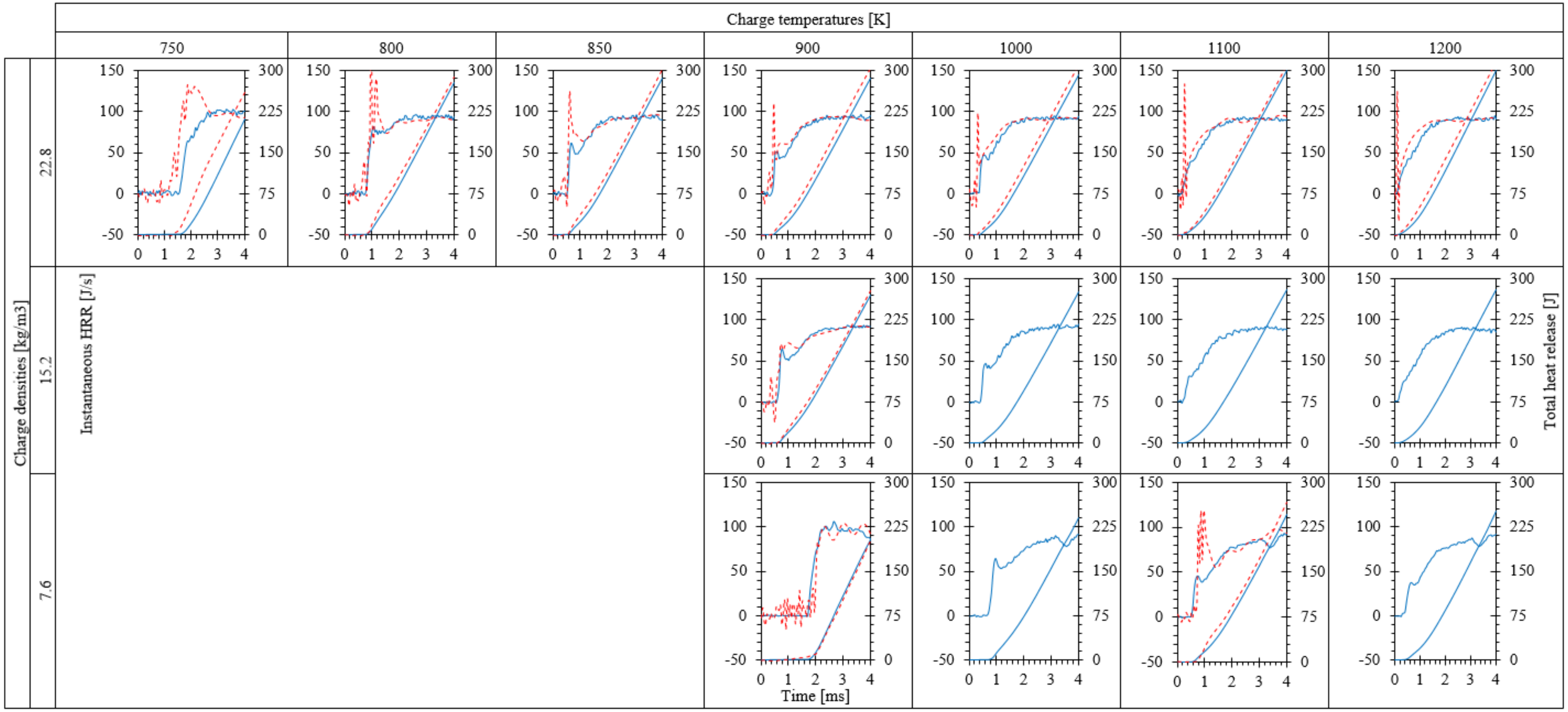

Figure 90: Simulated (blue solid) vs experimental (red dashed) RoHR and total heat release for different thermodynamic chamber conditions.

8.1.6 Coefficient tabulation

For the simulations to match the experiments, the Livengood-Wu auto-ignition model, droplet drag force scaling and initial droplet sizes proved to be the key modelling coefficients. The boundary condition dependencies of these three modelling coefficients are shown in Figures 91-93. The exact coefficient values may not be shown due to confidentiality constraints, which however does not impede the qualitative nature of the graphs. What is of interest is to explore the physics that the trends in the change of the coefficients indicate.

Auto-ignition coefficient

The auto-ignition coefficient must be changed both within the ambient temperature and density swings. A rise in the auto-ignition coefficient signifies a reduction of the time integral, which results in advanced auto-ignition. The curves shown in Figure 91 exhibit a clear non-linear progression which poses a challenge for tabulating this coefficient.

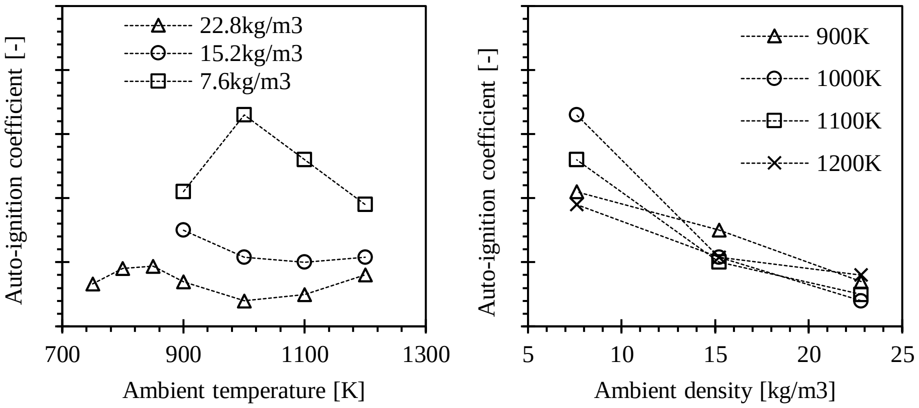

Figure 91: Tabulation of the auto-ignition coefficient for changing ambient temperature and density conditions at constant injection pressure of 150MPa. The coefficient values are removed for confidentiality reasons. The coefficient value scale is identical for all auto-ignition coefficient plots.

An initial study into the non-linear nature of this curve suggests it is most likely due to the complex ignition delay characteristics of the n-dodecane fuel. The auto-ignition model is not capturing the ID accurately and needs user-intervention. The reasons for this could be flaws in the chemical mechanism, simplicity of the ignition model or errors in the simulated local mixture characteristics at the supposed SoC. While miscalculation of local conditions is always a possibility, the approach leading up the reactive Spray A simulations was rigorous in characterising the mixture fraction distributions. It is more likely that the simplicity of the ignition model has a larger contribution to simulation errors ID.

Despite the strong non-linearity, some useful information is derivable from Figure 91. First, an overall temperature-independent reduction of the auto-ignition coefficient with increasing ambient densities is noticed. This allows rough extrapolation to higher density conditions. Secondly, the fluctuations of the curves decrease with increasing ambient densities. For increasing densities, a flattening of the curve at lower absolute values is expected. A detailed analysis of the reasons for the strong sensitivity at low-density conditions was forgone on the grounds of engine simulation typically being above 20kg/m^3. Speculatively however, this sensitivity may be connected to the domination of chemical kinetics at these conditions.

Initial droplet sizes

With increasing ambient density at constant temperature (compensated by chamber pressure), a necessary decrease in initial droplet sizes is recorded. These changes of droplet sizes cannot solely be attributed to nozzle dynamics because the difference in pressure drop between these cases ranges only between 144 and 148MPa. Instead, the impact of gas density on a droplet is linked to the Weber number, which increases with a rise in density. This makes the droplet more unstable and easier to break-up [24]. Experimental findings from Nawi *et al* in [171] show that with increasing ambient density under evaporating conditions (which supresses droplet coalescence), the probability of smaller droplets sizes is increased. This trend is followed by the droplet sizes shown in Figure 92.

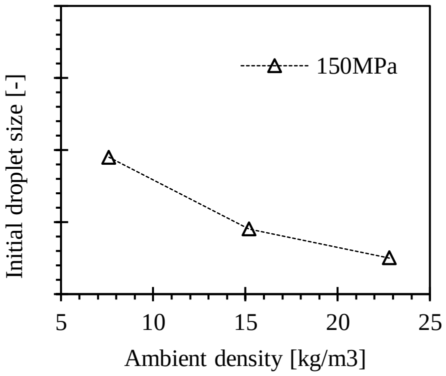

Figure 92: Tabulation of the initial droplet sizes for changing ambient temperature and density conditions at constant injection pressure of 150MPa. The coefficient values are removed for confidentiality reasons. The size scale is identical to all other initial droplet size plots.

The initial droplet sizes appear to be insensitive to ambient charge temperatures. Although rising evaporation rates play a role, they affect the downstream droplets and are subject to the spray break-up and evaporation model. These two models appear to handle temperatures swings well and therefore do not need user-intervention.

Drag scaling coefficient

The drag scaling coefficient scales the drag coefficient that is calculated by the Putnam model. As shown in Figure 93, it exhibits a decrease with increasing density. This means that with increasing density, the droplet drag coefficient continuously reduces, which implies an increasing deviation form sphericity. This is a characteristic found within droplets exposed to high sheer due to increased aerodynamic resistance.

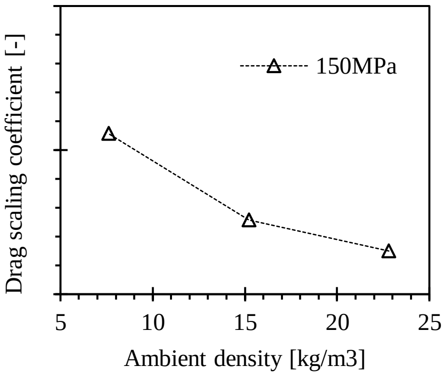

Figure 93: Tabulation of drag scaling coefficient for changing ambient temperature and density conditions at constant injection pressure of 150MPa. The coefficient values are removed for confidentiality reasons. The coefficient value scale is identical to all drag scaling coefficient plots.

Like the initial droplet sizes, the drag scaling coefficient is not, nor is expected to be, sensitive to changing ambient temperatures. The ambient temperature and pressure effects on heat transfer and droplet evaporation are calculated by the evaporation model.

8.2 Tabulation of changing injection pressures

Injection pressure is one of the key aspects of spray injection dynamics. In this section, variations of Spray A have incrementally increasing injection pressures between 30 – 150MPa and four ambient temperature conditions while ambient density is held constant at 22.8kg/m^3. Experimental spray penetration and LoL data are marked with crosses and simulated with rings with the temperature condition colour coded from blue (cold) to red (hot). Experimental spray penetration data for the 900K cases are taken from inert cases and only used as reference.

The datasets of the key points 21-41 were collected by CMT using the #210675 nozzle. Some of the key points overlap nominally with those from the SNL. However, the injection rate used by CMT is slightly higher, hence not permitting a direct comparison to the jet penetration and heat release data from the other nozzles because these two metrics are highly sensitive to changing injection rates. The spray penetration shows little sensitivity hence can be used at least for the 900K case [13].

Table 15: Selection of key points for the analysis of the injection pressure swings. The ambient density for all cases is 22.8kg/m^3.

Key point	Ambient Temp. (K)	Chamber Pressure (bar)	Inj. Pressure (MPa)	Injector (#)	Gas composition at SoI (%)	Comparison data
21/22/23	750	5.1	50/100/150	210675 (CMT)	O_2 = 15 N_2 = 85	LoL, ignition delay, spray penetration to #210677
24/25/26	800	5.4				
27/28/29	850	5.75				
36/37/38	900	6.09	30/50/75			
39/40/41			100/125/150			

8.2.1 *Spray penetration*

Liquid length, as shown in Figure 94, is almost independent of injection pressure as it is predominantly determined by air entrainment (or turbulent mixing). As mentioned before, in turbulent mixing, the local interphase transport rates of mass, momentum and energy (which determine liquid break-up) must be fast relative to turbulent mixing rates.

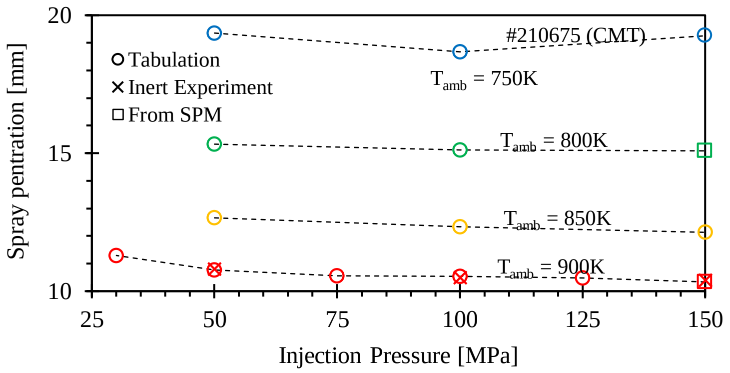

Figure 94: Simulated spray penetration under increasing injection pressures at constant ambient conditions. The shown experimental data for the 900K case is taken from inert Spray A cases and a different nozzle and should only be used as reference.

The turbulent mixing defines the rate at which energy is entrained into the spray. An increase of fuel mass can always provide the spray with enough fresh gas to be entrained, and hence keep the equilibrium. The temperature sensitivity at constant injection pressure shown was previously discussed in section 8.1. The settings used in the simulations accurately produce trends in which the spray penetration is insensitive to injection pressure, but sensitive to ambient temperature.

8.2.2 Lift-off length

Figure 95 shows a good quantitative and qualitative agreement between experimental and simulated LoL. The experiments show a clear near-linear trend of increasing LoL with increasing injection pressures.

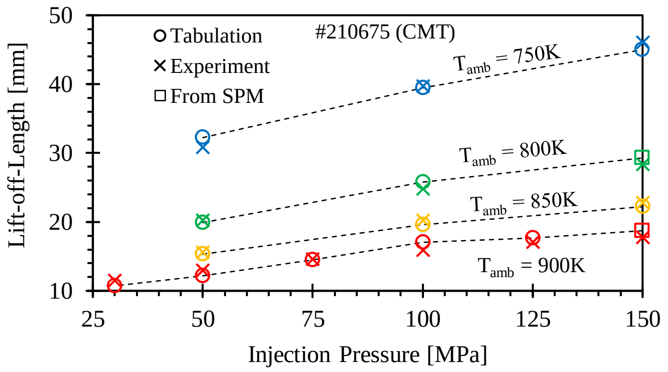

Figure 95: Simulated vs experimental LoL under increasing injection pressures at four ambient temperature conditions.

Siebers and Higgins in [49] show that the sensitivity in fact stems from the injection velocity rather than the pressure drop and refer to the analytically derived scaling law by Peters in [53]. The turbulent mixing rate increases in proportion to the increase in injection velocity. The ambient temperature effects were previously discussed in section 8.1. The simulation setup derived from the table accurately predicts both ambient temperature and injection pressure dependant trends.

8.2.3 Jet penetration

The jet penetration for these key points is shown for completeness in Figure 96. No experimental measurements for this metric are available and comparisons to similar conditions from other institutions are not possible due to the differing rate of injection and the strong sensitivity of the penetration rate to this change.

With rising injection pressures, a clear increase in jet penetration rate is visible. Heikki *et al* stipulates in [39] that the increase in jet penetration rate at higher injection pressures is caused by the higher relative liquid phase velocity which in turn induces higher gas velocities and turbulence levels. At constant injection pressure and decreasing ambient temperatures, a reduction of the penetration rate is observable. This trend was also shown in Figure 89 in section 8.1.4. There the effect of this appears to stagnate after reaching 900K. The mechanism behind this is unclear.

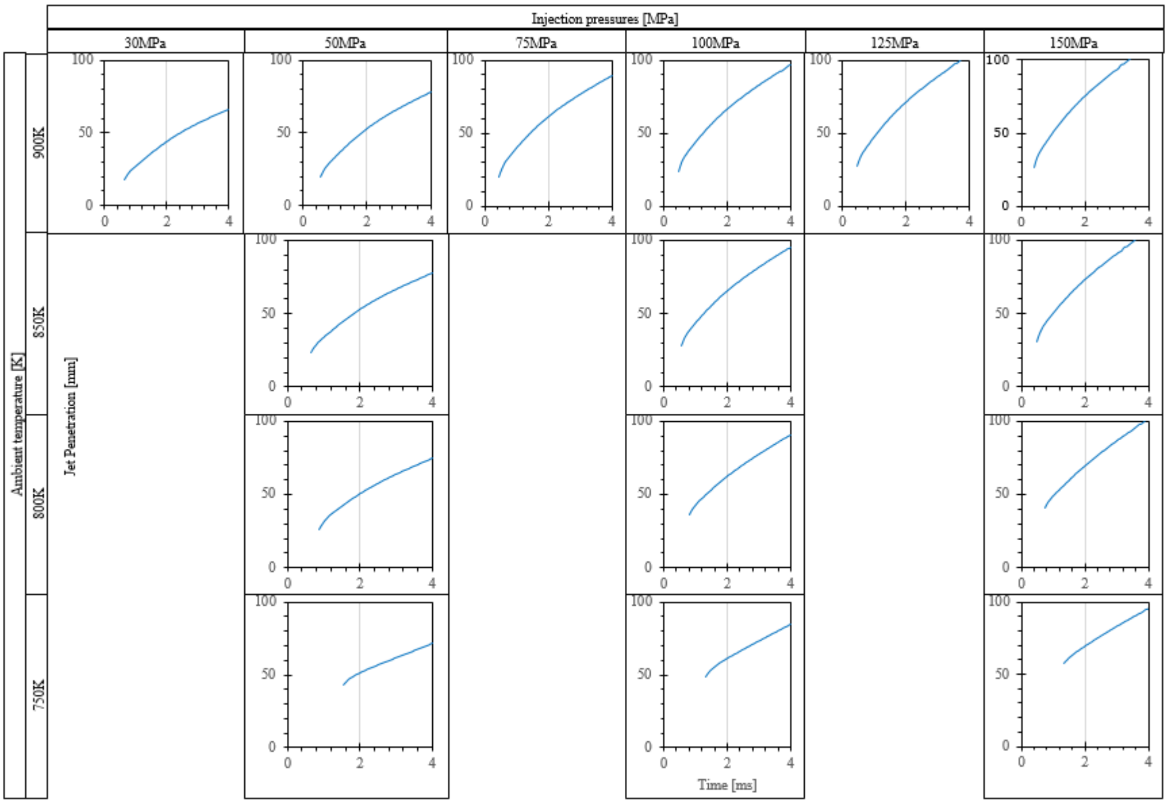

Figure 96: Simulated jet penetration for a range of injection pressures at four ambient temperature conditions

8.2.4 Heat release

The heat release data shown in Figure 97 was not comparable to similar cases due to the differing injection rates as already mentioned in this section. The simulations, however, still show relevant trends that must align with previous findings to make sure that the modelling coefficient table performs physically correct.

In Figure 97, the RoHR and total heat release are shown for multiple injection pressures and temperature conditions. Within the injection pressure swing two processes are evident. Firstly, the start of combustion (or ID) remains roughly unchanged. Secondly, both the steady state instantaneous and the gradient of the total heat release rise due to increased fuel mass being burned. With decreasing temperatures comes an increase of ID due to decelerated chemical reactions. Simultaneously, the characteristics of the combustion change. At higher temperatures, earlier combustion means that the initial combustion is weaker (less available mixture) and that the remaining fuel is injected into a burning flame resulting in the round transition into the steady state. In contrast, the delayed auto-ignition at lower temperatures leads to more of the fuel premixing before it all ignites together leading to a sharp rise of heat release. The result is a square shaped heat release rate curve.

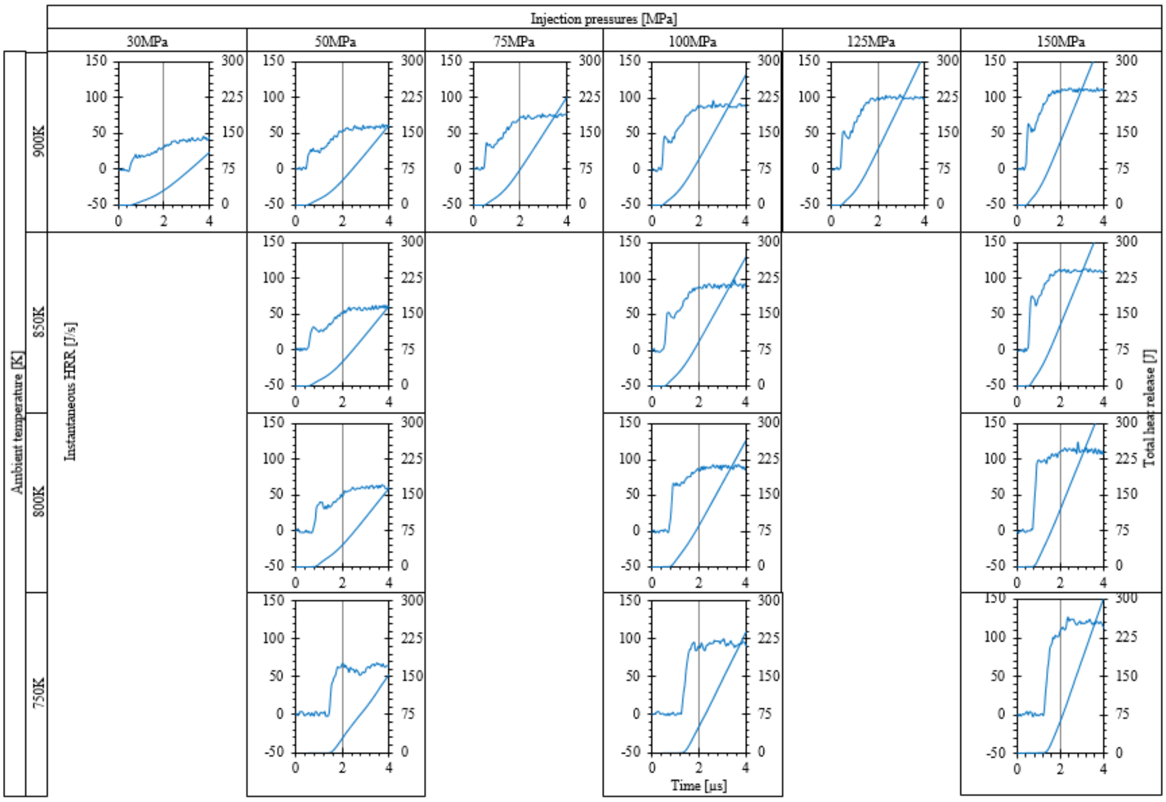

Figure 97: Simulated RoHR and total heat release for a range of injection pressures at four ambient temperature conditions

8.2.5 Coefficient tabulation

The coefficients required to be adapted to produce the results of this injection pressure swing of Spray A are shown in Figures 98 and 99. The initial droplet sizes and the drag scaling coefficient are each plotted as a function of injection pressure or as injection pressure variations over ambient density. The auto-ignition coefficient appears to be insensitive to changing injection pressures.

Initial droplet sizes

The initial droplet sizes in Figure 98 are set to decrease in size as the injection pressure increases. This is in line with findings in the literature by Crua *et al* in [131] that with an increasing injection velocity the droplet break-up becomes more rapid as shear forces become stronger. The blob method does not account for any in-nozzle process changes that occur when injection pressure is raised. Therefore, the coefficient table accounts for this by introducing smaller droplets. The droplet size dependency on ambient density was shown and discussed in the previous section but is here expanded to host the varying injection pressures.

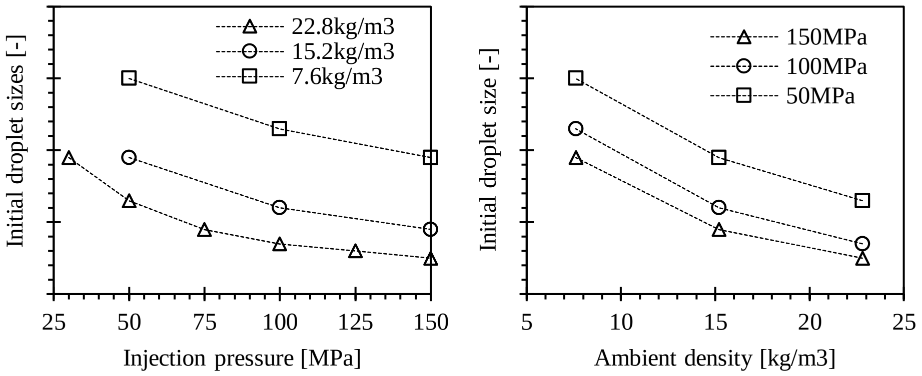

Figure 98: Tabulation of the initial droplet sizes over injection pressures and ambient densities. The coefficient values were removed for confidentiality reasons.

The droplet size sensitivity to both condition swings is relatively straightforward to project into elevated conditions. This means for increasing injection pressures, the initial droplet sizes are expected to drop, however at a smaller rate. Similarly, for increasing ambient densities, the projection of the curve indicates an asymptotic progression of the initial droplet sizes. This means that at higher ambient densities the droplet sizes should be smaller, but at decreasing margins.

Drag scaling coefficient

The drag scaling coefficient shown in Figure 99 indicates that with increasing injection pressures and ambient densities the droplets increasingly deform. This is a characteristic found within droplets exposed to increasing sheer due to rising relative injection velocities and aerodynamic resistance. The ambient density effect was described for the 150MPa case in the previous thermodynamic conditions swing. Here, the graph was expanded to also show the how the drag scaling coefficient must change for dropping injection pressures.

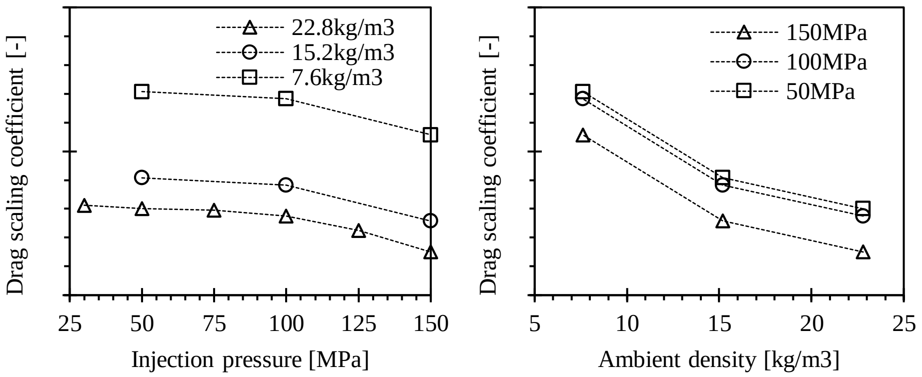

Figure 99: Tabulation of the drag scaling coefficient over injection pressures and ambient densities. The coefficient values are removed for confidentiality reasons.

8.3 Tabulation with changing ambient density and injection pressure

The final investigation includes a swing of ambient density at three different injection pressures. The results are partially inferable from the previous results. For the conditions listed in Table 16, ambient temperature is held constant by adjusting the chamber pressure while at each of the ambient density conditions there are three injection pressure variations to compare to. The data are from the #210675 nozzle used by CMT, which means only flame lift-off and ignition delay data are available. Despite this, spray and jet penetration and heat release simulations are shown for completeness.

Table 16: Selection of key points for the analysis of the simultaneous ambient density and injection pressure swings. The ambient temperature for all key points is 900K.

Key point	Ambient Density (kg/m^3)	Chamber Pressure (bar)	Inj. Pressure (MPa)	Injector (#)	Gas composition at SoI (%)	Comparison data
30/31/32	7.6	2.02	50/100/150	210675 (CMT)	$O_2 = 15$ $N_2 = 85$	LoL, ignition delay
33/34/35	15.2	4.03				
37/39/41	22.8	6.09				

A discussion of the modelling coefficients at the end of this section is not performed because all relevant sensitivities were discussed in the previous two sections.

8.3.1 Spray penetration

The spray penetration of the injection pressure swing at three density conditions is shown Figure 100. The shown comparison data are taken from the inert condition of a #210677 nozzle from an experiment run at the SNL (with differing rates of injection) hence only a qualitative comparison is performed. As expected, only a small deviation between the injection pressures is shown. An increase of fuel mass and velocity can always provide the spray with enough fresh gas to be entrained, and hence maintain the equilibrium. A steep decline in spray penetration with increasing densities is also expected due to increased energy carried by the ambient air. These aspects were discussed in more detail in the previous sections in this chapter.

One inconsistency is visible in Figure 100. For the lowest and highest density conditions, the spray penetration decreases slightly with increasing injection pressure. This is the expected and was discussed in section 7.2. However, at the intermediate ambient density condition, the key point with a 100MPa injection pressure shows the lowest spray penetration. The difference is very small but shows that the modelling coefficient table requires some more refinement to capture all processes accurately.

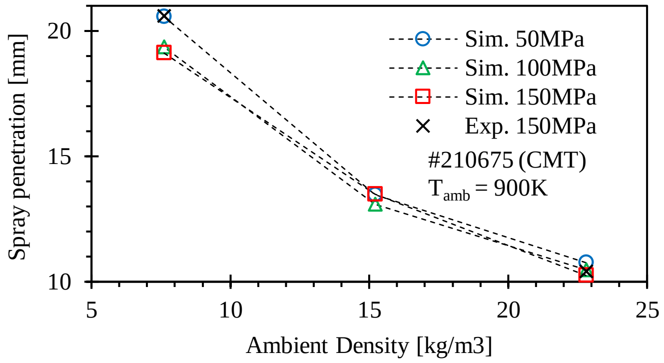

Figure 100: Spray penetration of injection pressure swings for three ambient density conditions

8.3.2 Lift-off length

In Figure 101, the LoL is plotted as a function of ambient density. The curves are grouped symbolically as circles for the tabulated setup and crosses for the experimental comparison data. Colouring is added for further visual separation between the injection pressure conditions. The LoL increase due to changes of ambient density at given injection pressure and ambient temperature has been discussed in section 8.1. The effect of injection pressure on flame lift-off within a given density and temperature condition is described in section 8.2.

One additional observation is that initial large difference of LoL reduces to only ~4mm between the highest and lowest pressure condition towards higher densities. This indicates that while at lower densities, the chemical kinetics is the dominant parameter for ignition delay, at higher densities the ignition is triggered by diffusion (almost) regardless of the injection pressure. Therefore, it can be assumed that for increasing densities, such as for full-load, the LoL will decrease only slightly and the difference between the injection pressures conditions will further reduce.

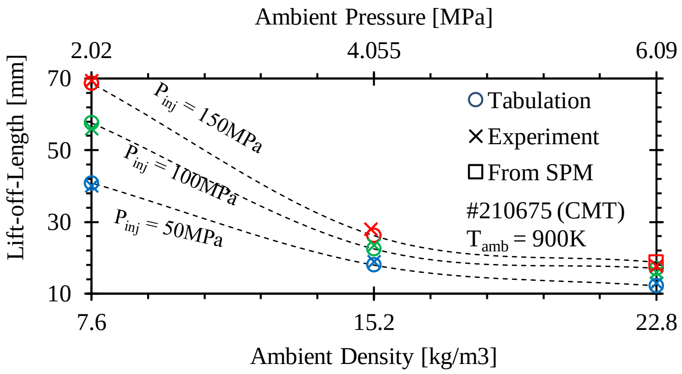

Figure 101: Simulated vs experimental LoL of three injection pressure conditions under an ambient temperature swing at changing ambient density

8.3.3 *Jet penetration*

The jet penetration plotted in Figure 102 as function of (1) ambient density and (2) injection pressure confirms two dependencies highlighted in previous sections. The jet penetration rate decreases with rising ambient densities and dropping injection pressures. The dependency on injection pressures stems from the momentum of the droplets transferred from the liquid to the vapour phase. Faster droplets (i.e. higher injection pressures) pass on more momentum resulting in longer jet penetrations. Lowering the ambient density has the effect of reducing both aerodynamic resistance and diffusion. The result is a faster and thinner spray plume. Although no direct comparison can be made to experimental data, the trends shown are physically reasonable and follow claims in the literature [39, 40].

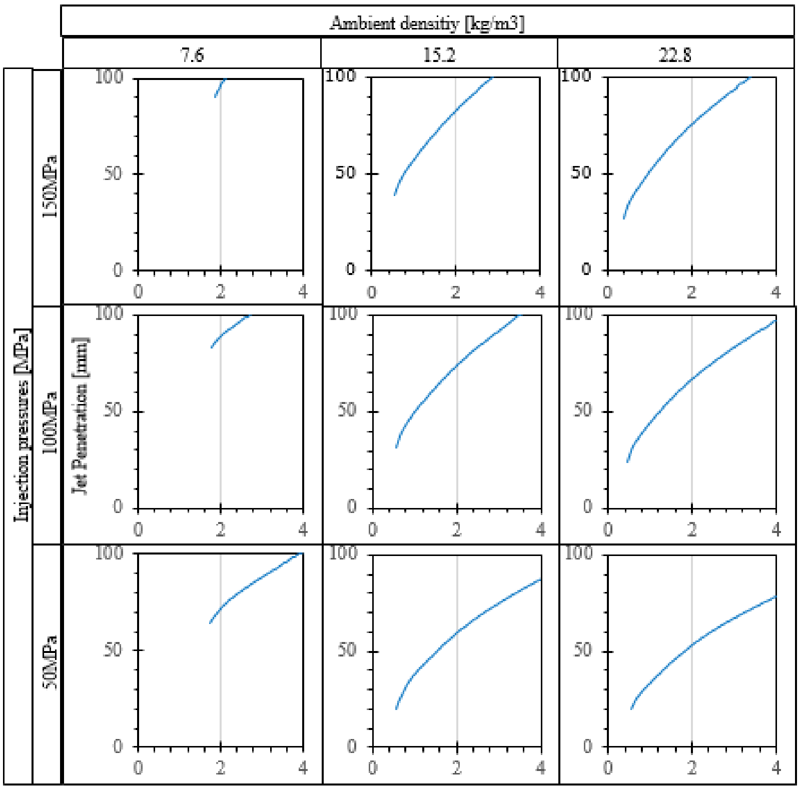

Figure 102: Simulated jet penetration for a range of injection pressures at three ambient density conditions at an ambient temperature of 900K

8.3.4 *Heat release*

The graphs in Figure 103 show the responses of RoHR and total heat release to changing densities (rows) and injection pressures (columns). The increase of ambient density from the lowest to the highest shows a similar behaviour to increasing temperatures shown in section 8.2.4. With increasing ambient density, the ignition delay shortens and develops a clear transition period between the initial ignition event and the steady state burn phase. These graphs combined with Figure 101 show that even with increasing density (or temperature) the ignition timing and the location cannot be advanced indefinitely and that these characteristics plateau beyond 20kg/m^3 or 900K.

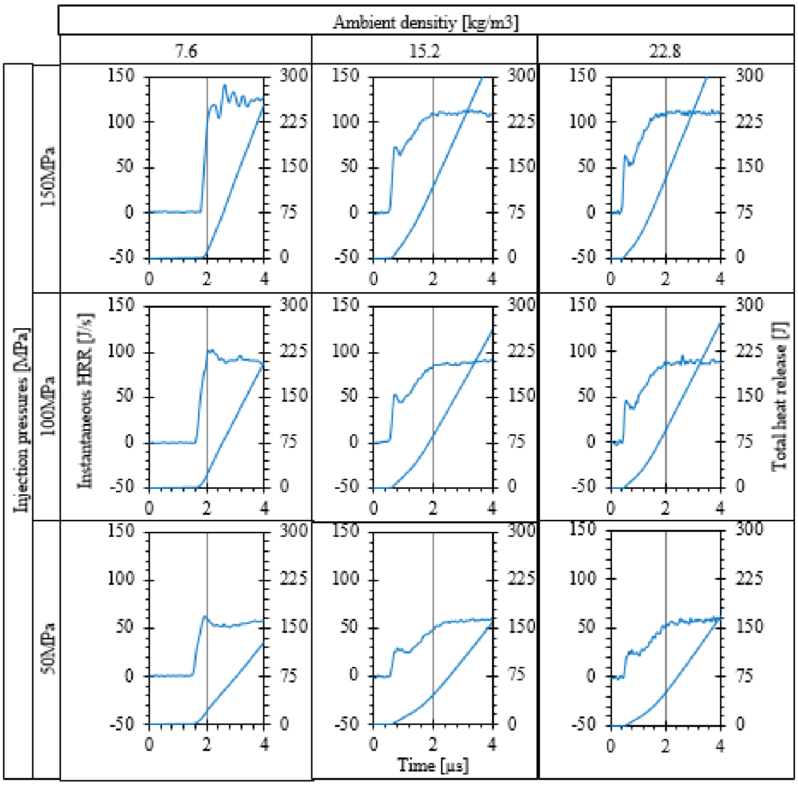

Figure 103: Simulated instantaneous and total heat release for a range of injection pressures at three ambient density conditions at an ambient temperature of 900K

8.4 Summary of the development of the coefficient table

The sensitivities found under discrete conditions swings for inert and reactive Spray A conditions are the basis for the extraction of a modelling coefficient table. Knowing which coefficients should remain unchanged and which must change and by how much is the key information for targeted selection of the simulation setup. The settings for all non-DoE Spray A conditions are set up using the characteristics found in section 7.2. This means that the drag scaling coefficient, the initial droplet sizes and the auto-ignition coefficient are varied during the boundary condition swing they were identified to be sensitive to while all other coefficients were held constant at their SPM-derived optimum value. The simulations showed good results, but also highlighted some necessary adjustments for coefficients that were more sensitive than initially suspected (i.e. the auto-ignition coefficient).

The simulated results were convincing, confirming the potential of such a modelling coefficient table. In most simulated conditions, the comparison metrics were well captured both in trend and in absolute values. Some improvement to the low temperature (>850K), low injection pressure (~50MPa) conditions may be necessary, however are not of the focus for this thesis as these fringe conditions have little relevance for real engine conditions. The establishment of this range of confidence guarantees an a priori definition the simulation setup for any parametric variation of the configuration to be simulated without iterations. The trends shown by the coefficient tables also showed encouraging interpolation and extrapolation potential which is explored in the next chapter.

9 Results and discussion IV: Validation on engine cases

Following the development of the modelling coefficient table, the next step is to apply the found values for real engine conditions. There are fundamental differences between the governing boundary conditions in a CV-vessel and real engine conditions. The most significant differences are the sharp thermodynamic gradients induced by the moving piston and heat transfer effects to the surrounding walls and the different turbulence levels produced by the intake stroke and by plume-to-plume interactions.

An attempt no to change too many simulation aspects at once, the engine cases are carefully chosen. The first is an optical engine that is operated at a load condition like that of KP 38 of the Spray A configuration and therefore lies well within the range of confidence of the coefficient table. This allows the coefficient values to be interpolated from surrounding operating conditions. The production engine, which is operated at full-load, then requires an extrapolation outside of the initially developed range of confidence. To reduce the number of unknowns, a geometrically similar engine setup to the optical engine is selected. The exact details of the production engines are confidential. The engine configurations are discussed in section 4.2. The results discussed in this chapter were also published in Nsikane *et al* in [17] and have since been improved.

9.1 Applying the coefficient table

To find the simulation setup that will be used for the two LDD DI engines, the modelling coefficient table is consulted. The modelling coefficients are selected for the thermodynamic boundary conditions at SoI. The description of the definition of these values is provided in the following sub sections.

Auto-ignition coefficient for LDD DI engines

The selection of the values for the LDD DI engines is based on interpolating and extrapolating from the developed range of confidence from the Spray A configurations. Figure 104 shows the overlay of both engine conditions into the modelling coefficient table to describe the selected values.

The coefficient lines that are not immediately necessary to derive the engine simulation value are removed to aid clarity. The value of the auto-ignition coefficient for the optical engine (925K, 21,8kg/m^3) lies between two Spray A key points. The selection of the coefficient for the full-load (1045K, 32kg/m^3) condition requires extrapolation of the 1000K and 1100K.

The fact that the value should have been between the lines was identified too late to be corrected. A corrected value, however, will have little impact due the auto-ignition coefficient losing importance at high density (short IDs).

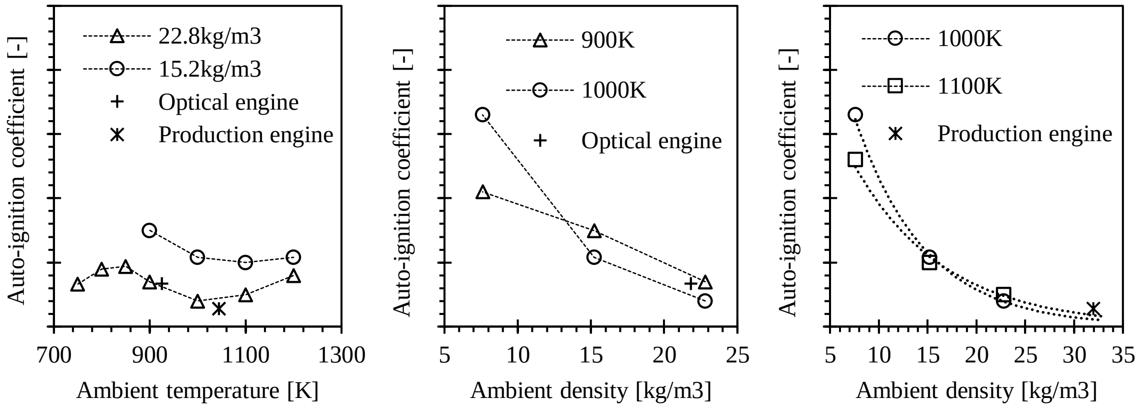

Figure 104: Graphical representation of the selected auto-ignition coefficient for the LDD DI engine simulations. The coefficient values were removed for confidentiality reasons.

Drag scaling coefficient for LDD DI engines

The drag scaling coefficient is derived similarly. The values from the surrounding Spray A settings are interpolated and extrapolated. Finding the drag coefficient for the optical engine is simple due to the 22.8kg/m3 line established during the development of the table. Additionally, there exists a Spray A configuration with a 75MPa injection pressure. The values for the optical engine simulation are therefore almost identical to key point 38. The coefficient value for the production engine is derived from extrapolating the 150MPa line of the 900K set of experiments (note, ambient temperature plays no role). A slightly lower coefficient value than the extrapolated value is chosen to account for the 10MPa higher injection pressure.

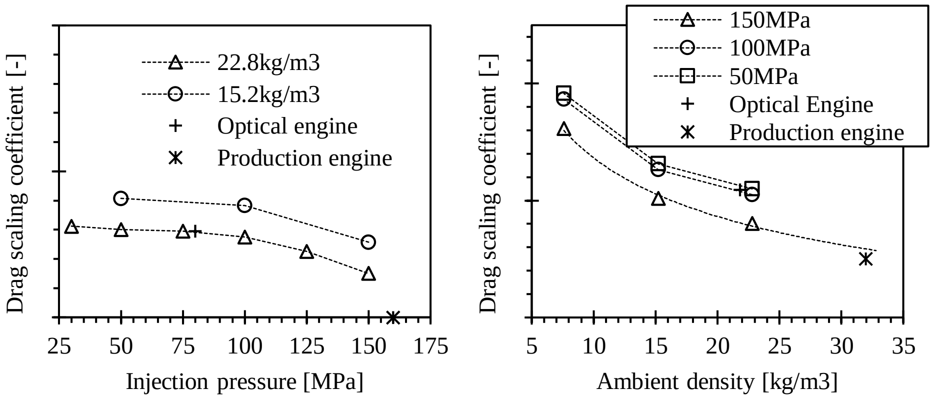

Figure 105: Graphical representation of the selected drag scaling coefficient for the LDD DI engine simulations. The coefficient values were removed for confidentiality reasons.

Initial droplet sizes for LDD DI engines

A tabulation of the initial droplet sizes concerning changing nozzle sizes has not yet been achieved. To continue with this task, the initial droplet sizes calculated by the Patterson-Reitz model are scaled like in the Spray A configuration. In future, an independent initial droplet size calculation that, like the Patterson-Reitz model, considers gas and liquid conditions as well as basic FIE parameters should be perused.

9.2 Cylinder pressure and heat release

Figure 106 shows the comparison between simulated and experimental in-cylinder pressures for both load conditions over crank angle. Directly carrying over the simulation setup from the Spray A setting derived from the tabulation results in an under-prediction of peak cylinder pressure (orange/dashed line). The combustion induced pressure rise and peak cylinder pressure are better captured by the simulation with the turbulent Schmidt number Sc_t and raised the dissipation coefficient C_2 (blue/solid line). Minor discrepancies against the experimental data (black/dotted line) are visible during the compression and, to a lesser extent, the expansion stroke. The improvement is significant in comparison to a simulation setup with the model settings left at default (green/dash-dotted line). The default setup appears to produce a good agreement for the part load conditions, but later analysis of the burn characteristics reveals shortcomings.

The RTZF combustion model calculates the enthalpies of formation from change of absolute enthalpy to change in total sensible enthalpy. The total heat release is derived from heat release contributions in every given time-step from the difference in formation enthalpies based on the conditions in every computational cell, the inlet/outlet boundaries and the compensation due to cooling effect from the spray. The final heat release is then a result of these contributions over the time-step size. This heat release is compared to the heat release derived from the respective engine pressure traces. Since they were obtained at different institutions and follow different post-processing routines and both methods differ from the way VECTIS calculates its heat release, only a qualitative comparison is possible.

Figure 106 shows a comparison between the RoHR and total heat release (black / dotted line) derived from the cylinder pressure trace and the VECTIS simulations using the “Spray A Tabulation” and its modification. In the case of the “Modified Tabulation” (blue / solid line), the Start of Combustion (SoC) and overall burn characteristics are captured well. For the production engine case some discrepancies can be seen at the peak and the transition into the tail of the heat release curve, indicating that some fuel that is not burned during the peak of the injection phase is burning later in the cycle. The original “Spray A Tabulation” (orange / dashed lines) shows a slow burn that extends throughout the expansion stroke. This is the main indication that the fuel mixing is occurring too slowly and must be increased by modifying the turbulence coefficients. For both cases, the ignition delay is well reproduced.

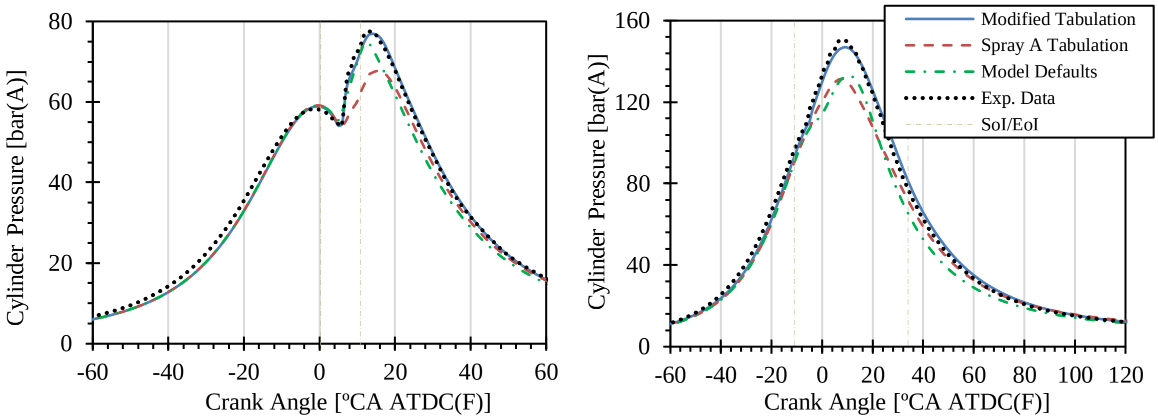

Figure 106: Comparison between simulated and experimental averaged ambient pressure over crank angle. SoI/EoI = Start/End of injection

The delay time allows the fuel vapour to mix and reach the thermodynamic state at which it ignites. A slower mixing under less extreme conditions like the part-load condition allows for longer mixing time which then leads to a higher RoHR when the mixture eventually ignites. Under the high load condition, the threshold for ignition is crossed as the fuel is mixing. This produces a more progressive heat release, i.e. without the presence of a large premixed spike. Both these burn characteristics are presented in Figure 107.

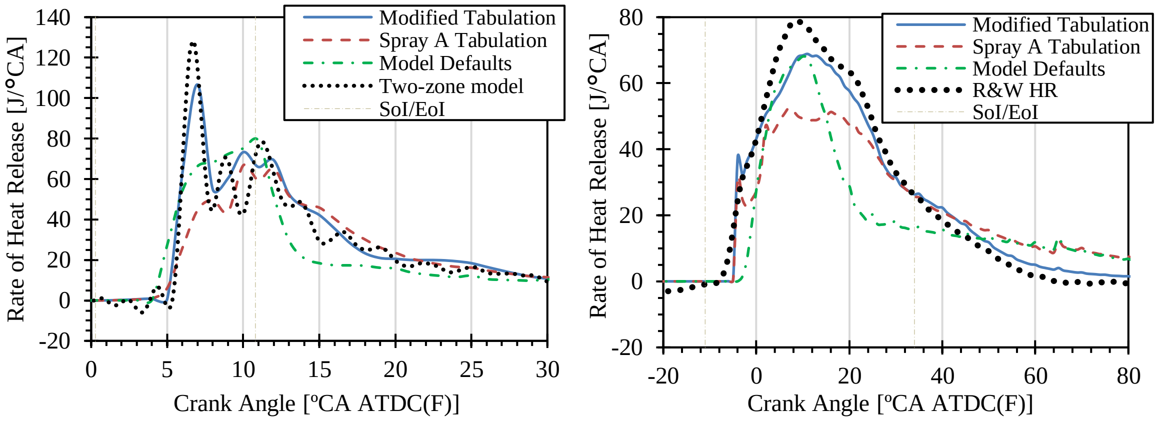

Figure 107: Comparison between simulated and experimental RoHR over crank angle

Again, a significant improvement against a model setup following default modelling coefficients (green / dash-dotted). For the optical engine, combustion commences too early, and for the production engine too late, indicating that either the mixing is not occurring with the appropriate rates or the combustion model is delay/advancing the combustion incorrectly. In both cases, the heat release prematurely decreases sharply with a slow burn towards the end of the combustion.

9.3 Spray penetration

The time resolved spray tip penetration for both key points is plotted in Figure 108. For the optical engine, experimental data for individual holes is available but has here been averaged. The simulated peak penetration and initial decline agrees well with the measuremnts. The shortening of spray penetration between the “Spray A Settings” and the “Modified Tabulation” is attributed to the increase of the dissipation coefficient C_2. An increase of this parameter enhnaces turbulent mixing, which as stipulated by Siebers in [13], shortens spray penetration due to the enhanced evaporation of droplets through exposure to more fresh hot ambient air. The increase in spray penetration after the end of injection, which is indicated by the RoI curve (gray dashed line) in Figure 108, is a result of very slow droplets being introduced into a cooling environment and appears under both load coniditions. These droplets of small but measurable mass linger and evaporate slowly rather than undergo traditional spray break-up due to aerodynamic effects. An increase in spray penetration after the injection period can also be seen in the experiments which may be related to post injection nozzle dribble and droplet coalescence [172]. The slow evaporation and late combustion of these trailing droplets is the source of the elevated heat release towards the end of the combustion in Figure 107. These increases in spray penetration at the end of injection will be studied in more detailed in future work, but at this stage no connection between the two phenomena can be made.

Although there are no experimental data to compare to, the simulated spray penetration of the production engine can give some indication about the evaporation of the fuel spray. The steady state spray penetration of the simulation is ~6.4mm. An inert ECN Spray A condition at comparable ambient temperatures and injection pressures, but with a lower ambient density stabilizes at ~7.4mm. Increasing ambient densities are one of the main factors for reducing spray penetrations [41]. The spray modelling coefficients of the KH-RT droplet break-up model are identical in both cases. The difference between the setups is that the tabulation suggests different initial droplet sizes and adjusted droplet drag to the condition. Due to the higher injection pressure and ambient density, it is expected that the droplets introduced into the production engine are more distorted than those in an optical engine.

Therefore, in the production engine, the droplet drag coefficient A_{drag} is significantly reduced in comparison to the optical engine.

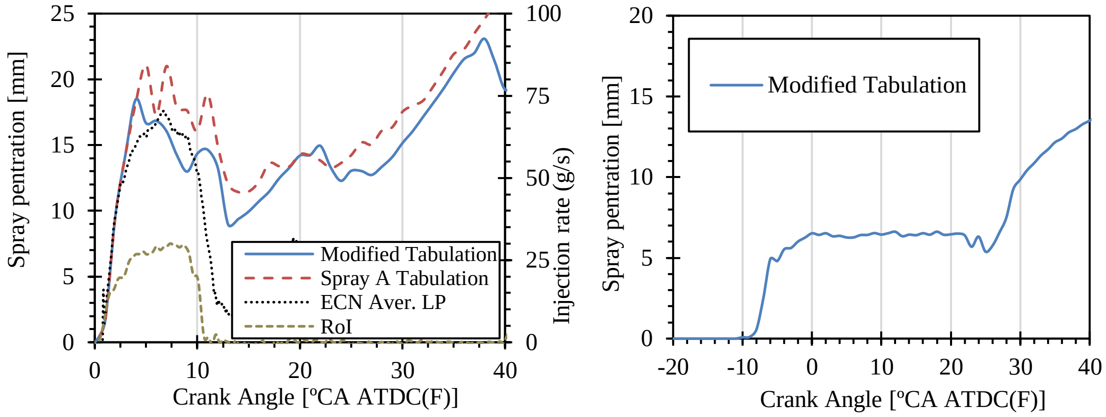

Figure 108: Spray penetration and RoI (only for optical engine) over crank angle

9.4 Summary of the validation of the coefficient table on engine cases

In this chapter, the validation of the previously derived modelling coefficient table on two different LDD DI engines is discussed. Two load conditions, one part-load condition of an optical engine and one full-load condition of a production engine, were simulated using the tabulation derived in chapter 8. The engines represent regular configurations that include a multi-hole injector, swirling ambient flow, large ambient thermodynamic gradients and moving geometries, all aspects not present in Spray A. The answer to the fourth research question, which questions the validity of the coefficient values derived under quiescent conditions for real engine conditions, is:

Answer to research question 4

With modifications to the turbulence model, the coefficient values derived under quiescent conditions are also valid for real engine operating conditions.

The turbulence coefficients derived from the CV – chamber were not directly transferrable to the engine cases. The simulations significantly underestimate early stage heat release and the associated pressure rise.

1. Increasing the dissipation coefficient C_2 in the standard k-ε turbulence model corrects the underestimation of the turbulent mixing by encouraging dissipating affects.

2. The burn rate is accelerated by reducing the turbulent Schmidt number Sc_t (reduction of ratio of eddy viscosity to eddy diffusivity).

These adjustments significantly improved heat release and pressure rise results. Towards the end of the research project, it was discovered that the Spray A conditions would most likely also profit from a reduced turbulent Schmidt numbers, but the investigation of this must be left for future work.

10 Conclusions and future work

A set of modelling approaches that fulfil the requirements of quick turnaround simulations was identified. This means, mainly simulation modelling approaches with low runtimes were selected. The first step was to investigate the validity of the selected models for the Spray A conditions. Using a combined DoE/stochastic process modelling approach to find the modelling coefficients for the selected sub models for a single representative simulation case. The performance of these settings was then tested on a range of differing operating conditions. As expected, the results for varying conditions were not convincing so a DoE method was expanded to a range of other selected operating conditions. A statistical approach allowed conclusions on the behaviour of modelling coefficients with regards to changing boundary conditions. These findings were then used to derive and test a modelling coefficient table that could accurately reproduce key metrics of a large range of related conditions. Finally, the modelling coefficient table was tested on real engine configurations under two load conditions. The key conclusions of each of these steps is given in the following sub-sections.

10.1 Conclusions of the analysis of the mixing regime

The scientific community has not yet found a consensus in which mixing regime the ECN's Spray A should be classified. It is unquestionable that the nominal thermodynamic conditions in the combustion chamber are beyond the critical point of the fuel. The following conclusions gathered from literature discussing the gas phase of the near-nozzle region of the inert Spray A baseline:

1. Trailing and peripheral droplets of the Spray A baseline show clear evidence of surface tension indicating that it is in the classical evaporation regime.
2. Literature shows that a continuous injection of cool liquid likely leads to a local cooling of the ambient air at the spray periphery, which reduces the critical temperature ratio.
3. Droplets injected at the highest temperature (>1000K) and density (>22.8kg/m^3) conditions are entering the trans-critical regime but are still subject to finite transition rate. The question whether the break-up time is shorter than this transition is key but could not be answered within the scope of this work. Further, it was not clear if the local cooling mentioned in the second point is potent enough to prevent a transition.

4. For all Spray A variations besides the ones mentioned in the 3rd point, the classical spray models can be considered valid which answers the first research question. For the few cases with highly elevated thermodynamic this cannot be claimed for certain.

10.2 Conclusions of the modelling coefficient analysis

The second research question was addressed by running a DoE campaign for the inert Spray A baseline, using an automated optimiser to reduce the RMSE between simulations and experiments and then running the found setup of the remaining four inert conditions. The conclusions are:

1. Even when running hundreds of simulations and using a statistical optimiser based on an SPM to minimise the error between simulations and experiments, a single setup to match all conditions could not be identified.
2. The results for the gaseous phase looked promising, but a detailed analysis into microscopic spray characteristics highlighted crucial shortcomings.
3. Due to inherent link between spray penetration and flame lift-off, this is likely to affect accurate predictions of the spatial ignition event negatively.

With the second research question being answered with a confident “no”, the focus shifted to identifying individual simulation coefficients that both successfully matched the experimental data and made physical sense. Seven more DoE campaigns for selected inert and reactive Spray A conditions were performed. They were each post processed to build SPMs and investigated holistically. The simulations based on these statistical models led to promising results:

1. The SPMs highlighted multiple modelling coefficient dependencies on boundary conditions that were explainable with their mathematical expression.
2. The combination of modelling coefficients derived from the SPMs could match all investigated Spray A conditions better than a transfer of the baseline settings.

Another important contribution of this work is the establishment of physical links between the modelling coefficients and the physical changes that occur in swinging operating conditions. Due to the complex nature of fluid dynamic processes in in-cylinder systems and intrinsic multivariable interactions, this was not easy but has the potential to change how engine development will be done in future. The main outcomes are summarised in the following points.

1. The most influential modelling coefficients are C_1, C_2 (standard k-ε model) and KH-B_1 (KH-RT break-up model).
2. The KH-RT break-up model could, without being adjusted, accurately simulate droplet break-up and evaporation under the condition that the initially introduced droplets diameters are adjusted to the boundary condition.
3. Leaning on the Patterson-Reitz droplet introduction method, a tabulation of droplet sizes based on the operating condition was derived. This tabulation followed the physical reasoning that droplet sizes are sensitive to injection pressure and density of the ambient gas. No sensitivity for changing ambient temperatures was detected.
4. The drag scaling coefficient introduced the necessary flexibility of the effects of theoretical droplet deformation in the Putnam drag model, which assumes that all droplets are spherical. The values of these two modelling coefficients appear to be following physically explainable trends and therefore open possibilities of extrapolation into other operating conditions. No sensitivity for changing ambient temperatures was noticed.
5. The auto-ignition coefficient links the complexity of the fuel specific ignition delay process with the simplistic Livengood-Wu auto-ignition model. This coefficient shows a strong sensitivity to all thermodynamic boundary condition swings. Its influence however declines sharply with shortening ignition delays. No sensitivity for changing injection pressure was recorded.

10.3 Conclusions from the tabulation of the modelling coefficients

With the modelling coefficients now characterised on the representative parametric swings of the Spray A condition, the remaining Spray A conditions were simulated, and their coefficient values recorded. The conclusions of this are:

1. The coefficient trends found in the modelling coefficient analysis is extendable to other Spray A boundary conditions and still produce good results.
2. All except the auto-ignition coefficient retain the characteristic found in the modelling coefficient analysis (e.g. droplet sizes reduce with increasing injection pressure etc.).
3. The auto-ignition coefficient had a more complex characteristic that was not highlighted in the swings hence needed some iterative adjustment to adjust the ignition delay.

4. The result is a boundary condition dependant table of coefficient values that can without any further iterations accurately predict any further parametric variation within the investigated range of conditions

10.4 Conclusions of the validation of the table on engine configurations

Next, it was investigated whether an input parameter matrix derived from the tabulated coefficients can be transferred from quiescent experiments to reproduce realistic engine test data. It is acknowledged that there are major differences between the Spray A configuration and a real engine case, hence it is anticipated that some parametric adjustments will have to be made. The conclusions are:

1. The original "Spray A settings" was not directly transferable to the engine cases. The simulations estimated significantly reduced turbulent mixing by suppressing dissipating affects. While this may be appropriate for the governing conditions in the quiescent ECN combustion chamber, it does not represent the more turbulent conditions in the production engine. For this reason, the turbulent Schmidt number Sc_t and the coefficient of dissipation C_2 in the standard k-ε turbulence model had to be adjusted.
2. A "Modified Tabulation", which consists of the "Spray A Settings" with reduced turbulent Schmidt number Sc_t (increased eddy diffusivity) and increased dissipation coefficient C_2, performed better to replicate cylinder pressure, THR and RoHR at both load conditions. For both load conditions, the dissipation coefficients C_2 were identical while turbulent Schmidt number Sc_t was slightly higher for the part-load case.
3. The spray penetration of the optical engine showed good agreement to averaged experimental data. The increase of C_2 increases turbulent mixing. This in turn reduces the spray penetration from the "Spray A Settings" to the "Modified Tabulation" setting. Inert simulations in previous work highlighted that the turbulent Schmidt number only has a minor effect on spray penetration.

10.5 Future work

The validation of the modelling coefficient tables on real engines should be expanded to more than two engine load conditions other geometrical hardware variations. In particular, the initial droplet size table, which currently still relies on the Patterson-Reitz model, should be revisited to allow tabulation against different nozzle sizes. Further, the limited variation in turbulence levels between the available conditions was not enough to clearly identify the pattern for the turbulence dissipation coefficients. More variations are necessary to be able to tabulate this influential coefficient to a change in whatever the fundamental source of its sensitivity is.

An interesting expansion of the findings of this work would be the application on split injection strategies. The table indicates that pilot-main strategies inject fuel in ambient conditions so different (especially in terms of density) that an adaption of the coefficients is unavoidable. Initial trials, which are not included in this thesis confirm these concerns and indicate that different sets of modelling coefficients will be necessary. An even further extension to this would be an implementation of the table into the CFD-software. The vision is a feedback loop of current boundary conditions defining the modelling coefficient of the following time-step without user intervention.

The auto-ignition coefficient proved be difficult to tabulate accurately due to the complexity of chemical interactions. Further, the table derived for the coefficient is based on n-dodecane. The extent of the difference between the values for pump Diesel and n-dodecane needs to be clarified. To my knowledge, no directly comparable experimental data exist to quantify the difference or to tabulate c_{ig} for pump Diesel. The Livengood-Wu model may therefore maybe not be the ideal model for this task. Other, more sophisticated ignition models may be tested to remove this uncertainty.

A detailed analysis into the emissions characteristics was not achieved due to time constraints. In future, another layer of validation of emission characteristics should be included. Initial results obtained in this work were promising but could not be analysed in enough detailed to be discussed in this thesis.

References

[1] B. Georgi, S. Hunkert, J. Liang, M. Willmann, Realizing Future Trends in Diesel Engine Development, SAE International, 1997.

[2] J. Seabrook, M. Rebhan, Y. He, P.A. Battiston, X. He, SCR calibration using design of experiments, MTZ worldwide 71 (2010) 24-28.

[3] J. Sacks, W.J. Welch, T.J. Mitchell, H.P. Wynn, Design and Analysis of Computer Experiments, Statist. Sci. 4 (1989) 409-423.

[4] Y. Pei, M.J. Davis, L.M. Pickett, S. Som, Engine Combustion Network (ECN): Global sensitivity analysis of Spray A for different combustion vessels, Combustion and Flame 162 (2015) 2337-2347.

[5] Y. Pei, R. Shan, S. Som, T. Lu, D. Longman, M.J. Davis, Global Sensitivity Analysis of a Diesel Engine Simulation with Multi-Target Functions, SAE International, 2014.

[6] A. Pandal, R. Payri, J.M. García-Oliver, J.M. Pastor, Optimization of spray break-up CFD simulations by combining Σ-Y Eulerian atomization model with a response surface methodology under diesel engine-like conditions (ECN Spray A), Computers & Fluids 156 (2017) 9-20.

[7] J. Brulatout, F. Garnier, C. Mounaïm-Rousselle, P. Seers, Calibration strategy of diesel-fuel spray atomization models using a design of experiment method, International Journal of Engine Research 17 (2016) 713-731.

[8] J.M. Desantes, J.M. García-Oliver, R. Novella, E.J. Pérez-Sánchez, Application of an unsteady flamelet model in a RANS framework for spray A simulation, Applied Thermal Engineering 117 (2017) 50-64.

[9] J.M. Desantes, J.M. Garcia-Oliver, J.M. Pastor, A. Pandal, A Comparison of Diesel Sprays CFD Modeling Approaches: DDM Versus Σ-Y Eulerian Atomization Model, 26 (2016) 713-737.

[10] G. D’Errico, T. Lucchini, F. Contino, M. Jangi, X.S. Bai, Comparison of well-mixed and multiple representative interactive flamelet approaches for diesel spray combustion modelling, Combustion Theory and Modelling 18 (2014) 65-88.

[11] H. Wang, R.D. Reitz, M. Yao, Comparison of Diesel Combustion CFD Models and Evaluation of the Effects of Model Constants, SAE International, 2012.

[12] J.C. Beale, Modeling fuel injection using Kelvin-Helmholtz/Rayleigh-Taylor hybrid atomization model in KIVA-3V, University of Wisconsin--Madison1999.

[13] D.L. Siebers, Liquid-Phase Fuel Penetration in Diesel Sprays, SAE International, 1998.

[14] J. Seabrook, nCal - Efficient Calibration User Guide Software Release 2018a 1808, 2018.

[15] D. Nsikane, K. Vogiatzaki, R. Morgan, Predictive Engine Simulations based on a novel DoE/RANS approach with coefficient tabulation, IMechE, Fuel Systems-Engines, London, 2018.

[16] D. Nsikane, M., K. Vogiatzaki, R.E. Morgan, M. Heikal, K. Mustafa, A. Ward, N. Winder, Novel approach for adaptive coefficient tuning for the simulation of evaporating

high-speed sprays injected into a high temperature and pressure environment, International Journal of Engine Research - In Print (2019).

[17] D. Nsikane, K. Vogiatzaki, R. Morgan, K. Mustafa, A. Ward, Predictive CFD Auto-Tuning Approach for In-Cylinder Simulations of Two Small-Bore LDD Engines, SAE International, 2019.

[18] M. Linne, Imaging in the optically dense regions of a spray: A review of developing techniques, Progress in Energy and Combustion Science 39 (2013) 403-440.

[19] A. Kastengren, J. Ilavsky, J.P. Viera, R. Payri, D.J. Duke, A. Swantek, F.Z. Tilocco, N. Sovis, C.F. Powell, Measurements of droplet size in shear-driven atomization using ultra-small angle x-ray scattering, International Journal of Multiphase Flow 92 (2017) 131-139.

[20] G.M. Magnotti, C.L. Genzale, Detailed assessment of diesel spray atomization models using visible and X-ray extinction measurements, International Journal of Multiphase Flow 97 (2017) 33-45.

[21] Z. Falgout, M. Rahm, D. Sedarsky, M. Linne, Gas/fuel jet interfaces under high pressures and temperatures, Fuel 168 (2016) 14-21.

[22] Z. Falgout, M. Rahm, Z. Wang, M. Linne, Evidence for supercritical mixing layers in the ECN Spray A, Proceedings of the Combustion Institute 35 (2015) 1579-1586.

[23] R. Payri, J.P. Viera, H. Wang, L.-M. Malbec, Velocity field analysis of the high density, high pressure diesel spray, International Journal of Multiphase Flow 80 (2016) 69-78.

[24] Y. Chi, E. Kim, Measurement of Droplet Size Distribution of Transient Diesel Spray, SAE International, 1993.

[25] J. Jeon, S. Moon, Ambient density effects on initial flow breakup and droplet size distribution of hollow-cone sprays from outwardly-opening GDI injector, Fuel 211 (2018) 572-581.

[26] J.G. Gupta, A.K. Agarwal, Macroscopic and Microscopic Spray Characteristics of Diesel and Karanja Biodiesel Blends, SAE International, 2016.

[27] S. Tonini, M. Gavaises, A. Theodorakakos, The role of droplet fragmentation in high-pressure evaporating diesel sprays, International Journal of Thermal Sciences 48 (2009) 554-572.

[28] C. Crua, J. Manin, L.M. Pickett, On the transcritical mixing of fuels at diesel engine conditions, Fuel 208 (2017) 535-548.

[29] J. Bellan, Supercritical (and subcritical) fluid behavior and modeling: drops, streams, shear and mixing layers, jets and sprays, Progress in Energy and Combustion Science 26 (2000) 329-366.

[30] R.N. Dahms, Understanding the breakdown of classic two-phase theory and spray atomization at engine-relevant conditions, Physics of Fluids 28 (2016) 042108.

[31] C. Chauveau, P. Dagaut, I. GÖKalp, M. Cathonnet, Vaporization And Oxidation Of Liquid Fuel Droplets At High Temperature And High Pressure: Application To N-alkanes And Vegetable Oil Methyl Esters Au - Morin ∗ , Céline, Combustion Science and Technology 176 (2004) 499-529.

[32] M. Wensing, T. Vogel, G. Götz, Transition of diesel spray to a supercritical state under engine conditions, International Journal of Engine Research 17 (2015) 108-119.

[33] W.T. Chung, P.C. Ma, M. Ihme, Examination of diesel spray combustion in supercritical ambient fluid using large-eddy simulations, International Journal of Engine Research (2019) 1468087419868388.

[34] C.-N. Yeh, T. Kamimoto, S. Kobori, H. Kosaka, 2-D Imaging of Fuel Vapor Concentration in a Diesel Spray via Exciplex-Based Fluorescence Technique, SAE International, 1993.

[35] T. Kamimoto, H. Yokota, H. Kobayashi, Effect of High Pressure Injection on Soot Formation Processes in a Rapid Compression Machine to Simulate Diesel Flames, SAE International, 1987.

[36] M. Hawi, H. Kosaka, S. Sato, T. Nagasawa, A. Elwardany, M. Ahmed, Effect of injection pressure and ambient density on spray characteristics of diesel and biodiesel surrogate fuels, Fuel 254 (2019) 115674.

[37] K.R. Browne, I.M. Partridge, G. Greeves, Fuel Property Effects on Fuel/Air Mixing in an Experimental Diesel Engine, SAE International, 1986.

[38] C. Espey, J.E. Dec, The Effect of TDC Temperature and Density on the Liquid-Phase Fuel Penetration in a D. I. Diesel Engine*, SAE International, 1995.

[39] H. Kahila, A. Wehrfritz, O. Kaario, M. Ghaderi Masouleh, N. Maes, B. Somers, V. Vuorinen, Large-eddy simulation on the influence of injection pressure in reacting Spray A, Combustion and Flame 191 (2018) 142-159.

[40] L.M. Pickett, J. Manin, C.L. Genzale, D.L. Siebers, M.P.B. Musculus, C.A. Idicheria, Relationship Between Diesel Fuel Spray Vapor Penetration/Dispersion and Local Fuel Mixture Fraction, SAE International Journal of Engines 4 (2011) 764-799.

[41] J.D. Naber, D.L. Siebers, Effects of Gas Density and Vaporization on Penetration and Dispersion of Diesel Sprays, SAE International, 1996.

[42] H. Hiroyasu, M. Arai, Structures of Fuel Sprays in Diesel Engines, SAE International, 1990.

[43] J. Arrègle, J.V. Pastor, S. Ruiz, The Influence of Injection Parameters on Diesel Spray Characteristics, SAE International, 1999.

[44] F. Payri, J.M. Desantes, J. Arrégle, Characterization of D.I. Diesel Sprays in High Density Conditions, SAE International, 1996.

[45] L.M. Pickett, C.L. Genzale, G. Bruneaux, L.-M. Malbec, L. Hermant, C. Christiansen, J. Schramm, Comparison of Diesel Spray Combustion in Different High-Temperature, High-Pressure Facilities, SAE International Journal of Engines 3 (2010) 156-181.

[46] J.V. Pastor, R. Payri, J.M. Garcia-Oliver, J.-G. Nerva, Schlieren Measurements of the ECN-Spray A Penetration under Inert and Reacting Conditions, SAE International, 2012.

[47] L.M. Pickett, D.L. Siebers, C.A. Idicheria, Relationship Between Ignition Processes and the Lift-Off Length of Diesel Fuel Jets, SAE International, 2005.

[48] L.M. Pickett, D.L. Siebers, Soot in diesel fuel jets: effects of ambient temperature, ambient density, and injection pressure, Combustion and Flame 138 (2004) 114-135.

[49] D.L. Siebers, B. Higgins, Flame Lift-Off on Direct-Injection Diesel Sprays Under Quiescent Conditions, SAE International, 2001.

[50] B. Higgins, D.L. Siebers, Measurement of the Flame Lift-Off Location on DI Diesel Sprays Using OH Chemiluminescence, SAE International, 2001.

[51] J. Benajes, R. Payri, M. Bardi, P. Martí-Aldaraví, Experimental characterization of diesel ignition and lift-off length using a single-hole ECN injector, Applied Thermal Engineering 58 (2013) 554-563.

[52] I.V. Roisman, L. Araneo, C. Tropea, Effect of ambient pressure on penetration of a diesel spray, International Journal of Multiphase Flow 33 (2007) 904-920.

[53] N. Peters, Turbulent Combustion, Cambridge University Press2000.

[54] J.M. Garcia-Oliver, J.M. Pastor, A. Pandal, N. Trask, E. Baldwin, D.P. Schmidt, Diesel Spray CFD Simulations Based on the Σ-Y Eulerian Atomization Model, 23 (2013) 71-95.

[55] F.J. Salvador, J. Gimeno, J.M. Pastor, P. Martí-Aldaraví, Effect of turbulence model and inlet boundary condition on the Diesel spray behavior simulated by an Eulerian Spray Atomization (ESA) model, International Journal of Multiphase Flow 65 (2014) 108-116.

[56] M. Vujanović, Z. Petranović, W. Edelbauer, J. Baleta, N. Duić, Numerical modelling of diesel spray using the Eulerian multiphase approach, Energy Conversion and Management 104 (2015) 160-169.

[57] D. Zuzio, J.-L. Estivalèzes, B. DiPierro, An improved multiscale Eulerian–Lagrangian method for simulation of atomization process, Computers & Fluids 176 (2018) 285-301.

[58] J. Capecelatro, O. Desjardins, An Euler–Lagrange strategy for simulating particle-laden flows, Journal of Computational Physics 238 (2013) 1-31.

[59] G. Borghesi, E. Mastorakos, R.S. Cant, Complex chemistry DNS of n-heptane spray autoignition at high pressure and intermediate temperature conditions, Combustion and Flame 160 (2013) 1254-1275.

[60] A. Viggiano, Exploring the effect of fluid dynamics and kinetic mechanisms on n-heptane autoignition in transient jets, Combustion and Flame 157 (2010) 328-340.

[61] E.R. Hawkes, R. Sankaran, J.C. Sutherland, J.H. Chen, Scalar mixing in direct numerical simulations of temporally evolving plane jet flames with skeletal CO/H2 kinetics, Proceedings of the Combustion Institute 31 (2007) 1633-1640.

[62] Y. Pei, E.R. Hawkes, S. Kook, A Comprehensive Study of Effects of Mixing and Chemical Kinetic Models on Predictions of n-heptane Jet Ignitions with the PDF Method, Flow, Turbulence and Combustion 91 (2013) 249-280.

[63] S. Bhattacharjee, D.C. Haworth, Simulations of transient n-heptane and n-dodecane spray flames under engine-relevant conditions using a transported PDF method, Combustion and Flame 160 (2013) 2083-2102.

[64] C. Gong, M. Jangi, X.-S. Bai, Large eddy simulation of n-Dodecane spray combustion in a high pressure combustion vessel, Applied Energy 136 (2014) 373-381.

[65] A. Irannejad, A. Banaeizadeh, F. Jaberi, Large eddy simulation of turbulent spray combustion, Combustion and Flame 162 (2015) 431-450.

[66] A. Irannejad, F. Jaberi, Large eddy simulation of turbulent spray breakup and evaporation, International Journal of Multiphase Flow 61 (2014) 108-128.

[67] Y. Pei, B. Hu, S. Som, Large-Eddy Simulation of an n-Dodecane Spray Flame Under Different Ambient Oxygen Conditions, Journal of Energy Resources Technology 138 (2016) 032205-032205-032210.

[68] Y. Pei, S. Som, E. Pomraning, P.K. Senecal, S.A. Skeen, J. Manin, L.M. Pickett, Large eddy simulation of a reacting spray flame with multiple realizations under compression ignition engine conditions, Combustion and Flame 162 (2015) 4442-4455.

[69] Y. Pei, S. Som, P. Kundu, G.M. Goldin, Large Eddy Simulation of a Reacting Spray Flame under Diesel Engine Conditions, SAE International, 2015.

[70] C.C. K. Vogiatzaki , R. Morgan , M.R. Heikal, A study of the controlling parameters of fuel air mixture formationfor ECN Spray A, ILASS–Europe 2017, 28th Conference on Liquid Atomization and Spray Systems, Valencia, Spain, 2017.

[71] O.T. Kaario, V. Vuorinen, H. Kahila, H.G. Im, M. Larmi, The effect of fuel on high velocity evaporating fuel sprays: Large-Eddy simulation of Spray A with various fuels, International Journal of Engine Research (2019) 1468087419854235.

[72] Y. Pei, E.R. Hawkes, M. Bolla, S. Kook, G.M. Goldin, Y. Yang, S.B. Pope, S. Som, An analysis of the structure of an n-dodecane spray flame using TPDF modelling, Combustion and Flame 168 (2016) 420-435.

[73] Y. Pei, E.R. Hawkes, S. Kook, G.M. Goldin, T. Lu, Modelling n-dodecane spray and combustion with the transported probability density function method, Combustion and Flame 162 (2015) 2006-2019.

[74] Y. Pei, E.R. Hawkes, S. Kook, Transported probability density function modelling of the vapour phase of an n-heptane jet at diesel engine conditions, Proceedings of the Combustion Institute 34 (2013) 3039-3047.

[75] C.K. Blomberg, L. Zeugin, S.S. Pandurangi, M. Bolla, K. Boulouchos, Y.M. Wright, Modeling Split Injections of ECN “Spray A” Using a Conditional Moment Closure Combustion Model with RANS and LES, SAE International Journal of Engines 9 (2016) 2107-2119.

[76] M.M. Ameen, J. Abraham, RANS and LES Study of Lift-Off Physics in Reacting Diesel Jets, SAE International, 2014.

[77] A. Wehrfritz, O. Kaario, V. Vuorinen, B. Somers, Large Eddy Simulation of n-dodecane spray flames using Flamelet Generated Manifolds, Combustion and Flame 167 (2016) 113-131.

[78] J. Tillou, J.B. Michel, C. Angelberger, C. Bekdemir, D. Veynante, Large-Eddy Simulation of Diesel Spray Combustion with Exhaust Gas Recirculation, Oil Gas Sci. Technol. – Rev. IFP Energies nouvelles 69 (2014) 155-165.

[79] C. Bekdemir, L.M.T. Somers, L.P.H. de Goey, J. Tillou, C. Angelberger, Predicting diesel combustion characteristics with Large-Eddy Simulations including tabulated chemical kinetics, Proceedings of the Combustion Institute 34 (2013) 3067-3074.

[80] W.P. Jones, B.E. Launder, The prediction of laminarization with a two-equation model of turbulence, International Journal of Heat and Mass Transfer 15 (1972) 301-314.

[81] B.E. Launder, Turbulence Modelling for CFD. By D. C. WILCOX. DCW Industries Inc., 1993. 460pp. $75, Journal of Fluid Mechanics 289 (1995) 406-407.

[82] B.E. Launder, D.B. Spalding, The numerical computation of turbulent flows, Computer Methods in Applied Mechanics and Engineering 3 (1974) 269-289.

[83] K. Puduppakkam, C. Naik, E. Meeks, C. Krenn, R. Kroiss, J. Gelbmann, G. Pessl, Predictive Combustion and Emissions Simulations for a High Performance Diesel Engine Using a Detailed Fuel Combustion Model, SAE International, 2014.

[84] M. Bolla, T. Gudmundsson, Y.M. Wright, K. Boulouchos, Simulations of Diesel Sprays Using the Conditional Moment Closure Model, SAE International Journal of Engines, SAE International, 2013, pp. 1249-1261.

[85] M.P.B. Musculus, K. Kattke, Entrainment Waves in Diesel Jets, SAE International Journal of Engines, SAE International, 2009, pp. 1170-1193.

[86] S. Som, G. D'Errico, D. Longman, T. Lucchini, Comparison and Standardization of Numerical Approaches for the Prediction of Non-reacting and Reacting Diesel Sprays, SAE International, 2012.

[87] S. Som, S.K. Aggarwal, Effects of primary breakup modeling on spray and combustion characteristics of compression ignition engines, Combustion and Flame 157 (2010) 1179-1193.

[88] R.A. Mugele, H.D. Evans, Droplet Size Distribution in Sprays, Industrial & Engineering Chemistry 43 (1951) 1317-1324.

[89] A.B. Liu, D. Mather, R.D. Reitz, Modeling the Effects of Drop Drag and Breakup on Fuel Sprays, SAE International, 1993.

[90] R. Payri, J.P. Viera, Y. Pei, S. Som, Experimental and numerical study of lift-off length and ignition delay of a two-component diesel surrogate, Fuel 158 (2015) 957-967.

[91] R. Clift, J.R. Grace, M.E. Weber, Bubbles, drops and particles, New York (N.Y.) : Academic press1978.

[92] L. Schiller, Z. Naumann, A Drag Coefficient Correlation, VDI Zeitung Vol. 77 (1935) 318-320.

[93] N. Frossling, Evaporation, Heat Transfer, and Velocity Distribution in Two-Dimensional and Rotationally Symmetrical Laminar Boundary-Layer Flow, N.A.C.A. , 1956.

[94] S. D.B., The Combustion of Liquid Fuels, 4th Symposium (International) on Combustion, Williams & Wilkins, Baltimore, 1953, pp. pp. 847-864.

[95] J.S.a.L. Chin, A.H., The Role of the Heat-up Period in Fuel Drop Evaporation, Int. J. Turbo Jet Engines vol. 2, (1985) pp. 315-325.

[96] A. Varna, A. Wehrfritz, E. R. Hawkes, M. J. Cleary, T. Lucchini, G. D'Errico, S. Kook, Q. N. Chan, Application of a multiple mapping conditioning mixing model to ECN Spray A, Proceedings of the Combustion Institute (2018).

[97] P. Kundu, Y. Pei, M. Wang, R. Mandhapati, S. Som, Evaluation of Turbulence-Chemistry interaction under Diesel Engine Conditions with Multi-Flamelet RIF Model, Atomization and Spray 24 (2014) 779-800.

[98] J. Villermaux, J.C. Devillon. Represéntation de la coalescence et de la redispersion des domaines de ségrégation dans un fluide par un modéle d'interaction phénoménologique. In: editor^editors. 2nd Int. Symp. on Chemical Reaction Engineering; 1972; New York: ISCRE. p. 1–13.

[99] J. Janicka, W. Kolbe, W. Kollmann, Closure of the transport equation for the probability density function of turbulent scalar fields J. Non-Equilib. Thermodyn 4 (1979) 47–66.

[100] S. Subramaniam, S.B. Pope, A mixing model for turbulent reactive flows based on Euclidean minimum spanning trees, Combustion and Flame 115 (1998) 487-514.

[101] E.R. Hawkes, O. Chatakonda, H. Kolla, A.R. Kerstein, J.H. Chen, A petascale direct numerical simulation study of the modelling of flame wrinkling for large-eddy simulations in intense turbulence, Combustion and Flame 159 (2012) 2690-2703.

[102] O. Chatakonda, E.R. Hawkes, A.J. Aspden, A.R. Kerstein, H. Kolla, J.H. Chen, On the fractal characteristics of low Damköhler number flames, Combustion and Flame 160 (2013) 2422-2433.

[103] S. Som, Senecal, P.K., Pomraning, E., Comparison of RANS and LES Turbulence Models against Constant Volume Diesel Experiments, ILASS Americas, 24th Annual Conference on Liquid Atomization and Spray Systems, San Antonio, TX, 2012.

[104] V. Knop, J.-B. Michel, O. Colin, On the use of a tabulation approach to model auto-ignition during flame propagation in SI engines, Applied Energy 88 (2011) 4968-4979.

[105] S. Gövert, D. Mira, J.B.W. Kok, M. Vázquez, G. Houzeaux, Turbulent combustion modelling of a confined premixed jet flame including heat loss effects using tabulated chemistry, Applied Energy 156 (2015) 804-815.

[106] M. Bardi, R. Payri, L.M. Malbec, G. Bruneaux, L.M. Pickett, J. Manin, T. Bazyn, C.L. Genzale, Engine Combustion Network: Comparison of Spray Development, Vaporization and Combustion in Different Combustion Vessels, 22 (2012) 807-842.

[107] M. Meijer, B. Somers, J. Johnson, J. Naber, S.-Y. Lee, L.M. Malbec, G. Bruneaux, L.M. Pickett, M. Bardi, R. Payri, T. Bazyn, Engine Combustion Network (ECN): Characterization and Comparison of Boundary Conditions for different Combustion Vessels, Atomization and Sprays 22 (2012) 777-806.

[108] C.N. Yeh, T. Kamimoto, S. Kobori, H. Kosaka, 2-D Imaging of Fuel Vapor Concentration in a Diesel Spray via Exciplex-Based Fluorescence Technique, SAE International, 1993.

[109] F. Poursadegh, O. Bibik, B. Yraguen, C.L. Genzale, A multispectral, extinction-based diagnostic for drop sizing in optically dense diesel sprays, International Journal of Engine Research (2019) 1468087419866034.

[110] J. Manin, M. Bardi, L.M. Pickett, R. Payri, Boundary condition and fuel composition effects on injection processes of high-pressure sprays at the microscopic level, International Journal of Multiphase Flow 83 (2016) 267-278.

[111] R. Payri, J.P. Viera, V. Gopalakrishnan, P.G. Szymkowicz, The effect of nozzle geometry over the evaporative spray formation for three different fuels, Fuel 188 (2017) 645-660.

[112] M. Bardi, R. Payri, L.M.C. Malbec, G. Bruneaux, L.M. Pickett, J. Manin, T. Bazyn, C.L. Genzale, Engine Combustion Network: Comparison of Spray Development, Vaporization and Combustion in Different Combustion Vessels, Atomization and Spray 22 (2012) 807-842.

[113] R. Payri, J.M. García-Oliver, M. Bardi, J. Manin, Fuel temperature influence on diesel sprays in inert and reacting conditions, Applied Thermal Engineering 35 (2012) 185-195.

[114] D.L. Siebers, B. Higgins, L. Pickett, Flame Lift-Off on Direct-Injection Diesel Fuel Jets: Oxygen Concentration Effects, SAE International, 2002.

[115] R. Payri, F.J. Salvador, J. Manin, A. Viera, Diesel ignition delay and lift-off length through different methodologies using a multi-hole injector, Applied Energy 162 (2016) 541-550.

[116] R. Payri, J.P. Viera, V. Gopalakrishnan, P.G. Szymkowicz, The effect of nozzle geometry over ignition delay and flame lift-off of reacting direct-injection sprays for three different fuels, Fuel 199 (2017) 76-90.

[117] L.M. Pickett, D.L. Siebers, Fuel Effects on Soot Processes of Fuel Jets at DI Diesel Conditions, SAE International, 2003.

[118] D.L. Siebers, L.M. Pickett. Injection Pressure and Orifice Diameter Effects on Soot in DI Diesel Fuel Jets. In: J.H. Whitelaw, F. Payri, C. Arcoumanis, J.M. Desantes, editor^editors. Thermo- and Fluid Dynamic Processes in Diesel Engines 2; 2004// 2004; Berlin, Heidelberg: Springer Berlin Heidelberg. p. 109-132.

[119] L.M. Pickett, D.L. Siebers, Non-Sooting, Low Flame Temperature Mixing-Controlled DI Diesel Combustion, SAE International, 2004.

[120] C.A. Idicheria, L.M. Pickett, Soot Formation in Diesel Combustion under High-EGR Conditions, SAE International, 2005.

[121] S.S. Pandurangi, M. Bolla, Y.M. Wright, K. Boulouchos, S.A. Skeen, J. Manin, L.M. Pickett, Onset and progression of soot in high-pressure n-dodecane sprays under diesel engine conditions, International Journal of Engine Research 18 (2016) 436-452.

[122] G.B. L. Pickett, R. Payri, Engine Combustion Network, http:// www.ca.sandia.gov/ecn 2014.

[123] E.C. Network, Data Search Utility. (accessed 07/03 2017).

[124] Engine Combustion Network, "Spray A" and "Spray B" Operating Conditions. (accessed 26/02/2017 2017).

[125] S.N. Laboratory, The Engine Combustion Network. (accessed 09/03/2017 2017).

[126] C.M. Termicos, Virtual ROI Generator. (accessed 25/04/2017 2017).

[127] R. Payri, F.J. Salvador, J. Gimeno, G. Bracho, A new methodology for correcting the signal cumulative phenomenon on injection rate measurements, Experimental Techniques 32 (2008) 46-49.

[128] C. Mauger, L. Mees, M. Michard, A. Azouzi, S. Valette, Shadowgraph, Schlieren and interferometry in a 2D cavitating channel flow, Experiments in Fluids 53 (2012) 1895–1913.

[129] E. Winklhofer, E. Kull, E. Kelz, M. A, Comprehensive Hydraulic and Flow Field Documentation in Model Throttle Experiment under Cavitation Conditions, ILASS-Europe 2001, Zurich, 2001.

[130] C. Arcoumanis, H. Flora, M. Gavaises, N. Kampanis, R. Horrocks, Investigation of Cavitation in a Vertical Multi-Hole Injector, SAE International, 1999.

[131] C. Crua, M.R. Heikal, M.R. Gold, Microscopic imaging of the initial stage of diesel spray formation, Fuel 157 (2015) 140-150.

[132] L.M. Pickett, J. Manin, A. Kastengren, C. Powell, Comparison of Near-Field Structure and Growth of a Diesel Spray Using Light-Based Optical Microscopy and X-Ray Radiography, SAE International Journal of Engines 7 (2014) 1044-1053.

[133] L. M. Pickett, C. Genzale, J. Manin, Uncertainty quantification for liquid penetration of evaporating sprays at diesel-like conditions, 2015.

[134] L.M. Pickett, S. Kook, T.C. Williams, Visualization of Diesel Spray Penetration, Cool-Flame, Ignition, High-Temperature Combustion, and Soot Formation Using High-Speed Imaging, SAE International Journal of Engines 2 (2009) 439-459.

[135] R. Payri, F.J. Salvador, G. Bracho, A. Viera, Differences between single and double-pass schlieren imaging on diesel vapor spray characteristics, Applied Thermal Engineering 125 (2017) 220-231.

[136] M. Bardi, R. Payri, L.M.C. Malbec, G. Bruneaux, L.M. Pickett, J. Manin, T. Bazyn, C.L. Genzale, ENGINE COMBUSTION NETWORK: COMPARISON OF SPRAY DEVELOPMENT, VAPORIZATION, AND COMBUSTION IN DIFFERENT COMBUSTION VESSELS, 22 (2012) 807-842.

[137] R. Payri, J.M. García-Oliver, T. Xuan, M. Bardi, A study on diesel spray tip penetration and radial expansion under reacting conditions, Applied Thermal Engineering 90 (2015) 619-629.

[138] R.N. Dahms, J. Manin, L.M. Pickett, J.C. Oefelein, Understanding high-pressure gas-liquid interface phenomena in Diesel engines, Proceedings of the Combustion Institute 34 (2013) 1667-1675.

[139] R.N. Dahms, G.A. Paczko, S.A. Skeen, L.M. Pickett, Understanding the ignition mechanism of high-pressure spray flames, Proceedings of the Combustion Institute 36 (2017) 2615-2623.

[140] L.-M. Malbec, J. Egúsquiza, G. Bruneaux, M. Meijer, Characterization of a Set of ECN Spray A Injectors: Nozzle to Nozzle Variations and Effect on Spray Characteristics, (2013).

[141] S.A. Skeen, J. Manin, L.M. Pickett, Simultaneous formaldehyde PLIF and high-speed schlieren imaging for ignition visualization in high-pressure spray flames, Proceedings of the Combustion Institute 35 (2015) 3167-3174.

[142] S. Busch, Engine Combustion Network - Small-bore diesel engine, https://ecn.sandia.gov/engines/small-bore-diesel-engine/. (accessed 27.06.2019.

[143] K. Zha, S. Busch, P.C. Miles, S. Wijeyakulasuriya, S. Mitra, P.K. Senecal, Characterization of Flow Asymmetry During the Compression Stroke Using Swirl-Plane

PIV in a Light-Duty Optical Diesel Engine with the Re-entrant Piston Bowl Geometry, SAE International Journal of Engines, SAE International, 2015, pp. 1837-1855.

[144] S. Busch, K. Zha, P.C. Miles, A. Warey, F. Pesce, R. Peterson, A. Vassallo, Experimental and Numerical Investigations of Close-Coupled Pilot Injections to Reduce Combustion Noise in a Small-Bore Diesel Engine, SAE International Journal of Engines, SAE International, 2015, pp. 660-678.

[145] B.R. Petersen, I.W. Ekoto, P.C. Miles, An Investigation into the Effects of Fuel Properties and Engine Load on UHC and CO Emissions from a Light-Duty Optical Diesel Engine Operating in a Partially Premixed Combustion Regime, SAE International Journal of Engines, SAE International, 2010, pp. 38-55.

[146] D. Sahoo, B. Petersen, P.C. Miles, Measurement of Equivalence Ratio in a Light-Duty Low Temperature Combustion Diesel Engine by Planar Laser Induced Fluorescence of a Fuel Tracer, SAE International Journal of Engines, SAE International, 2011, pp. 2312-2325.

[147] I.W. Ekoto, W.F. Colban, P.C. Miles, S.W. Park, D.E. Foster, R.D. Reitz, U. Aronsson, Ö. Andersson, UHC and CO Emissions Sources from a Light-Duty Diesel Engine Undergoing Dilution-Controlled Low-Temperature Combustion, SAE International Journal of Engines, Consiglio Nazionale delle Ricerche, 2009, pp. 411-430.

[148] D. Sahoo, P.C. Miles, J. Trost, A. Leipertz, The Impact of Fuel Mass, Injection Pressure, Ambient Temperature, and Swirl Ratio on the Mixture Preparation of a Pilot Injection, SAE International Journal of Engines, SAE International, 2013, pp. 1716-1730.

[149] P.C. Miles, D. Sahoo, S. Busch, J. Trost, A. Leipertz, Pilot Injection Ignition Properties Under Low-Temperature, Dilute In-Cylinder Conditions, SAE International Journal of Engines, SAE International, 2013, pp. 1888-1907.

[150] S. Busch, K. Zha, P.C. Miles, Investigations of Closely Coupled Pilot and Main Injections as a Means to Reduce Combustion Noise, THIESEL 2014 Valencia, Spain, 2014.

[151] S. Busch, P.C. Miles, Parametric study of injection rates with solenoid injectors in an injection quantity and rate measuring device, ASME, Journal of Engineering for Gas Turbines and Power, 2014.

[152] G. Li, S.M. Sapsford, R.E. Morgan, CFD Simulation of DI Diesel Truck Engine Combustion Using VECTIS, SAE International, 2000.

[153] A. Lefebvre, Atomization and Sprays, Taylor & Francis1988.

[154] A. Putnam, Integratable Form of Droplet Drag Coefficient, J. Am. Rocket Soc., 1961, pp. 1467-4798.

[155] J.C. Livengood, P.C. Wu, Correlation of autoignition phenomena in internal combustion engines and rapid compression machines, Symposium (International) on Combustion 5 (1955) 347-356.

[156] C. Chen, M.E.A. Bardsley, R.J.R. Johns, Two-Zone Flamelet Combustion Model, SAE International, 2000.

[157] M. Metghalchi, J.C. Keck, Burning velocities of mixtures of air with methanol, isooctane, and indolene at high pressure and temperature, Combustion and Flame 48 (1982) 191-210.

[158] Ö.L. Gülder, Turbulent premixed flame propagation models for different combustion regimes, Symposium (International) on Combustion 23 (1991) 743-750.

[159] G.L. Borman, J.H. Johnson, Unsteady Vaporization Histories and Trajectories of Fuel Drops Injected into Swirling Air, SAE International, 1962.

[160] J.S. Chin, A.H. Lefebvre, The Role of the Heat-up Period in Fuel Drop Evaporation, International Journal of Turbo and Jet Engines, 1985, pp. 315.

[161] R. Software, Vectis Documentation Version 2015.2, (2015).

[162] R.D. Reitz, Modeling atomization processes in high-pressure vaporizing sprays, Atomisation Spray Technology 3 (1987) 309-337.

[163] M.A. Patterson, R.D. Reitz, Modeling the Effects of Fuel Spray Characteristics on Diesel Engine Combustion and Emission, SAE International, 1998.

[164] R. Software, VECTIS User Manual, Version 2017.1b1, 2017.

[165] D.B. Spalding, A novel finite difference formulation for differential expressions involving both first and second derivatives, International Journal for Numerical Methods in Engineering 4 (1972) 551-559.

[166] B.F. Magnussen, B.H. Hjertager, On mathematical modeling of turbulent combustion with special emphasis on soot formation and combustion, Symposium (International) on Combustion 16 (1977) 719-729.

[167] D.R. Stull, H. Prophet, JANAF thermochemical tables, U.S. Dept. of Commerce, National Bureau of Standards, (1971).

[168] D.M. Nsikane, K. Mustafa, A. Ward, R. Morgan, D. Mason, M. Heikal, Statistical Approach on Visualizing Multi-Variable Interactions in a Hybrid Breakup Model under ECN Spray Conditions, SAE International Journal of Engines 10 (2017).

[169] D. Nsikane, K. Vogiatzaki, R. Morgan, M. Heikal, Assessment of the performance of conventional spray models under high pressure and high temperature conditions using a “Design of Experiments” approach, ICLASS 2018, 14th Triennial International Conference on Liquid Atomization and Spray Systems, Chicago, USA, 2018.

[170] D. Nsikane, K. Vogiatzaki, R. Morgan, K. Mustafa, A. Ward, Predictive CFD Auto-Tuning Approach For In-Cylinder EU6 LDD DI Engine, SAE International, 2019.

[171] M.A.-H.M. Nawi, N. Uwa, Y. Ueda, Y. Nada, Y. Kidoguchi, Droplets Behavior and Evaporation of Diesel Spray Affected by Ambient Density after Pilot Injection, Society of Automotive Engineers of Japan, 2015.

[172] D. Sykes, G. de Sercey, M. Gold, R. Pearson, C. Crua, Visual Analyses of End of Injection Liquid Structures and the Behaviour of Nozzle Surface-Bound Fuel in a Direct Injection Diesel Engine, SAE International, 2019.

Appendix

Analysis of mixing regime of inert baseline Spray A

A frequently discussed topic surrounding the Spray A configuration is whether it is supercritical or not. As discussed in the literature review in section 3.1.1.3, the surrounding air unquestionably is beyond the critical point of the fuel. The question is whether this also means that the injected cool spray must be classified in diffusive mixing regime. Should this be the case, then the industry standard classical break-up models provided in the used software package are not valid. The literature mentioned in section 3.1.1.3 discusses multiple experimental efforts to visualise individual droplets near the nozzle that have tentatively identified temporary surface tension effects even for the highest ambient temperature and pressure effects.

Since the experimental acquisition of conclusive data is very difficult for these conditions, a numerical approach to characterising the near-nozzle gas phase temperature is shown in this chapter. The approach assumes that even at ambient conditions far beyond the critical point of the fuel, there exists a transitional period in which the spray remains subcritical as it extracts energy from the surrounding air. The hypothesis is that the continuous injection of a cool liquid spray into supercritical ambient conditions will produce subcritical local conditions around the plume due to finite heat transfer rates.

The left side of shows contour plots of ambient temperature of the baseline (KP1) from the start of injection up to the steady state phase (spray penetration stabilising) in 0.1ms increments. It also shows a qualitative representation of the droplet mean diameter and a quantitative contour plot of the droplet temperatures. Just after the start of injection (first row, 0.05 ASOI), the liquid jet starts reducing the ambient temperature around 5mm downstream the nozzle. The droplets in this area begin to rapidly heat up by absorbing thermal energy from the surrounding air leading to their evaporation. Within this low temperature zone, some following droplets begin to coalesce instead of evaporating. These large droplets then penetrate through the surrounding air while evaporating downstream relatively slowly. Despite these cases being under evaporating conditions, some parallels can be drawn to the process described by Magnotti *et al* in [20] where under non-evaporating conditions shortly after injection some degree of droplet coalescence was observed. It is assumed that once the cooled initial stagnant air is removed by liquid jet induced turbulence, the low temperature zone stabilizes at higher temperatures preventing any further coalescing.

As of 0.3ms ASOI, the steady state is established, and the droplets complete their break-up and evaporation process around 10mm downstream the nozzle. These images indicate that due to high droplet velocities, the droplets only begin to show considerable heating around 4mm downstream presumably due to thermal inertia. This is the first important point supporting the conclusions by Crua *et al* in [28] that essentially only droplets further downstream might reach to critical temperatures. A further investigation into the development of the temperature conditions of the gas phase around the spray injection region is shown on the right side of Figure 109. The radial temperature distributions of incremental slices at given time-steps are plotted as a wireframe. The temperature is normalised with n-dodecane’s critical temperature to match the characterisation previously shown in section 3.1.1.3. The significance of this graph is that a local cooling along the centre axis leading to a drop of Tr is observable. The consequence is effectively a shift to the left of the location of the key point in Figure 19 for the transient phase of the injection process. These findings also apply for all other invested key points.

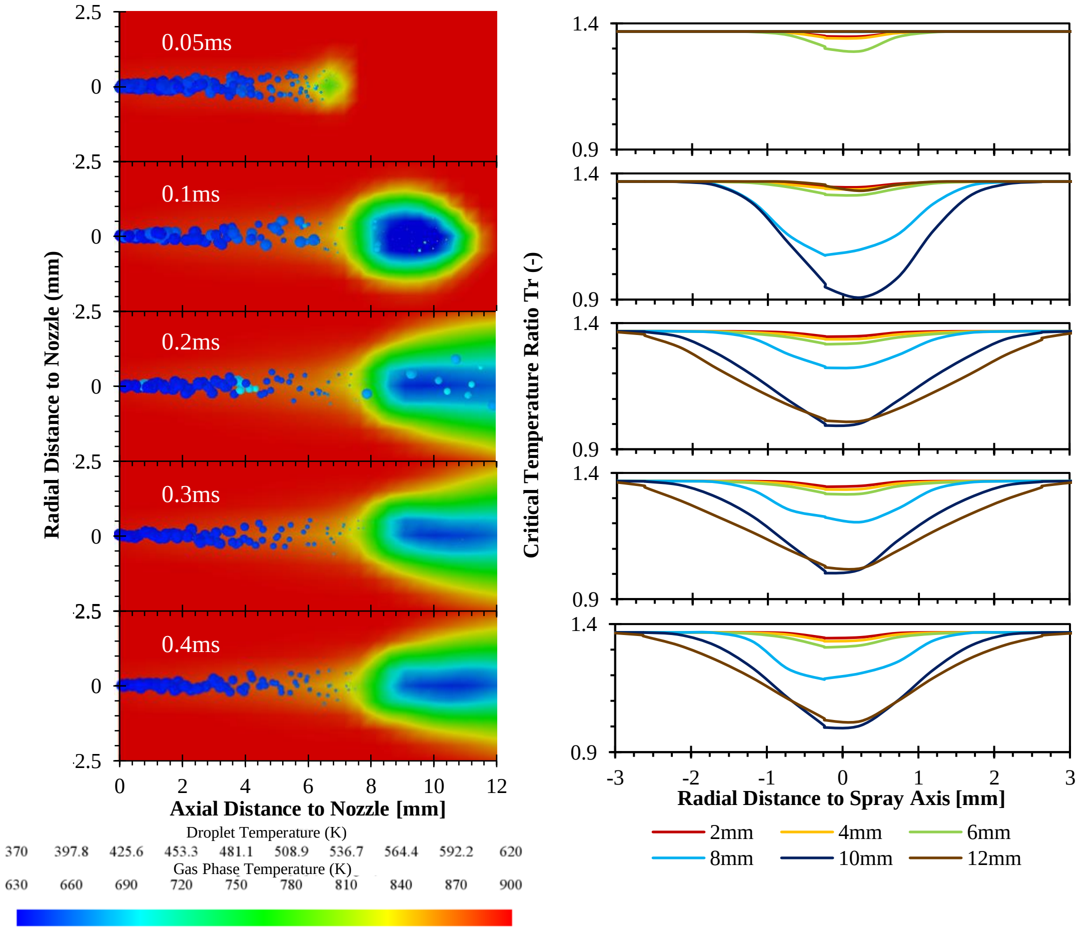

Figure 109: Ambient temperature, droplet sizes (scaled qualitatively) and droplet temperatures (colour scale) at various time-steps (left) and the corresponding radial critical temperature ratio distributions at six axial locations for the baseline ECN Spray A (KP1) (right)

In Crua *et al* in [28], show clear evidence that despite the ambient conditions being supercritical, surface tension and primary atomisation for n-dodecane can be observed, hence categorising the spray well within the ‘classical evaporation’ regime. They further show that even in cases where ambient conditions are so extreme that the fuel ultimately undergoes diffusive mixing, there is still a finite transition time that depends on local gas temperatures and pressures as well as on the fuel’s physical properties. The key points with a density of 22.8kg/m^3 approach the transitional mixing regime at 1100K and even the supercritical regime at 1200K. A detailed analysis of these two key points would exceed the scope of this thesis but must be considered when running simulations with sub models design for subcritical sprays.

Summary of the analysis

Numerically defining the mixing regimen of the droplet in Spray A is difficult because the used simulation package bases its equations in the assumption that the spray is subcritical. The findings in literature that thermal inertia prevent droplets from immediately reaching the supercritical mixing regime offers an attack point to investigate the droplets with the available equations. Nonetheless, this initial analysis was not focussed around the droplets, but rather the gas phase. It was shown that a continuous injection (transient phase) of a cold spray of the baseline Spray A case, in which the ambient gas constitutes supercritical environment, reduced critical temperature ratio. On the mixing regime qualification system derived by Crua *et al* [28] this shifted the condition further to the left meaning it is remained in the subcritical regime. It may well be that the initial droplets do at some point transition into the supercritical mixing regime, however the bulk of the spray is thought to remain subcritical and hence permitting the use of classical sub models.